Université de Neuchâtel
Institut de Microtechnique

Replicated Micro-Optics for Datacom

Thèse

Présentée à la Faculté des sciences
pour obtenir le grade de docteur ès sciences
par

Thomas Ammer

Neuchâtel, Decembre 2001

IMPRIMATUR POUR LA THESE

Replicated Micro-Optics for Datacom

de M. Thomas Ammer

UNIVERSITE DE NEUCHATEL

FACULTE DES SCIENCES

La Faculté des sciences de l'Université de Neuchâtel sur le rapport des membres du jury,

MM. R. Dändliker (directeur de thèse),
H.-P. Herzig, M. Rossi (Zürich) et
J. Jahns (Hagen, D)

autorise l'impression de la présente thèse.

Neuchâtel, le 25 septembre 2002

Le doyen:

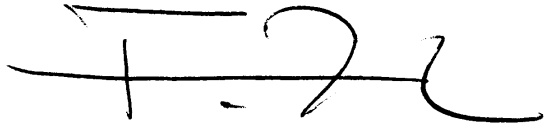

F. Zwahlen

Abstract

Optical data transmission systems have already entered the short and very-short distance domain and are expected to be exposed to increasing performance and cost pressure in the near future. Replicated refractive and diffractive optical microstructures are therefore attractive for use in such applications.

This work is primarily focussed at the utilization of photolithography and replication techniques for the combination of micro-optical structures with active or passive opto-electronic components towards the aspect of integration into such system.

The first chapters cover the design of specific micro-optical structures, such as diffractive optical elements with non-regular zone sizes, deep elements for infrared applications and diffractive or refractive microlenses for the use with Vertical Surface Emitting Lasers (VCSELs). The photolithographic origination of diffractive optical micro-structures such as blazed gratings, diffractive lenses and fan-out elements by mask exposure or direct laser writing and the influence of fabrication effects on their optical performance is treated in detail.

Furthermore, techniques for the replication of optical and mechanical micro-structures based on UV-casting and injection-molding are discussed.

Finally, the use of replicated micro-structures on VCSEL-chips for the coupling of light into optical-fibers is discussed in depth and a low-cost wafer-scale fabrication technology based on UV-casting is presented.

Contents

Chapter 1

Introduction

Along with the coming of the modern information age, communication-based services have undergone an unprecedentedly rapid development. Primarily driven by the Internet, the demand for increased communication bandwidth still seems insatiable. A key role as the enabling factor herein plays optical communication technology, as pure electronic transmission has already reached its limits. Recent developments show that optical information transportation is no longer used exclusively in long-haul (telecom) systems, but moves also more and more into short-range applications (datacom).

Today, the majority of local area networks (LAN's) routers and switches are already equipped with optical fiber links and the future trend directs towards a further integration into intra-system optical interconnects (e. g. optical backplanes), chip to chip communication and optoelectronic integrated circuits. Due to the massive parallel character of such short-range links, the need for low costs systems and components becomes the determining factor for the choice of technology.

To meet this requirements, transmitter systems based on Vertical Surface Emitting Lasers (VCSELs) provide a cost effective solution for such datacom applications. VCSELs operating at 850 nm deliver a number of advantages over edge emitting lasers. They can be directly modulated at high data rates, have low heat dissipation and a low threshold current. The output beam has a circular symmetry, which facilitates the coupling into fibers. A VCSEL is relatively small and thus, a large number of devices can be processed on a single wafer and due to the vertical emission, it is well suited for the production of arrays made to comply with the spacing of fiber ribbons [1].

In a recent market forecast (November 2000) the global market volume for VCSEL based transceivers is predicted to grow from 262 million US$ in 1999 to 3.4 billion US$ in 2004 and 14.1 billion US$ in 2009. The largest growth is expected for intra-system and very short range fiber links [2].

INTRODUCTION

The subject of the author's work summarized in this thesis resides within the field of micro-optics. More precisely, it is focussed at the utilization of photolithography and replication techniques for the combination of micro-optical structures with active or passive opto-electronic components towards the aspect of system integration.

The main objective of this work is dedicated to a low-cost approach for the integration of micro-optical elements with VCSELs taking advantage of techniques based on UV-replication [3]. The origination of most of the diffractive elements described in this work is typically carried out by direct laser writing.

Chapter 2 therefore addresses effects specific to this laser writing fabrication process, which affect the shape of the continuous surface profiles. The typical smoothing due to the limited resolution is described by a mathematical model and different methods for compensation (a geometrical difference method, an iterative Fourier transform algorithm and simulated annealing) are applied to the examples of blazed gratings and fan-out gratings. Scalar and rigorous diffraction theory is employed for the evaluation of the diffraction efficiencies.

Chapter 3 deals with a design concept for diffractive phase elements, which is based on the scalar diffraction theory and Fourier-optics. It describes an specific encoding scheme for the translation of the design phase function into a diffractive surface, which typically results in non-regular zone sizes. It is shown that in the ideal case, a phase element designed in this manner exhibits the same diffractive behavior as an element with a regular encoded phase function. In presence of a wavelength detuned from the design value or profile depth deviations, the zone-variation principle can have advantageous properties in terms of stray light suppression. Consequently, the concept offers the capability to improve the design for less restrictive fabrication tolerances. Another possible application is the increase of the spectral bandwidth of the element, e.g. for the use with multimode sources. As an example, the diffractive behavior of blazed gratings [4] and diffractive lenses [5, 6] encoded with this scheme is investigated.

In many cases, it is desirable to have structures with large profile depths in order to produce diffractive elements designed for long wavelengths (Infrared) or for higher diffraction orders. Furthermore, the elements might also have a mechanical functionality, which ensures the alignment or spacing of the element with respect to its substrate or other to elements.

Chapter 4 describes an example for the fabrication of deep direct laser written surface profiles for infrared applications and the fabrication of special guiding and alignment structures for optical fibers using thick-film lithography. In order to achieve the consistency between cost-effectiveness and a

complicated and time-consuming origination of the micro-optical elements, the reproduction of the elements and integration on chip or on wafer-scale level is accomplished by UV-replication techniques, primarily using Sol-Gel materials [7, 8, 9]. This process and its application to the processing of VCSEL chips and wafers are also outlined in Section 4.

The last Chapter covers the application of the above described technologies for an exemplary system for multimode VCSEL to fiber coupling with a diffractive coupling lens. Beginning with the characterization of the modal near- and far field properties of the VCSELs, a mathematical model is developed for the description of the source. The propagation of the (scalar) fields through the system is based on fast Fourier beam propagation algorithm. This model is then used for the simulation of the influences of the chosen dimensions on the fiber coupling efficiencies and positioning tolerances taking into account the modal characteristics of the laser. Based on the method depicted in Chapter 2, the performance of the diffractive lens itself is estimated by evaluation of the local diffraction efficiency of each lens zone under consideration of the illumination conditions. Finally, some experimental results for diffractive lenses replicated onto $850\,nm$ multimode VCSELs are presented. In addition, results for replicated fiber guiding structures based on the same technology are shown.

Chapter 2

Direct laser written micro-optical elements: fabrication-inherent relief deviations

The fabrication of high-quality micro-structures is often a key factor for the successful realization of micro-optical applications. A great variety of tools and processes, initially developed for the micro-electronics industry and other branches of micro-technologies are being adopted for the fabrication of micro-optical elements. Among the most important methods are photolithographic processes, such as mask lithographic techniques (e.g. single or multiple-step binary mask lithography, gray-tone lithography) or scanning methods such as electron beam writing or direct laser writing. The methods are widely used and also optimized for the demands of micro-optics [10].

However, the relief quality and thus the optical performance of micro-optical structures is mainly determined by the reliability and precision of the fabrication process. Especially with diffractive structures, such as diffractive lenses with a high numerical aperture or gratings designed for large diffraction angles, the minimum feature sizes often reach the resolution limits of the fabrication method.

This chapter deals with the surface relief deviations caused by the limited resolution of direct laser writing. Such fabrication inherent effects are mathematically modelled using a convolution operation. We present different algorithms for the compensation of this convolution effect during the design of the profile shape: First, a pure geometrical approach is described for the optimization of the design profile. Second, the profile is diffraction-efficiency optimized using a scalar iterative Fourier transform algorithm and finally, an

optimization based on rigorous coupled wave analysis and simulated annealing is presented. To our knowledge, it is the first time that such a rigorous optimization algorithm, which simultaneously takes fabrication specific effects into account, has been applied to continuous diffractive surface reliefs. Theoretical, as well as experimental results are presented for the examples of blazed gratings and fan-out gratings.

The mentioned mathematical approach using convolutions for the simulation and optimization of surface reliefs is also applicable to other fabrication methods [11, 12]. Additional details can be found in publication I.

2.1 Direct laser writing

Most of the diffractive optical elements described is this thesis have been produced by direct laser writing in photoresist (see chapter 4 in reference [13] or chapter 4 in reference [3]). The method is appropriate for the rapid prototyping of elements or the origination of master structures for subsequent replication.

Figure 2.1 illustrates the optical and mechanical setup of the used system. A blue Helium-Cadmium laser ($\lambda = 0.442\,\mu m$) is intensity-modulated (with 8 bit resolution) and focussed onto the resist substrate. High-precision xy-translation stages assure the accurate scanning and positioning of the laser beam. The minimal separation of the scanning lines is $0.4\,\mu m$. A Gaussian spot with constant diameter is accomplished by an optical auto-focus unit, which controls the position of the objective by help of a piezo drive. In typical operation, a microscope objective with a numerical aperture of 0.65 is used. This assures a writing spot diameter in the order of $1\,\mu m$ full width at half maximum (FWHM). The spot size can be determined with an integrated detector equipped with a piezo-driven knife-edge scanning unit.

The exposure data is encoded in a specific file format and imported to the control computer, which automatically processes the tasks in batch operation.

Typical fabrication conditions involve the writing of structures with a minimum feature size of few microns in layers of positive photoresist with a thickness in the order of $1\,\mu m - 5\,\mu m$. The limitation for the thickness is determined by the exposure and development characteristics of the chosen photoresist.

We have used this method for the fabrication of discrete elements and components for the integration into optical microsystems, e.g. blazed gratings (this chapter and chapter 3), fan-out elements (this chapter), diffractive lenses (chapter 5) and binary mask layouts for fiber guiding structures (chapter 4). For the origination of diffractive optical elements for mid-infrared

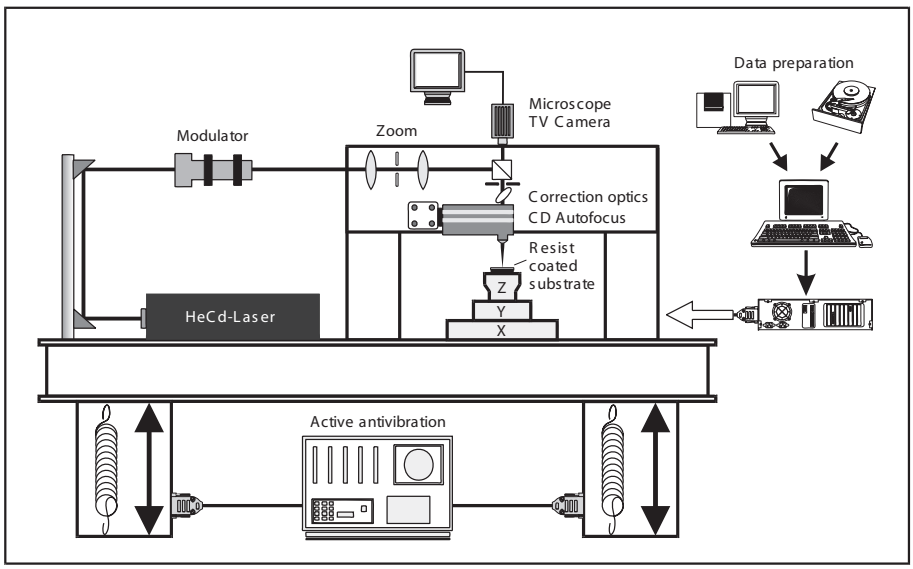

Figure 2.1: Schematic diagram of the direct laser writing system.

applications, the realization of structures up to $20\,\mu m$ thickness has been demonstrated (see chapter 4 and Publication IV).

2.2 The convolution effect

As already mentioned, the minimum feature size is limited by the resolution of the exposure. This results in a loss of finesse of the structural details after development. For example, the typical sharp profile steps in many diffractive structures suffer from smoothing.

Neglecting nonlinearities of the resist response (during development) to the laser beam exposure, the mentioned "smoothing effect" in direct laser beam writing can be approximated by a convolution of the designed exposure profile with a Gaussian shape function. Hence, the normalized smoothing function can be written as

$$g(x) = \frac{2}{w}\sqrt{\frac{\ln 2}{\pi}}\exp\left[-\left(\frac{2\sqrt{\ln 2}x}{w}\right)^2\right], \tag{2.1}$$

where w denotes the Gaussian diameter as full width at half maximum (FWHM). Note that w does not necessarily coincide with the real writing spot diameter determined by e.g. a knife-edge measurement. Since the writing beam is linearly scanned over the resist substrate, the actual transversal

exposure-dose distribution at a fixed point on a scanning line is equivalent to the time-integral of the spot intensity distribution. In addition, the dose-profile also depends on the material, the thickness and the development characteristics of the resist layer. Therefore, $g(x)$ shall be referred to as the "effective writing spot" and has to be empirically determined.

The convolution of the surface-relief profile, here denoted as $f(x)$, with $g(x)$ is accomplished by using the convolution theorem

$$\mathcal{F}\left[f(x) \circledast g(x)\right] = F(\nu)\, G(\nu). \tag{2.2}$$

Here $\mathcal{F}$ denotes the Fourier-transform and $\circledast$ the convolution operation. Functions $F(\nu)$ and $G(\nu)$ are the Fourier transforms of $f(x)$ and $g(x)$, respectively.

Figure 2.2 schematically illustrates the smoothing effect of the convolution of an ideal profile with a Gaussian function for the example of a) a blazed grating and b) a diffractive lens.

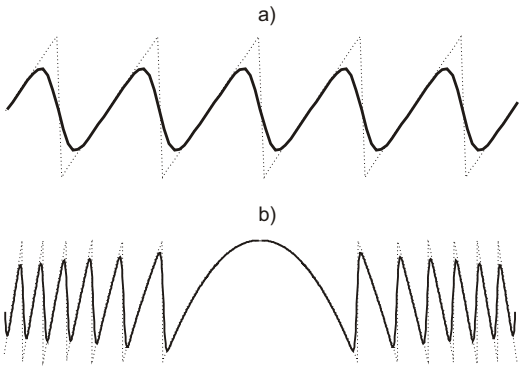

Figure 2.2: Convolution effect

While for the blazed grating, the deterioration is constant for each diffractive zone, it is negligible in the center of the diffractive lens, but increases with the distance from the center. As the local zone sizes of an diffractive optical element (DOE) reach the order of the effective spot size, the convolution effect has to be taken into account. An important parameter for DOEs is the design diffraction order, which we will denote by M. This number is directly associate with the resulting zone sizes. For example, a blazed grating of a certain length with $M = 4$ has four times less zones than the corresponding first order grating. Consequently, the number of zone boundary steps and the minimum lateral feature size are accordingly decreased. Thus, the convolution effect is less significant for a DOE with higher values of M. However, the choice of higher design orders has to be paid for with larger structure

depths, which in return causes a larger effective writing spot. No general statement can be made for the optimal value of M, since it also depends on the shape of the structure. For diffractive lenses and blazed gratings designed for visible wavelengths, in many cases a design order in the range of $M = 2...4$ yields the best results.

2.3 Compensation methods

In this section, a brief overview of different approaches for a pre-compensation of the design profile in order to improve the efficiency of the real element is given. We describe a profile optimization for DOEs based on a pure geometrical method and the compensation of the design profile by optimization of the diffraction properties.

2.3.1 Geometrical profile optimization

A simple and straightforward method for improving the performance of a diffractive profile relies on a geometrical minimization of the profile deviations from its ideal design. Particularly for structures which can be categorized into the domain of scalar diffraction theory [14], this is an intuitive approach. An iterative optimization algorithm is employed for the convolution pre-compensation of an arbitrary diffractive profile. We consider the pixel-wise optimization of the desired design function $f_0(x)$. Starting with $f_0(x)$, the corresponding convolved function $h_0(x) = f_0(x) \circledast g(x)$ is calculated. The starting function for the next iteration step is then determined by taking the difference between h and f and adding this difference to f [11]:

$$f_{i+1}(x) = f_i(x) + [f_i(x) - h_i(x)]\,. \tag{2.3}$$

Since the function f has to be translated into an exposure profile for the writing process, the range for the depth values is limited to the thickness of the resist layer ($dmax$). Therefore, f has to be truncated to $[0, dmax]$ after each iteration. It is also advantageous to center f about $dmax/2$. A convergence of the result is typically reached after $10 - 20$ iteration steps [15].

Figure 2.3 schematically illustrates the convolution effect for the example of a blazed grating profile. It also shows a typical shape of a pre-compensated profile and the resulting shape after convolution.

In the example shown in figure 2.3, the grating period Λ corresponds to four times the effective spot size w. The compensated profile centered and truncated to a thickness of three times the design profile depth. Numerical

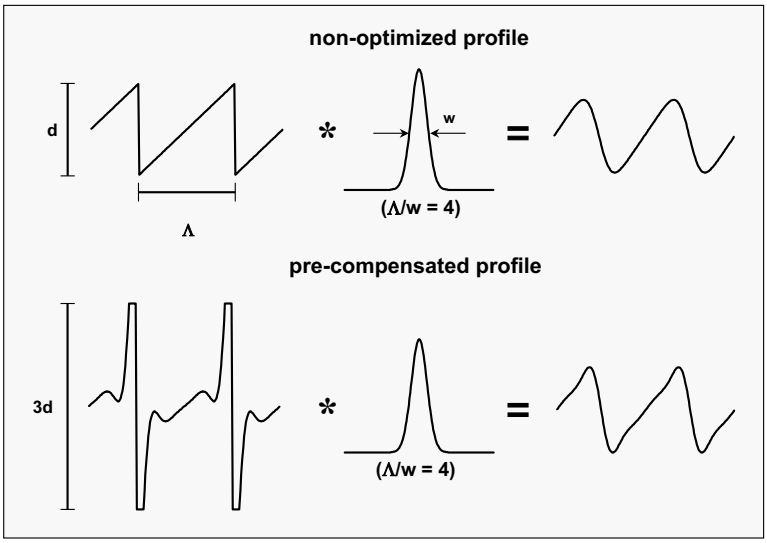

Figure 2.3: Schematic illustration of the convolution of a blazed grating with a Gaussian function. The upper plot shows the resulting profile shape in case of the non-optimized profile and the lower plot the same for a pre-compensated profile, respectively.

examples of blazed gratings optimized in this manner are presented in section 2.4.1.

2.3.2 Iterative Fourier-transform optimization

In this and the following section, we describe two concepts for a non-linear compensation of the convolution effects by a direct optimization of the diffraction behavior of the DOE. They are both based on iterative algorithms for the optimization of the complex amplitude transmittance of the element (see section 1 in reference [13]). These algorithms represent general design concepts, which have not been initially developed for the compensation of fabrication-induced effects. However, the consideration of the convolution effect already in the optical design phase automatically accomplishes a compensation and an implementation is straightforward [16, 17].

The iterative Fourier-transform algorithm (IFTA, also called Gerchberg-Saxton algorithm) [18] is well suited for the direct encoding of continuous diffractive surfaces. Usually, the DOE is treated as a phase-only element and scalar diffraction theory is employed. Typical examples for the use of this method are the application to beam-shaping problems (e.g. Gaussian to

flat-top beam transformers of fan-out elements) [17, 19, 20, 21, 22, 23] or the realization of computer generated holograms (CGH's) [24, 25].

The method relies on the evaluation of diffraction integrals formulated in Fourier-transform representation (Fourier-optics)[26, 27, 28]. Therefore, the fields in the diffraction (image) plane and in the DOE plane are mutually related by forward and inverse Fourier transforms. This corresponds to the Fraunhofer-approximation. However, the method can also be applied to more complex relations [13].

Since we have constrained ourselves to phase-only elements, we seek for a phase-function in the DOE-plane which can be directly mapped into a surface profile and which produces the desired intensity distribution in the image plane. Starting point is this intensity distribution in the image plane. At the beginning, a guess for the phase distribution in the image plane is taken. The IFTA can be outlined as follows:

1. reverse propagation of the image field to the DOE-plane by an inverse Fourier transform,
2. adjustment of the amplitude in the DOE plane to the amplitude of the incident plane while keeping the phase,
3. application of the convolution operation (or other fabrication constraints) to the phase function,
4. forward propagation of the field to the image plane,
5. adjustment of the intensity to the design intensity distribution while keeping the phase.

Steps 1-5 are iteratively repeated until the chosen merit function (uniformity, efficiency, etc.) converges to an acceptable level. Thanks to Fast Fourier Transform (FFT) techniques, the method allows a very fast an efficient numerical implementation. However, the convergence of the IFTA strongly depends on the chosen starting guess parameters and frequently stagnates in local minima [13]. An example for a successful global optimization method is the simulated annealing algorithm.

2.3.3 Simulated Annealing

The simulated annealing algorithm (SA) is an iterative method which allows for a global optimization of the DOE profile. Its name derives from its analogy to the process of energy minimization of a physical body during thermal annealing [29, 30].

Starting point is an appropriate description of the profile shape, e.g. polynomial coefficients or the transition positions of a binary structure. In case of direct laser writing, this profile function will be preferably described by the intensity of the corresponding exposure pixel. For the special case of blazed gratings and diffractive lenses with modulated zone sizes, as described in chapter 3, the surface will be determined by the locations of the zone boundaries. To account for the smoothing effect, this profile can also be convolved before evaluation the diffraction.

For the determination of the diffracted field in the region of interest, scalar or rigorous methods can be applied. Furthermore, a merit function U, which accounts for the difference between the diffracted field and the desired pattern, needs to be defined (e.g. the intensities of the diffracted orders). We define U in a way, that $U = 0$ corresponds to 100 % conformity and thus, it has to be minimized.

During each iteration loop n in the SA-algorithm, all surface parameters are changed sequentially within a predefined range and after each change, the merit function is recalculated. The decision, whether the change is accepted or not, depends on the change of the merit function $\Delta U = U_{new} - U_{old}$. Is $U < 0$, the change is always accepted. If $U \geq 0$, the change is accepted with a probability of $p(n) = exp\,[-\Delta U/T(n)]$. The parameter $T(n)$ accounts for the "temperature" and determines the probability $p(n)$. T is constantly lowered in each iteration step n from an initial value T_0, typically in an exponential decay. The initial value and the rapidness of the decay are problem-dependent and have to be chosen carefully, in order to avoid the process to get stalled in a local minimum. When U reaches a stationary state or does no longer decrease, the process is halted. The success of the method strongly depends on the proper choice of the function $T(n)$ and on the strategy of changing the parameters to be optimized [13].

2.4 Theoretical and experimental examples

In this section, some theoretical as well as experimental examples are presented for blazed gratings [3, 4] and fan-out elements (one- and two-dimensional) [20, 21, 31]. Blazed gratings play an important role in diffractive optics as calibration structures, since they are easy to model and to characterize. In addition, the zones in outer regions of diffractive lenses are frequently approximated as local blazed grating sections [32, 33, 34]. In this manner, the local diffraction efficiency of these section can be estimated in a simple way. Therefore, blazed gratings are very useful objects to study the effects of profile convolution. On the other hand, fan-out elements have important ap-

plications in the fields of optical interconnects and optical computing [22]. Its purpose is the splitting of an incident beam into a defined number of diffraction orders with equal intensity. Furthermore, the uniformity and efficiency of these orders are highly sensitive to profile distortions [35]. Thus, they can serve as a good instrument to qualify the performance of the convolution compensation.

2.4.1 Blazed gratings

The convolution effect primarily affects fine details and discontinuities in the profile shape of a DOE. In case of blazed gratings, such discontinuities occur at the zone boundaries. In figure 2.4, the smoothing of the profile steps is elucidated. In the same figure, the smoothed version of a blazed grating which has been optimized by the geometrical compensation method (section 2.3.1) is plotted. It is well perceptible, how the affected area can be reduced in this way. The ratio between grating period and convolution spot size in this example is $\Lambda/w = 0.25$ and the depth of the compensated grating is clipped to three times the depth of the uncompensated one.

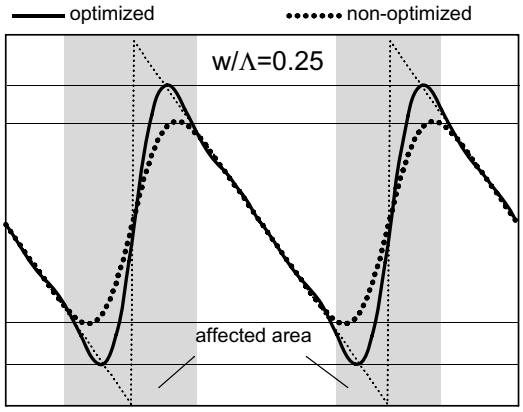

Figure 2.4: Convolution-smoothed profile shape of a standard blazed grating profile and the corresponding pre-compensated profile (geometrical optimization). The profile sections affected by the convolution for both cases are sketched by the shaded areas. Horizontal lines indicate the effective depth and the shaded areas schematically indicate the lateral extents of the profile distortions .

Some theoretical results for the diffraction efficiencies obtained by Fourier optical calculations [26, 27] (scalar diffraction) using the thin element approximation [36] are summarized in table 2.1. The diffraction efficiency η is shown for optimized and non-optimized gratings of design diffraction orders

$M = 1, 2, 4$ and for ratios $\Lambda/w = 0.05, 0.1$ and 0.2. For all cases, the compensation method was the geometrical optimization as outlined in section 2.3.1 and the maximum allowed profile depth is three times the depth of the non-compensated grating.

Table 2.1: Diffraction efficiencies η_M, calculated with scalar diffraction theory for smoothed blazed gratings. Results for regular non-optimized, (η_{reg}) and convolution-optimized (η_{opt}), blazed gratings of orders $M = 1, 2, 4$.

	$M=1$		$M=2$		$M=4$	
w/Λ	η_{reg}	η_{opt}	η_{reg}	η_{opt}	η_{reg}	η_{opt}
0.05	0.88	0.93	0.86	0.91	0.84	0.89
0.10	0.77	0.85	0.73	0.83	0.69	0.80
0.20	0.57	0.72	0.50	0.68	0.43	0.61

It becomes clear, that for given w, the resulting efficiency strongly depends on the grating period Λ. The compensation has a more significant effect, if Λ decreases. As expected, the efficiency increases if a higher design order M is chosen. Please note, that a higher order grating has a period of M-times the period of a first order grating with the same deflection angle. For example, a third order grating with a period of $\Lambda = 15\,\mu m$ would have a first order pendant with a period of $\Lambda = 5\,\mu m$! Therefore, an improvement of the diffraction efficiency can already be accomplished by choosing a higher value for M. As it is readily seen in table 2.1, a non-optimized second order blazed grating already yields an efficiency comparable to the optimized first order version. The same holds for $M = 2$ and $M = 4$.

However, considering real fabricated elements, the efficiency of higher design order gratings is also influenced by the following factors:

1. The choice of higher orders is associated with larger profile depths (M times the depth of a first order grating). This in turn decreases the resolution of the fabrication process and causes an increase of w (which is typical for analog written structures).

2. The larger depth can limit the depth-range available for compensation (see figure 2.4), for a given resist layer thickness.

3. If $\Lambda/M \lesssim 10\lambda$, the use of scalar diffraction theory is no longer appropriate [14].

Therefore, if the minimum absolute period length of higher order gratings does not fulfil the above condition, significant diffraction efficiency losses

have to be taken into account, unless a rigorous optimization is performed (see publication I).

We have fabricated first order blazed gratings in photoresist ($n = 1.64$), designed for a wavelength $\lambda = 0.633\,\mu m$ and periods of $\Lambda = 5, 8, 10$ and $15\,\mu m$ by direct laser writing. The design profile depth is $d = 0.99\,\mu m$ and the effective spot diameter is $w = 1.1\,\mu m$ (FWHM). Figure 2.5 shows the measured diffraction efficiencies for these gratings with optimized and non-optimized profile, respectively (geometrical optimization method).

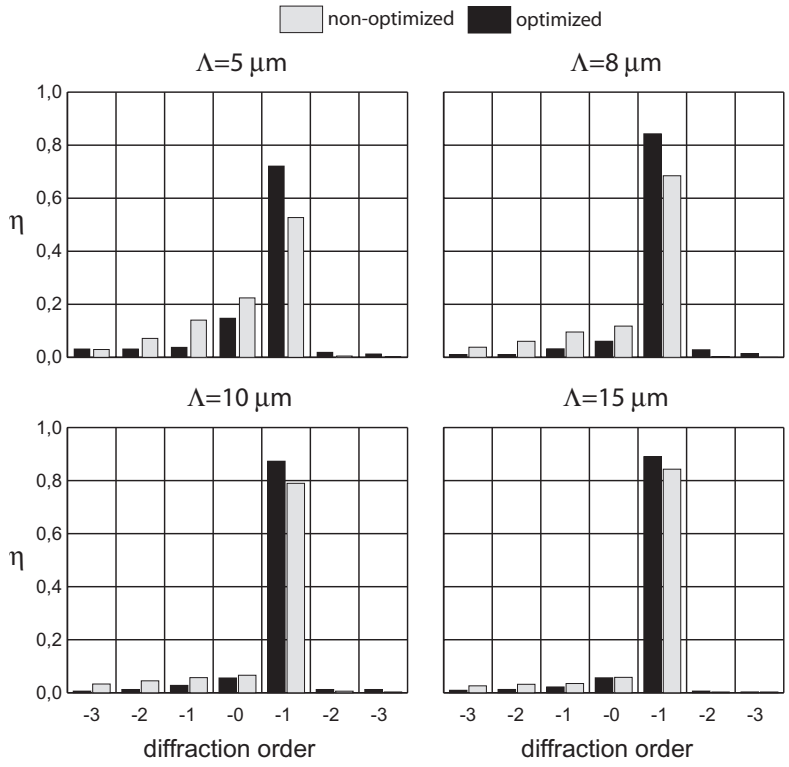

Figure 2.5: Measured efficiencies of optimized and non-optimized first order blazed gratings with periods of $\Lambda = 5, 8, 10$ and $15\,\mu m$.

It is readily seen from this plots, that the compensation is the more effective, the smaller the grating period. For $\Lambda = 5\,\mu m$, an improvement by a factor of 0.36 could be achieved, whereas for the $\Lambda = 15\,\mu m$ grating, the improvement is only 0.06. The results agree very well with the theoretical values given in table 2.1. Note that although a grating with a period of $\Lambda = 5\,\mu m$ already approaches a domain where scalar diffraction theory already looses its validity and rigorous treatments should be employed for exact evaluation [14], the simple geometrical compensation method still yields considerable improvements.

Higher order blazed gratings with absolute periods $\Lambda \lesssim 10\lambda$, require the use of rigorous diffraction calculations for accurate results. We have investigated the diffraction efficiency for higher order blazed gratings ($M = 3, 4, 5$) with periods $\Lambda = 4, 5.2$ and $6\,\mu m$ and an effective Gaussian beam of $w = 0.5\,\mu m$ as an example for the investigation of the convolution effect in the rigorous diffraction domain.

In addition to the pure evaluation, we have also employed an optimization method based on rigorous coupled wave analysis (RCWA) [37, 38]. Starting from the ideal profile shape and depth as obtained from the thin element approximation (Sweatt approximation, cf. section 3.2), the profile has been rigourously optimized while simultaneously taking the convolution effect into account. Such a treatment is a novel way (to our knowledge) to compensate for fabrication specific effects.

All rigorous diffraction analysis and -optimization has been performed by Ilkka Kallioniemi (see publication I). For the optimization, a simulated annealing algorithm was used along with diffraction efficiency calculation by the RCWA method. For the diffraction efficiency calculations of the above mentioned gratings have been done assuming a normally incident TE-polarized plane wave with a wavelength $\lambda_0 = 0.633\,\mu m$ and a grating in photoresist ($n = 1.64$). The diffraction medium is air ($n = 1.0$). The results for the diffraction efficiencies of both the non-optimized and optimized blazed gratings are summarized in figure 2.6.

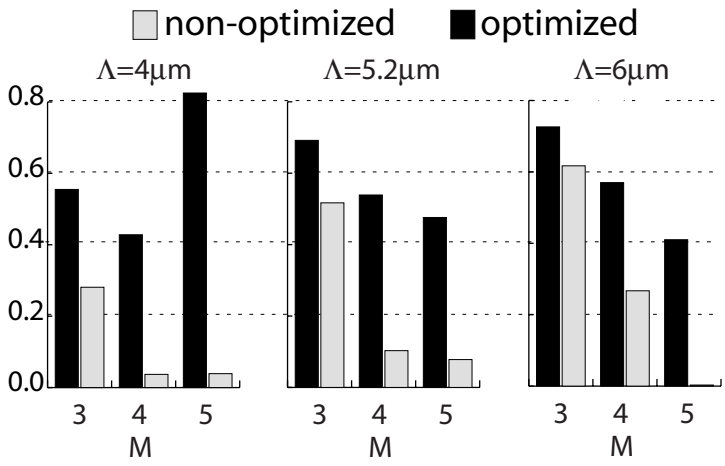

Figure 2.6: Calculated rigorous efficiencies of optimized and non-optimized blazed gratings of order $M = 3, 4, 5$ with absolute periods of $\Lambda = 4, 5.2$ and $6\,\mu m$. The profiles are convolved with an effective beam with $w = 0.5\,\mu m$. The diffraction efficiencies are normalized to the sum of transmitted orders.

This graphs confirm, that for higher order blazed gratings with such small periods, the scalar approximation completely fails (cf. table 2.1). For $\Lambda = 4, 5.2$ and $M = 4, 5$ the diffraction efficiency is even below 0.1. In all cases, a considerable improvement of the diffraction efficiency to values better than 0.4 could be achieved with the optimization. Please note, that the grating periods noted in the figure are absolute values and the different orders do not correspond to gratings with the same deflection angle.

It has to be emphasized, that this dramatic improvement is partially due to the fact that the initial depth has been taken from the scalar approximation. For higher order blazed grating , the diffraction efficiencies can already be significantly improved by adjusting the depth. As depicted by figure 2.7, the diffraction efficiency of the $\Lambda = 5.2\,\mu m, M = 4$ blazed grating (convolved) can be raised from $\eta \approx 0.06$ to $\eta \approx 0.3$, reducing the depth by a factor of 0.2. With additional convolution compensation, the efficiency can be further increased to approximately $\eta = 0.54$ (figure 2.6). The deviation of the optimal depth from the thin element approximation value is below a factor of 0.1 for first order blazed gratings and increases with M.

However, the consideration of the convolution effect in any rigorous optimization algorithm is straightforward and offers additional potential for improvement of the diffraction efficiency.

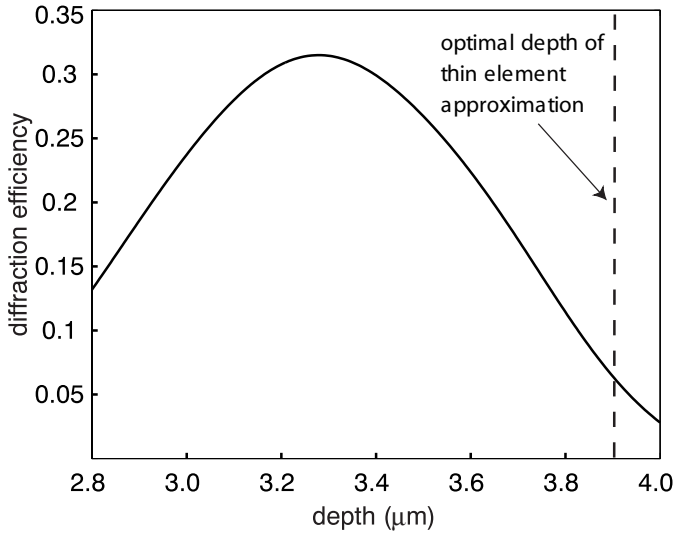

Figure 2.7: Rigorous diffraction efficiency calculation of a convolved ($w = 0.5\,\mu m$) fourth order ($M = 4$) blazed grating with $\Lambda = 5.2\,\mu m$, designed for $\lambda_0 = 0.633\,\mu m$ and $n = 1.64$ (TE-polarization). Graph courtesy of Ilkka Kallioniemi.

2.4.2 Fan-out elements

For a demonstration of the convolution effect with diffractive fan-out gratings, examples of transmissive elements designed for a red HeNe laser with $\lambda = 0.633\,\mu m$ have been realized in photoresist ($n = 1.64$) on a glass substrate. Three different one- and two-dimensional fan-out gratings (1×9, 1×15 and 4×4) have been fabricated with an effective writing spot $w = 1.1\,\mu m$ (FWHM). Table 2.2 lists the measured values for the uniformity and the total diffraction efficiency η for these samples.

Table 2.2: Measured uniformities and total diffraction efficiencies of standard and convolution-optimized one- and two-dimensional fan-out elements (1×9, 1×15 and 4×4).

	uniformity		efficiency	
element	non-opt.	opt.	non-opt.	opt.
1×9	0.54	0.21	0.85	0.95
1×15	0.82	0.17	0.81	0.95
4×4	0.44	0.25	0.81	0.85

Hereby, the uniformity σ has been defined by the maximum and minimum intensities occurring among the fan-out orders [13]:

$$\sigma = \frac{I_{max} - I_{min}}{I_{max} + I_{min}}, \tag{2.4}$$

and the efficiency η as the sum of the intensities I_j carried the N individual fan-out orders normalized by the intensity I_0 of the incident beam (not taking losses caused by reflection of the incident beam into account):

$$\eta = \frac{1}{I_0} \sum_{j=1}^{N} I_j. \tag{2.5}$$

All elements (convolution compensated and non-compensated) have been designed with an iterative Fourier-transform algorithm, as described in section 2.3.2. The designs were performed by Andreas Schilling (see chapters 3 and 4 in reference [39]). The phase functions corresponding to the non-optimized and convolution optimized 1×9 and 1×15 fan-out gratings are displayed in figure 2.8. In the non-compensated cases, the design phase functions for both gratings are wrapped to an interval of 2π. Consequently, the 1×9 fan-out grating has two and the 1×15 grating four phase jumps per period. These discontinuities are primarily affected by the convolution effect

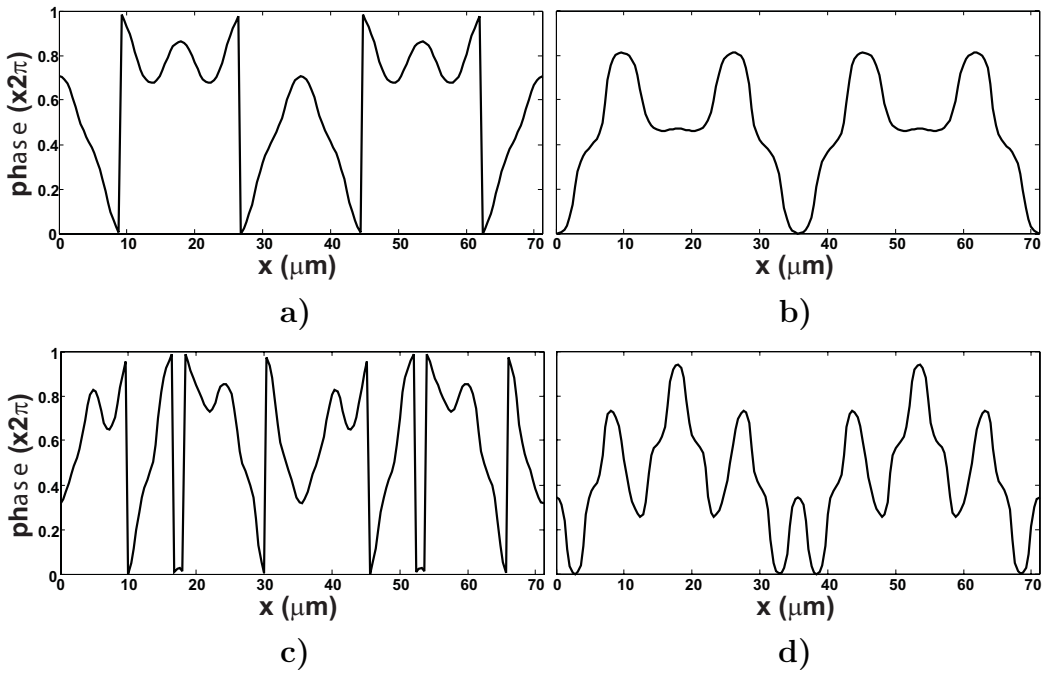

Figure 2.8: Design phase functions of one-dimensional fan-out gratings (2 periods). a) 1×9 fan-out, non-compensated, b) 1×9 fan-out, compensated, c) 1×15 fan-out, non-compensated and d) 1×15 fan-out, compensated.

and thus responsible for the loss in diffraction efficiency . In contrast, the optimization procedure yielded profiles without phase discontinuities.

Figure 2.9 shows the measured diffraction efficiencies of all orders for the 1×9 fan-out grating and the results for the 1×15 sample are shown in figure 2.10. The grating periods of the two one-dimensional elements are $\Lambda = 35.6\,\mu m$.

Both figures confirm the significant improvement of the uniformity as well as the efficiency (as quoted in table 2.2), due to the convolution-compensation. The poorer uniformity of the non-compensated fan-outs is mainly caused by the high efficiency of the zeroth diffraction order. This dominance could be significantly reduced with the compensation procedure. In addition, the experimental results are also in good agreement with the theoretical expectation [39].

In figure 2.11, diffraction efficiency measurements for the case of a two-dimensional (4×4) grating are shown. For this element, the grating period is $\Lambda = 37.6\,\mu m$. The improvement of the uniformity is well recognizable. In particular, the dominance of the zeroth order is again significantly deduced.

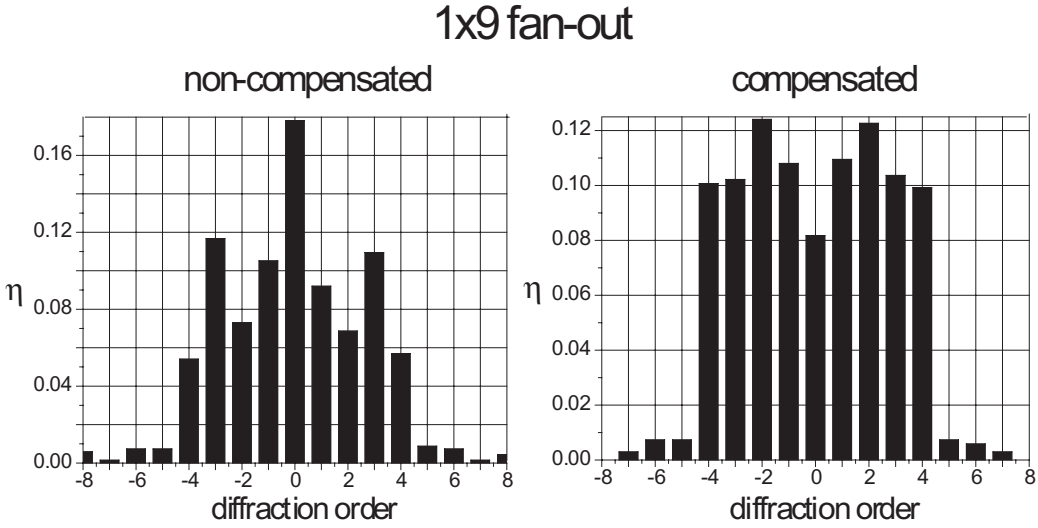

Figure 2.9: Measured diffraction efficiencies of a non-compensated and a convolution compensated 1×9 fan-out grating realized in photoresist.

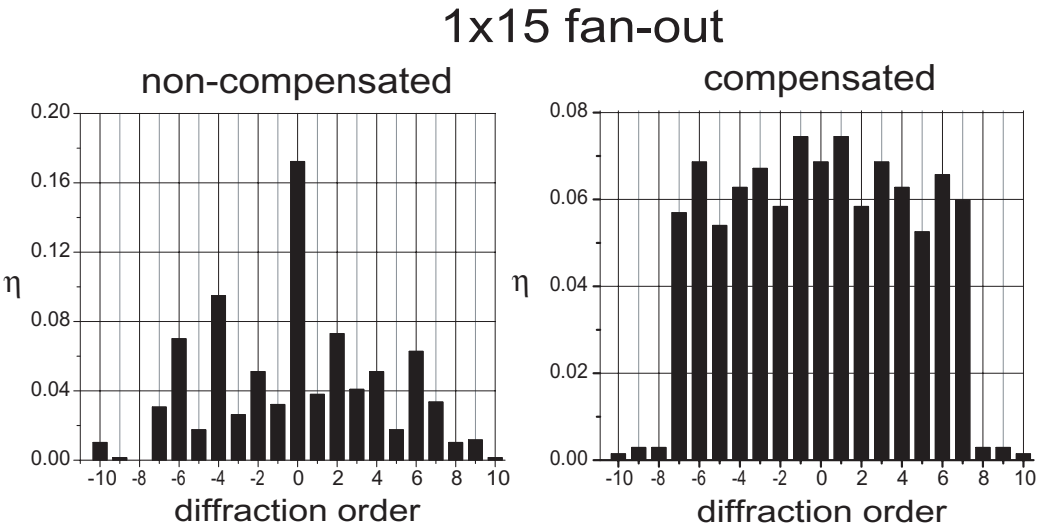

Figure 2.10: Diffraction efficiency measurements of a non-compensated and a convolution compensated 1×15 fan-out grating, analogue to figure 2.9.

2.5 Conclusions

Different methods for the compensation of the convolution-effect in direct laser written micro-optical structures have been introduced. With the example of blaze gratings, the pure geometrical profile optimization yielded already considerable potential for the improvement of the diffraction efficiency, par-

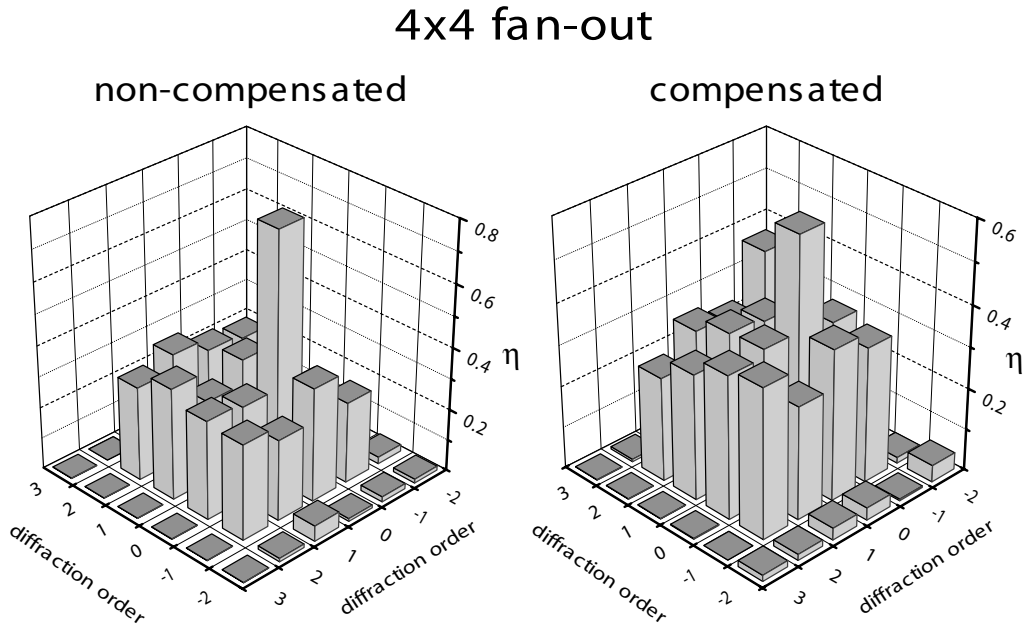

Figure 2.11: Measured diffraction efficiencies of a non-compensated and a convolution compensated two dimensional 4×4 fan-out element, fabricated by direct laser writing in positive photoresist.

ticularly for large ratios w/Λ. The results could be successfully confirmed by experimental data. Simulations using a simulated annealing algorithm in combination with rigorous diffraction analysis demonstrated the potential of the diffraction efficiency improvement of blazed gratings with periods smaller than 10λ. Furthermore, experimental examples of one- and two-dimensional fan-out elements proved the applicability of the convolution-compensation concept to DOEs designed by an iterative Fourier transform algorithm. The optimization of the uniformity as well as the improvement of the overall diffraction efficiency of the fan-out elements has been demonstrated.

Chapter 3

Diffractive optical elements with modulated zone sizes

The use of diffractive optical elements in compact optical microsystems is typically limited in geometrical dimensions and propagation lengths. Consequently, elements with large deflection angles and small periods are often required (as discussed in chapter 2). Due to fabrication inherent imperfections or wavelength deviations, such elements can give rise to stray light levels, which lower the overall performance of the system and can be critical for certain applications. In particular for beam shaping, focusing or collimating diffractive elements, interference effects between the design and unwanted diffraction orders (stray light orders) can significantly affect the beam quality [40].

This chapter describes an alternative approach for the encoding of a design phase function in to a diffractive surface with interesting properties for beam quality improvement or stray light suppression. The result is a DOE with an additional degree of freedom for the design of the individual zone sizes. This can help to improve the performance of elements with systematic fabrication errors or to improve the spectral tolerances.

3.1 Introduction

For thin phase-only diffractive optical elements with large periods, compared to the optical wavelength ($\Lambda \lesssim 10\lambda$) [14], the design method first formulated by Sweatt [36] is often used. Thereby, a design phase function $\Phi(x)$ is first wrapped into an interval $[\phi_0,\, \phi_0 + M2\pi]$ and then translated into the surface relief $d(x)$ of the DOE by a linear mapping [13, 3]. M is an integer number which corresponds to the design diffraction order and ϕ_0 represents an arbi-

trary (constant) phase offset. Typically, M and ϕ_0 are the only parameters which are used for the specification of the phase-wrapping. In this manner, the resulting zones of the DOE-profile are of equal height and vertically aligned.

However, such a uniform zone-alignment is not a mandatory condition for the implementation of a diffractive surface. We present a more general design approach for DOEs within the domain of scalar diffraction theory. For example, the generalized form of a blazed grating is an irregular arrangement of zones with non-uniform size, but with a defined phase correlation. The spectral properties of such elements typically deviate from the properties of conventionally designed elements, whereas its diffractive properties at the design wavelength are equivalent. These properties and the additional degree of freedom for the design can be used for an improvement of the spectral behavior.

Section 3.2 deals with the special properties of such elements and gives an answer to the question, whether its behavior is still diffractive. In section 3.3, methods for the evaluation and optimization of the diffractive properties are given. Some numerical and experimental investigations for blazed gratings are presented in section 3.4. Finally, in section 3.6, a potential application of the design principle for focusing and collimating diffractive lenses is studied theoretically.

3.2 Design concept

In the following, we consider a pure phase element and assume the validity of the thin-element approximation. The conventional derivation of the surface profile comprises a wrapping of the design phase function $\Phi(x)$ into an interval, whose length is an integer multiple of 2π:

$$\Phi_D(x) = \Phi_{wrap}(x) = mod\left[\Phi(x)+\phi_0;\, 2\pi M\right]. \tag{3.1}$$

The translation of the derived diffractive phase function $\Phi_D(x)$ into a physical relief profile is typically accomplished by use of the Sweatt-approximation [36]:

$$d(x) = \Phi_D(x)\frac{\lambda_0}{n_1 - n_2}, \tag{3.2}$$

where n_1 and n_2 are the refractive indices of the grating material and the ambient, respectively, and λ_0 depicts the design wavelength in vacuum. This relation implies, that the phase delay introduced by the DOE is proportional to the profile depth.

Without loss of generality, we regard in the following a blazed grating as a simple model for the illustration of the method specified by equations 3.1 and 3.2. Starting from a linear phase function $\Phi(x) = \phi_0 + 2\pi M x/\Lambda$, the wrapped phase derives to a shape as shown in figure 3.1b). The resulting surface relief can be interpreted as a regular arrangement of equally sized and spaced micro-prisms. The profile step between two adjacent prisms corresponds to a phase difference of $M2\pi$. An optically equivalent interpretation can be formulated by means of phase-sensitive ray-tracing [41]. The blaze angle directs the light to the desired direction according to the laws of refraction. For constructive interference of all the wavelets emerging from the individual micro-prisms (in the sense of the Huygens-Fresnel principle [42]), their phase difference has to be an integer multiple M of 2π. In fact, the profile shape and the height of the phase steps are the only two essential conditions for the design of the surface relief function. The periodicity and regularity of a conventional blazed grating are a consequence of the simple formalism given by equations 3.1 and 3.2, but not a stringent requirement.

As long as the phase-condition is fulfilled, a blazed grating can be designed as an array of micro-prism with constant blaze-angle, but arbitrary size. Therefore, the vertical position of the individual zones needs to be adjusted in a way, that the emerging wavelets are at constructive interference. This is achievable, if the phase steps from zone to zone correspond to an integer multiple of 2π. In this fashion, only the most fundamental conditions for the compliance of the diffractive properties are taken into account. Figure 3.1a) illustrates an example for a phase function of a blazed grating with non-uniform zone sizes. In the following, we will refer to DOEs with such non-uniform zone sizes as elements with modulated zone sizes.

In order to investigate the basic optical properties of a blazed grating with modulated zone sizes, we fist develop a formalism for the description of the diffractive phase function $\Phi_D(x) = \Phi_{mod}(x)$, which can subsequently be translated into a physical profile by use of equation 3.2. For simplicity, we consider a regular blazed grating with N periods of length Λ as a starting point. According to the notations in figure 3.1a),the boundary position of each zone j is assigned with a new value x_j by the modulation $x_j = \Lambda(j + \epsilon_j \Delta_j)$, with $\epsilon_j \in [-1, 1]$ and $j = 1, ..., N + 1$. Δ_j accounts for the maximum allowed zone size variation. The values of ϵ_j can be arbitrarily distributed or optimized for a specific application. If we write the starting phase Φ_j of the j-th zone as

$$\Phi_j = \Phi_{j-1} + 2\pi M \left[\frac{x_j - x_{j-1}}{\Lambda} - 1 \right], \tag{3.3}$$

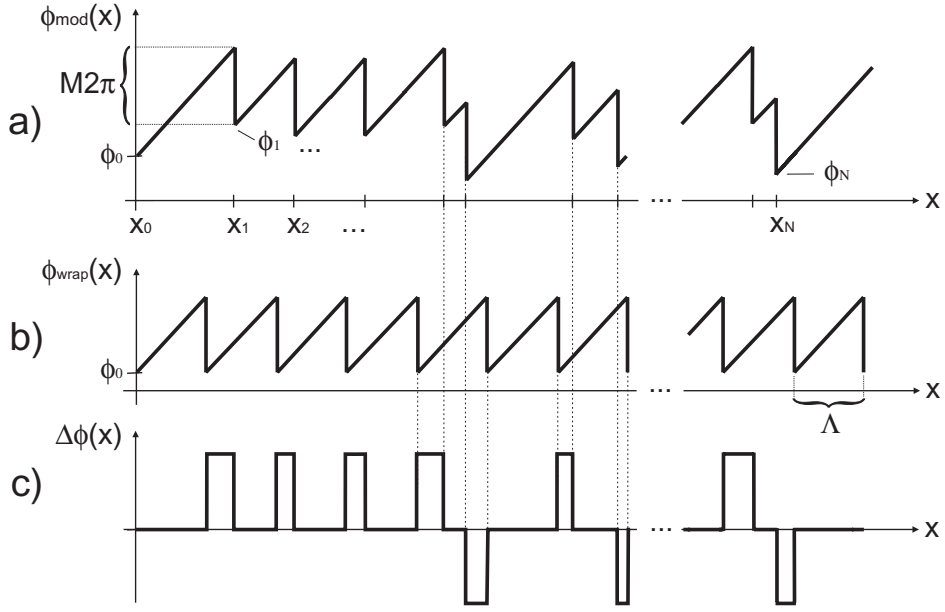

Figure 3.1: Decomposition of the zone-size modulated diffractive phase function a) into a linear b) and a binary component c).

with an arbitrary Φ_1, the phase function of this zone becomes

$$\Phi_{mod}(x) = \Phi_j + \frac{2\pi M}{\Lambda}(x - x_j) \quad for \quad x_j < x \leq x_{j+1}. \tag{3.4}$$

Therefore, it is guaranteed, that the phase steps between adjacent zones equal the factor $M2\pi$.

For a physical understanding of the diffractive properties associated with the phase function $\Phi_{mod}(x)$, we decompose it into the phase function $\Phi_{wrap}(x)$ of the corresponding regular blazed grating and a difference function $\Delta\Phi(x)$. Such a decomposition is depicted in figure 3.1. It is obvious from the drawings, that the difference function $\Delta\Phi(x)$ takes only discrete values. All phase steps are integral multiples of 2π. Therefore, it is readily seen, that superimposing the linear phase function of a regular blazed grating with a function of the form $\Delta\Phi(x)$, has no effect on the diffractive properties. Therefore, it is evident, that both function $\Phi_{wrap}(x)$ and $\Phi_{mod}(x)$ are equivalent in terms of scalar diffraction theory.

However, this statement only holds if the wavelength of the incident (monochromatic) field equals the design wavelength. In case of a wavelength deviation, $\Delta\Phi(x)$ is still a discrete function, but the phase steps are no longer an integral multiple of 2π. The phase function is then resembled by the linear component $\Phi_{wrap}(x)$, scaled by α and "disturbed" by the binary phase

component $\Delta\Phi(x)$. Consequently, the element with the modulated zone sizes exhibits a different spectral behavior.

Form this perspective, it becomes clear, that such an element acts not like mere scatterer which produces a random phase, but shows a clear diffractive behavior. It can still be classified as a diffractive optical element.

In sections 3.4 and 3.6, some of these effects will be discussed and exploited for an optimization of specific spectral properties of blazed gratings and diffractive lenses.

3.3 Efficiency modelling and optimization

For an evaluation of the diffractive properties of a DOE at wavelengths λ other than the design wavelength λ_0, we introduce a phase correction factor α [43], which is in general described as

$$\alpha = \frac{\lambda_0}{\lambda} \frac{n(\lambda) - 1}{n(\lambda_0) - 1} \beta. \tag{3.5}$$

The additional factor β accounts for a systematic constant phase error and can be used to model a fabrication error, for example [44]. If not otherwise specified, we set $\beta = 1$.

3.3.1 Linear blazed gratings

Assuming an infinitely thin phase element, the field emerging from the grating can be described in terms of its complex amplitude transmittance $t(x)$:

$$u^+(x, 0) = t(x)u^-(x, 0), \tag{3.6}$$

where $u^-(x, 0)$ is the field incident on the element and $u^+(x, 0)$ immediately behind the grating, in the plane $z = 0$. The transmittance function is given by

$$t(x) = \exp[i\alpha\Phi_D(x)]. \tag{3.7}$$

Taking advantage of a Fourier-optics approach [26, 27], the diffraction pattern in the far-field can be determined from the Fourier transform of the field immediately behind the grating:

$$U(\xi) = \mathcal{F}[u^+(x, 0)], \tag{3.8}$$

where ξ denotes the spatial frequency, which is associated with a direction cosine $\alpha = \lambda\xi$. In the Fraunhofer approximation [26], the irradiance distribution

in a transversal plane at distance z can be written as

$$I(x,z) \propto \left| U\left(\frac{x}{\lambda z}\right)\right|^2 . \tag{3.9}$$

In case of a periodic grating with period Λ, only a discrete set of spatial frequencies ξ_m arises. These frequencies are related to the corresponding diffraction orders by $m = \Lambda\xi$, The diffraction efficiencies of individual diffraction orders are obtained from the Fourier coefficients. If we assume an infinite periodic blazed grating, illuminated with a monochromatic plane wave, the diffraction efficiency of the m-th order becomes

$$\eta_m = sinc^2(M\alpha - m). \tag{3.10}$$

Now, we consider a blazed grating with modulated zone boundary positions, as described above. According to the notations used in figure 3.1, the complex amplitude transmittance of a grating with N zones can be written as

$$t(x) = \sum_{j=0}^{N-1} \exp\left[i\alpha\left(\Phi_j - \frac{2\pi}{\Lambda}M(x-x_j)\right)\right] rect\left[\frac{x-(x_{j+1}+x_j)/2}{x_{j+1}-x_j}\right]. \tag{3.11}$$

The *rect*-function is defined in reference [27]. If we consider an illumination with a plane wave of unit amplitude at normal incidence, the Fourier transform of $u^+(x,0)$ is identical with the Fourier transform of $t(x)$:

$$\begin{aligned} U(\xi) = \mathcal{F}[t(x)] = \sum_{j=0}^{N-1} \quad & \exp\left[i\alpha\left(\Phi_j - \frac{2\pi}{\Lambda}Mx_j\right)\right](x_{j+1}-x_j) \times \\ & \exp\left[-i\pi\,(x_{j+1}+x_j)\left(\xi - \frac{M\alpha}{\Lambda}\right)\right] \times \\ & sinc\left[(x_{j+1}-x_j)\left(\xi - \frac{M\alpha}{\Lambda}\right)\right]. \end{aligned} \tag{3.12}$$

Due to the generally non-uniform size of the individual zones, this spectrum no-longer consists only of the discrete diffraction orders m at spatial frequencies $\xi_m = m/\Lambda$. The non-uniform nature gives rise to the occurrence of additional discrete frequencies between the orders m, which are separated by a factor of $(N\Lambda)^{-1}$. The spectral width of these orders depends on the number of illuminated zones or on the width of the aperture, respectively. Mutual overlapping of these intermediate orders typically leads to an additional "ground noise". The normalized diffraction efficiency evaluated at frequency ξ is

$$\widetilde{\eta}(\xi) = \left(\frac{\Lambda}{x_N - x_0}\right)^2 |T(\xi)|^2 . \tag{3.13}$$

In this fashion, the efficiency $\widetilde{\eta}_m$, which corresponds to the diffraction order of the regular grating is given by $\widetilde{\eta}_m = \widetilde{\eta}(m/\Lambda)$. If $\alpha = 1$ is chosen, all intermediate frequencies vanish and the diffraction efficiencies are the same as for a regular blazed grating : $\widetilde{\eta}_m = \delta_{mM}$ (where δ_{mM} denotes the Kronecker-symbol).

3.3.2 Diffractive lenses

Now, we consider cylindrically symmetric diffractive lenses, in a way equivalent to the treatment of the blazed gratings with modulated zone sizes. Since we will investigate effects in beam focusing and collimation, we describe the incident field in a more general way as a Gaussian beam of width b (e^{-2}-convention [45]) and a wavefront radius of curvature R_c:

$$u_0^-(\rho, \varphi, 0) = \exp\left(\frac{-2\rho^2}{b^2}\right) \exp\left(\frac{i\pi\rho^2}{\lambda R_c}\right). \tag{3.14}$$

The field behind the thin lens, written as a function of the radial coordinate ρ and the angular coordinate φ is then (analogue to 3.6)

$$u_0^+(\rho, \varphi, 0) = t(\rho) u_0^-(\rho, \varphi, 0). \tag{3.15}$$

The zone boundary locations ρ_p of a conventional M-th order diffractive lens with N zones and a focal length f are determined by [3, 43]

$$\rho_p = \left[2fM\lambda p + (M\lambda p)^2\right]^{1/2}, \quad p = 1, ..., N, \quad \rho_0 = 0. \tag{3.16}$$

Within the p-th zone, the phase delay function is

$$\Phi_p(\rho) = \frac{2\pi}{\lambda_0}\left[(\rho^2 + f^2)^{1/2} - f - M\lambda(p-1)\right] \quad for \quad \rho_{p-1} \le \rho < \rho_p. \tag{3.17}$$

Thus, the overall complex amplitude transmission function within an aperture radius r_A can be constructed by a summation over the N zones:

$$t(\rho) = \sum_{p=1}^{N} C_p(\rho) \exp[i\alpha\Phi_p(\rho)], \tag{3.18}$$

with

$$C_p(\rho) = \begin{cases} 1 & \rho_p \le \rho < \rho_{p+1} \\ 0 & otherwise \end{cases}; \quad 0 \le \rho < r_A\,. \tag{3.19}$$

Again, the complex amplitude transmission function contains the phase correction factor α for the consideration of wavelength-dependent effects.

Within the paraxial approximation, the transmission function can be expanded into a Fourier series summed over the diffraction orders m [43, 46], which results in

$$\Phi(\rho) = \sum_{m=-\infty}^{\infty} \exp[-i\pi(M\alpha - m)] sinc(M\alpha - m) \exp\left(\frac{-i\pi m\rho^2}{Mf\lambda_0}\right). \quad (3.20)$$

Note that the last term in the above expression is equivalent to the Fresnel approximation $u_q(\rho, z)$ of a spherical wave, which has the quadratic phase function of a paraboloidal wave and can be written as

$$u_q(\rho, z) = \frac{A}{z} \exp(-ikz) \exp\left(\frac{-i\pi\rho^2}{\lambda z}\right). \quad (3.21)$$

It has a complex amplitude A and z denotes the distance from the origin. As a consequence, the diffractive lens represented by equation 3.20, can be regarded as a paraxial element with an infinite number of focal lengths. Thus, each diffraction order is associated with a focal length f_m, according to

$$f_m = \frac{Mf}{m}\frac{\lambda_0}{\lambda}. \quad (3.22)$$

The diffraction efficiency of the m-th order is given by the squared modulus of the Fourier coefficients in equation 3.20 and derives to

$$\eta_m = sinc^2(M\alpha - m), \quad (3.23)$$

which is exactly the same as in case of the the regular blazed grating (cf. equation 3.10).

Based on this analogy, it is straightforward to apply the concept of the zone size modulation to diffractive lenses as well. In the same way as for the blazed grating we now redefine or "modulate" the boundary positions $\rho_p \rightarrow \widetilde{\rho_p}$:

$$\widetilde{\rho_p} = \rho_p + \Delta_\rho \epsilon_p (\rho_p - \rho_{p-1}) \quad with \quad \epsilon_p \in [-1, 1]. \quad (3.24)$$

In doing so, the complex amplitude transmission function can be calculated by help of equations 3.17 and 3.18. Δ_p is again the maximum variation of the original zone size and should be chosen in such a way, that a minimum zone size which does not violate the validity of scalar diffraction theory. The index p indicates, needs not necessarily to be the same for each zone.

For the evaluation of the diffracted field in a transverse image plane at distance z from the lens surface, we employ the first Rayleigh-Sommerfeld

diffration integral [26, 47, 32]:

$$u_p(r,\vartheta,z) = \int_{r_{p-1}}^{r_p}\int_0^{2\pi} u_p(\rho,\varphi,0^+)\frac{\rho z}{\lambda R^2}\left(\frac{1}{kR}-i\right)\exp(ikR)d\varphi d\rho,$$
$$R = \left[z^2+r^2+\rho^2-2r\rho\cos(\vartheta-\varphi)\right]^{1/2}. \tag{3.25}$$

Hereby, we only integrate over the p-th zone. r and ϑ are the radial and azimuthal coordinates in the image plane, respectively. For the calculation of the resulting irradiance at an image point (r,ϑ,z), the contributions of all N zones must be coherently superimposed:

$$I(r,\vartheta,z) = \left|\sum_{p=1}^{N} u_p(r,\vartheta,z)\right|^2 \tag{3.26}$$

Since the numerical evaluation of the double-integral 3.25 for many image points can consume considerable computational time, we take advantage of the Gauss-Legendre numerical quadrature algorithm [48] for the integration along the radial, as well as the angular coordinate. For on-axis image points, expression 3.25 reduces to a single-integral.

3.3.3 Optimization by simulated annealing

For the improvement of specific diffractive properties of a zone-size modulated DOE, a non-linear optimization algorithm is required, in order to find an optimal set of the individual zone size variations ϵ. A typical task for such an algorithm is the optimization of the efficiency distribution among the diffracted orders or the shaping of the irradiance pattern in a given image plane.

For each specific case, an appropriate merit function has to be defined, upon which the progress of the optimization can be qualified. Due to the large number of zones (typically $\gg 10$) and considerable computational effort, a fast and efficient global optimization method is required. For all optimizations presented in this chapter, a simulated annealing (SA) algorithm, as introduced in section 2.3.3 has been employed.

3.4 Blazed gratings

A phase mismatch caused by a depth error (due to fabrication), or by an illumination with a wavelength other than the design wavelength, leads to the occurrence of multiple diffraction orders in the image space. For many

practical applications, only the design order is of interest and the other orders in most cases have a detrimental effect on the optical performance. Therefore, we will refer to non-design diffraction orders as "stray-light" diffraction orders in the following. The zone size modulation concept can help to suppress the rising of such stray-light diffraction orders for changing values of α.

3.4.1 Stray-light diffraction order suppression

We have performed an optimization of the wavelength tolerances for an example blazed grating with N=50 zones, designed for the first order. By use of a simulated annealing algorithm, the optimization aimed at the reduction of the diffraction efficiency of all orders $m \neq M$, while simultaneously keeping the efficiency η_M as high as possible. Therefore, the merit function to be minimized during the course of the optimization was formulated as the ratio between the efficiency of the most dominant stray-light order and the efficiency of the design order:

$$\gamma = \frac{max(\eta_{k \neq M})}{\eta_M}. \tag{3.27}$$

The shape of the profile resulting from the SA-optimization is illustrated in figure 3.2.

Figure 3.2: Profile shape of the zone-size optimized first order blazed grating (50 periods).

Figure 3.3 shows the calculated diffraction efficiency for this optimized grating and is regular-sized pendant, respectively. For the regular blazed grating , $\eta_m(\alpha)$ has the shape of a squared *sinc*-function, according to equation 3.10. This behavior is no longer valid for the zone-size modulated blazed grating . The larger the magnitude of the zone-size variations, the more significant becomes the deviation from the $sinc^2$-shape. The central lobes of the first order and the two neighboring orders are getting slightly narrower, but remain symmetric about the maximum value and still intersect at $\alpha = 0.5$ and $\alpha = 1.5$, respectively.

Note that the secondary lobes are almost vanishing in case of the optimized grating. Consequently, the occurrence of unwanted orders ($m \neq M$) for values of $\alpha \neq M$ is reduced. However, although additional losses of the main diffraction efficiency have to be tolerated, significant improvements of the factor γ can be achieved, as listed in table 3.1.

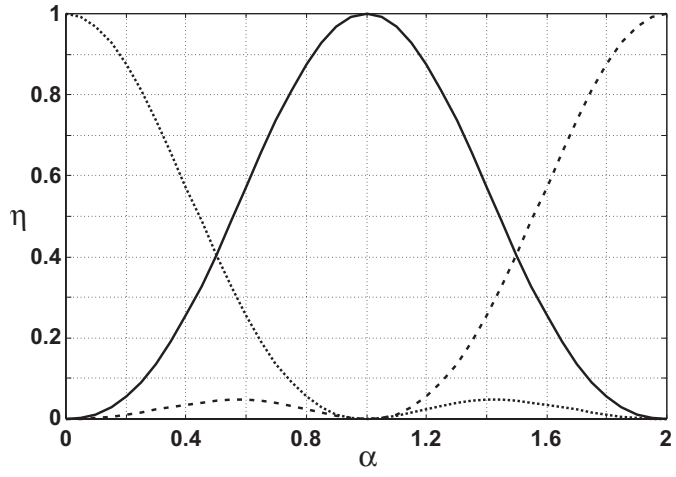

a)

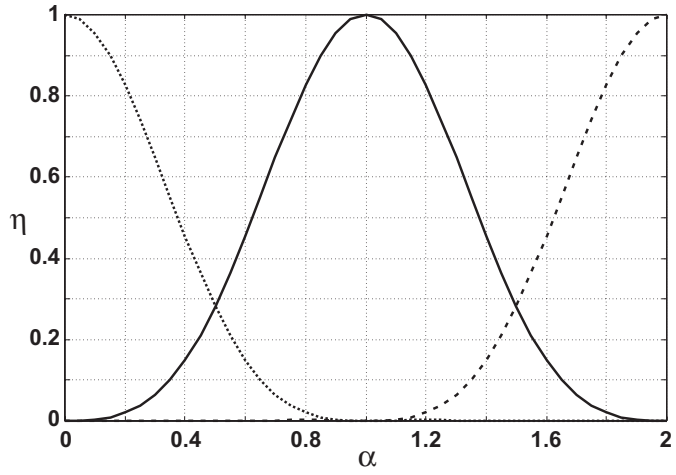

a)

Figure 3.3: Calculated diffraction efficiencies $\eta_m(\alpha)$ of a) a regular blazed grating and b) an example of an optimized zone-size modulated blazed grating for $M=1$, $m=0$ (dotted), $m=1$ (solid) and $m=2$ (dashed).

The calculated far-field diffraction pattern (Fraunhofer-approximation) of the regular and the optimized first order blazed grating are compared in figure 3.4. It is well discernible, that the efficiencies of the orders $M\pm1$ are significantly lowered, and the orders $M\pm2, \pm...$ are successfully suppressed in figure 3.4b). As already mentioned, there is an additional level of "noise" or stray-light between the discrete orders in figure 3.4b). However, the level of this stray-light is lower than $\eta=0.02$ and these frequencies have a narrow spectral spacing, since $N=50$ zones are illuminated.

Table 3.1: Values of γ for a first order regular blazed and the optimized zone-size modulated blazed grating .

$\alpha =$	0.7	0.8	0.9	1.0	1.1	1.2	1.3
non-optimized	0.184	0.063	0.012	0.000	0.012	0.063	0.184
optimized	0.099	0.024	0.003	0.000	0.003	0.024	0.099

3.4.2 Rigorous diffraction analysis

The initial idea of the zone-size modulation concept was derived from the principle of the thin-element approximation. On the other hand, DOEs with zone-sizes, which reach the order of magnitude of the wavelength have to be treated with rigorous vectorial diffraction theory. This can be the case for DOEs with large diffraction angles or for zone-size modulated elements with large maximum zone-size variations. Therefore, it is worth to study the diffractive properties of such elements with rigorous diffraction analysis.

Therefore we have taken a blazed grating with N=20 periods optimized for stray-light order suppression under conditions of wavelength deviations as an example. The zone-size modulated blazed grating is designed for the first order, $\lambda_0 = 0.633\,\mu m$ and optimized by simulated annealing (using scalar diffraction theory), in the same way as the grating described in section 3.4.1.

Figure 3.5 shows the rigorously calculated diffraction efficiency spectra for differently scaled period lengths $\Lambda = 10\,\mu m, 5\,\mu m$ and $3\,\mu m$ under illumination wavelengths of $\lambda = 0.4\,\mu m$ and $\lambda = 0.9\,\mu m$ (rigorous diffraction calculations have been again performed by Ilkka Kallioniemi).

The grating with $\Lambda = 10\,\mu m$ exhibits an excellent agreement of the calculated diffraction efficiency spectra with scalar results. In case of $\Lambda = 5\,\mu m$ and $\Lambda = 3\,\mu m$, the diffraction efficiencies show a deviation form the scalar results by a factor less than 0.05 for the first order and increase of the zeroth order less than a factor of 0.35, if $\lambda = 0.9\,\mu m$.

For $\lambda = 0.4\,\mu m$, η_2 increases by a factor of 0.25 by reducing the period from $\Lambda = 10\,\mu m$ to $\Lambda = 3\,\mu m$., while the first order is slightly reduced, simultaneously.

In addition, the efficiencies of the intermediate spatial frequencies agree very well with the scalar results for $\Lambda = 10\,\mu m$ and do not change significanly, while $\Lambda > 3\,\mu m$.

This example confirms, that the zone-size modulation principle is not necessarily only restricted to cases where $\Lambda/M \gtrsim 10\lambda_0$. Therefore, an aim for future work could be the combination of an appropriate algorithm for the zone-size optimization, such as simulated annealing with rigorous diffraction analysis.

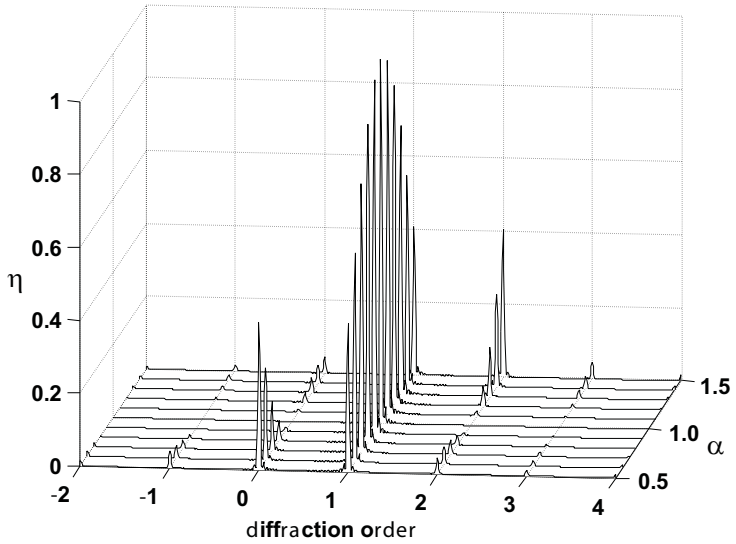

a)

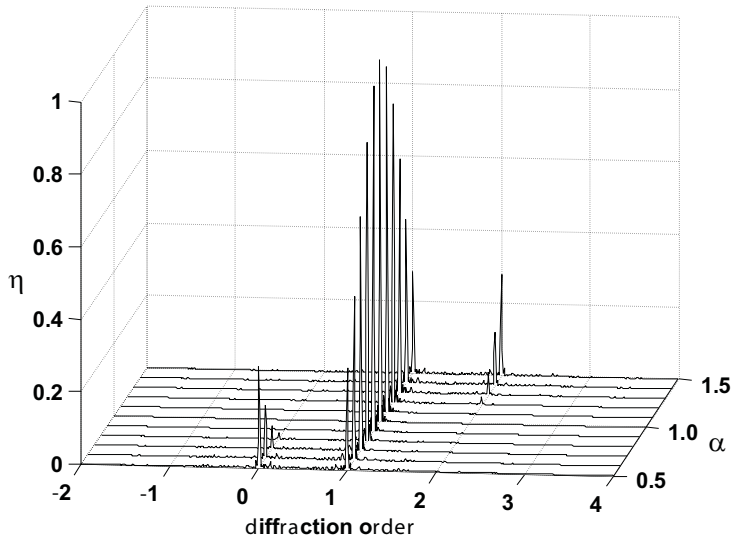

b)

Figure 3.4: Calculated scalar far-field diffraction spectra of a) a regular blazed grating and b) an optimized zone-size modulated blazed grating with 50 zones, for $\alpha = 0.5, ..., 1.5$. The peak amplitudes correspond to the respective diffraction efficiency .

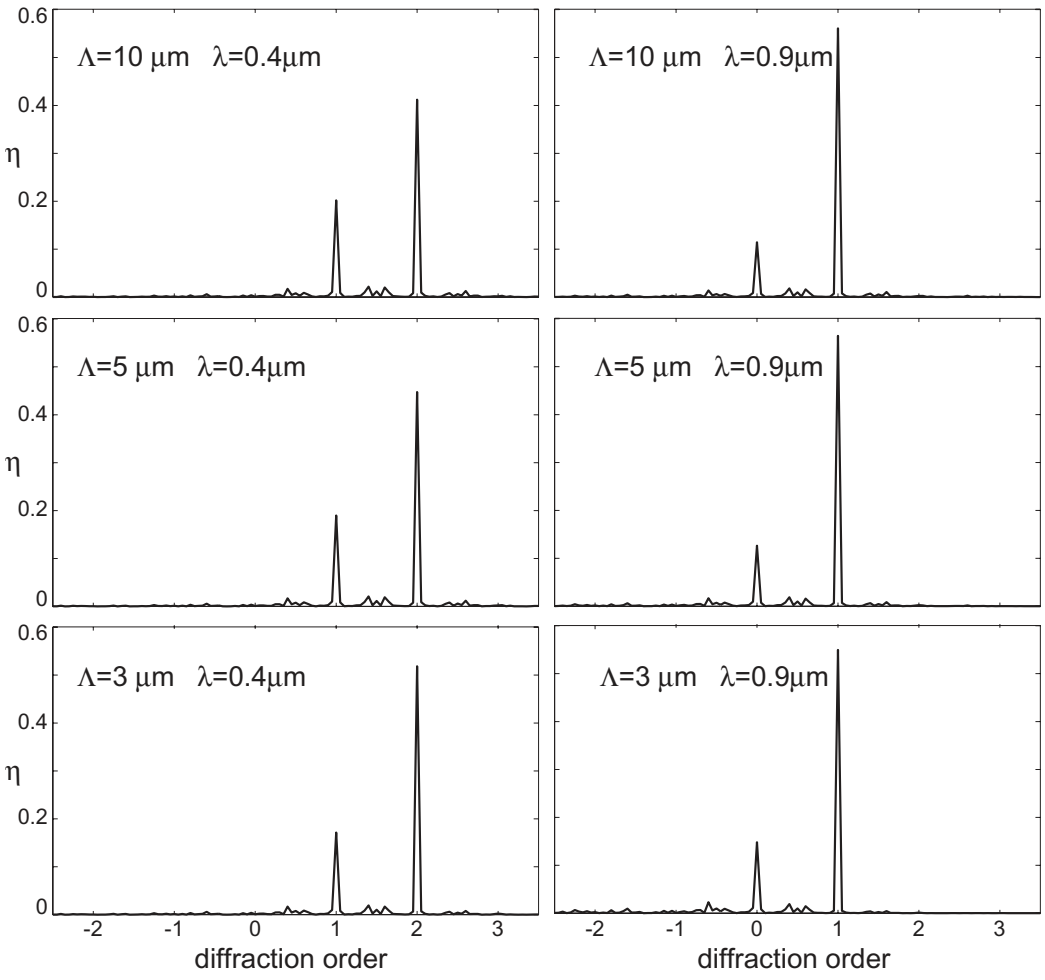

Figure 3.5: Rigorously calculated diffraction efficiency spectra of first order zone-size optimized blazed gratings with 20 periods, design for $\lambda = 0.633\,\mu m$. The plots show the same optimized grating with scaled period lengths of $\Lambda = 3, 5$ and $10\,\mu m$, illuminated at $\lambda = 0.4\,\mu m$ and $\lambda = 0.9\,\mu m$. The diffraction efficiencies are normalized to the sum of transmitted orders. Calculations carried out by Ilkka Kallioniemi.

3.4.3 Experimental results

In order to verify the theoretical results, the optimized zone-size modulated blazed grating and the corresponding regular blazed grating presented in section 3.4.1 have been fabricated by direct laser writing in positive photoresist ($n(\lambda_0) = 1.64$). The design wavelength is $\lambda_0 = 0.633\,\mu m$ (for a HeNe-laser) and the period $\Lambda = 40\,\mu m$.

In order to evaluate the α-dependence of the diffraction efficiency , the grating has been fabricated with different scalings of the design profile depth $d_{2\pi} = \lambda_0/[n(\lambda_0) - 1] = 0.99\,\mu m$, according to equation 3.2. The scaling factors β for the depth have been chosen as $\beta = 0.5, ..., 1.2$, in steps of 0.07. Since the illumination wavelength is constant, the resulting phase correction factor $\alpha = \beta$ (cf. equation 3.5).

The far-field intensity distributions for both gratings have been measured at a distance of $50\,cm$, with a scanning stage equipped with a photodetector and a slit-aperture. This measurements are shown in figure 3.6. Comparing the diffraction patterns with the theoretical results (figure 3.4) show a good agreement of the dispersion behavior (the α-dependence) and the relative efficiencies of the various diffraction orders. It is well recognizable, how the orders $m = -1$, $m = 2$ and $m = 3$ are suppressed with the optimized grating.

As expected, the efficiencies of the first and zeroth order of the regular blazed grating are approximately equal. The same holds for the non-regular blazed grating. However, the diffraction efficiencies of these diffraction orders are a factor of 1.3 higher for the regular blazed grating, compared to the other one.

Due to the use of a Gaussian laser beam, the number of effectively illuminated zones is less than 50, so that the spacial resolution or width of the peaks is lower than in the theoretical example. The resolution is further diminished by the finite with of the detector aperture (approximately $200\,\mu m$).

In addition, the noise level is slightly higher than theoretically expected. This is possibly caused by fabrication errors like surface roughness or the convolution effect (see chapter 2), which could direct light into the intermediate diffraction orders (which do not exist in the pure periodic case).

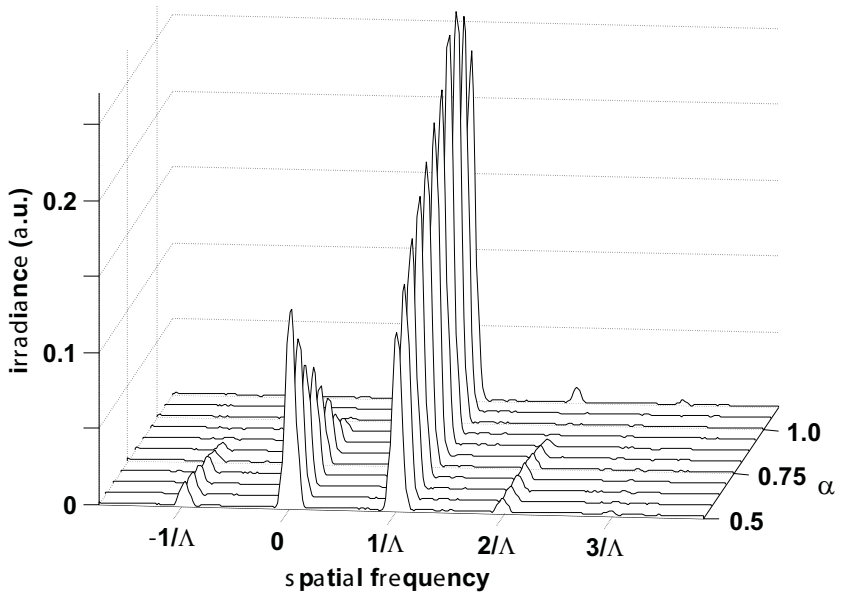

a)

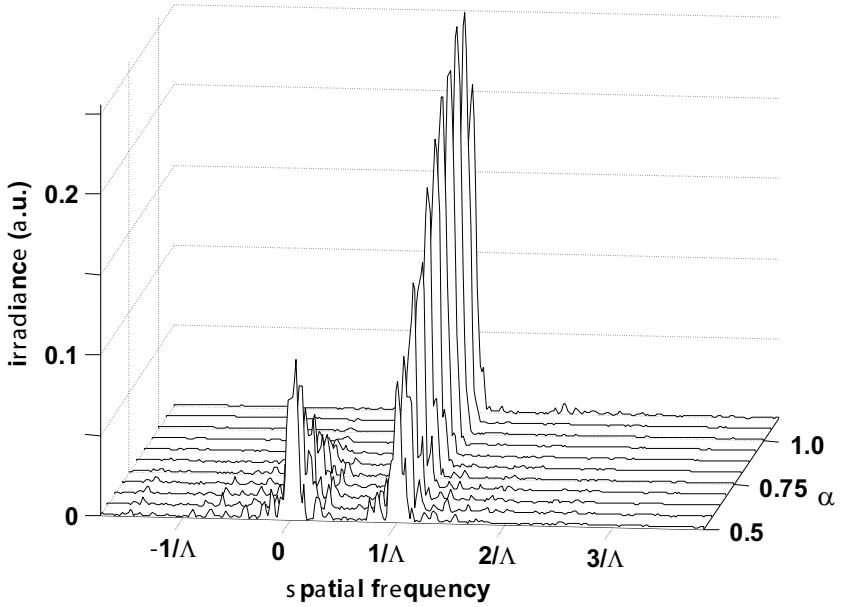

b)

Figure 3.6: Measured far-field diffraction spectra of a) a regular blazed grating and b) an optimized zone-size modulated blazed grating , for $\alpha = 0.5, ..., 1.2$.

3.5 Application to diffractive lenses

The optimization principle described in the previous section is also applicable to diffractive lenses. We will demonstrate examples for the improvement of a focusing as well as a collimating diffractive lens. Since the determination of the diffractive properties involves the evaluation of diffraction integrals of the form 3.25, the optimization (by simulated annealing) requires sufficient computation resources, depending on the number of zones and image points.

3.5.1 Focusing lenses

Diffractive lenses and blazed gratings exhibit a number of analogies. The zones at the outer regions of the lens are often approximated by local blazed gratings (see section 2.4). Furthermore, the efficiencies of the individual diffraction orders obey the same relation as the diffraction efficiencies of blazed gratings (equations 3.10 and 3.23). According to equation 3.22, the individual diffraction orders focus at different axial points.

Therefore, it seems obvious that the zone-modulation principle is also applicable to the suppression of stray-light orders (and thus the occurrence of unwanted focal spots), if a beam is focused with a diffractive lens. As an illustrative example, we have chosen a diffractive lens with a design similar to the ones used for the coupling of a multimode VCSEL beam into a fiber (as described in chapter 5).

The lens is designed for the second diffraction order with a focal length of $157\,\mu m$ at a wavelength of $0.85\,\mu m$. This corresponds to a replicated lens in Sol-Gel material with a refractive index of 1.54 and a thickness of $400\,\mu m$ on a VCSEL chip (see chapter 5) and a distance between VCSEL and fiber of $400\,\mu m$ (paraxial approximation). Within an aperture radius of $75\,\mu m$, the diffractive lens has 10 zones.

For the illumination, the multimode beam is approximated by a Gaussian shape with a divergence of 7° within the material. This corresponds to $b = 50\,\mu m$ and $R_c = 260\,\mu m$ (considering the refractive index change in the propagation medium), in the lens plane, according to definition 3.14. The diffraction pattern along the optical axis is determined by use of the thin element approximation and the zone-wise evaluation of the Rayleigh-Sommerfeld diffraction integral (cf. equation 3.25).

For this exemplary case, a reduction of focal spot intensities associated with stray-light diffraction orders due to the presence of a profile depth error is demonstrated. A deviation of the profile depth from the design value is a typical fabrication error [44].

Assuming a depth tolerance of ±10%, the individual zone sizes of the lens have been optimized for a scaling factor $\beta = 0.9$ by simulated annealing.

The calculated on-axis diffraction patters for this configuration at depth scalings of $\beta = 0.9$ and $\beta = 1.1$ are plotted in figure 3.7. The figure compares the non-optimized and optimized lenses for each scaling.

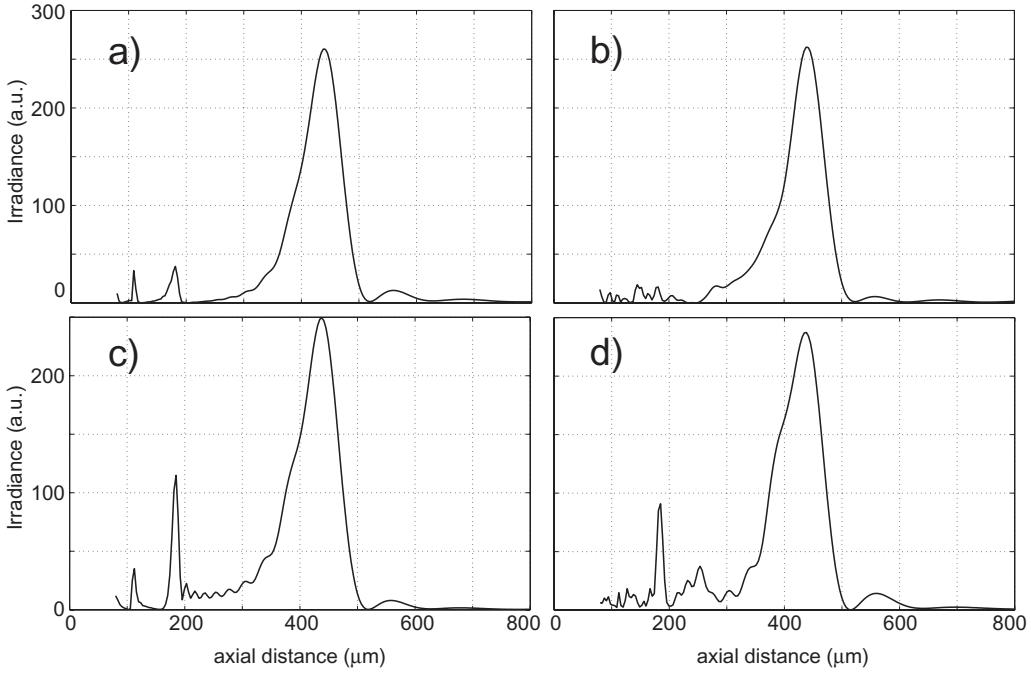

Figure 3.7: Calculated on-axis irradiance distributions of second order diffractive lenses with a focal length of $157\,\mu m$ and an aperture radius of $75\,\mu m$ under Gaussian beam illumination ($b = 50\,\mu m$). a) and b) compare the non-optimized and optimized lenses at $\beta = 0.9$; c) and d) compare the non-optimized and optimized lenses at $\beta = 1.1$, respectively.

As the lens is optimized for $\beta = 0.9$, the most significant suppression of the additional focal points is achieved at this value. The peak focal intensities of the third and fourth diffraction order - the two smaller peaks in figure 3.7a) - are lowered by a factor better than 2, while the shape and height of the main peak remain almost unaffected. Similar to blazed gratings, a low level of additional peaks occur in between the main orders.

A reduction of the additional foci with the optimized lens is also achieved for $\beta = 1.1$, although the suppression is less significant and the peak intensity of the design focus is slightly reduced. The improvement holds for the whole range $\beta = 0.9, ..., 1.1$ (at $\beta = 1.0$, optimized and non-optimized lenses produce identical intensity distributions).

In order to give another example for the optimization of diffractive lenses, we apply the zone-size modulation principle to an exemplary collimation problem in the following section.

3.5.2 Collimating lenses

A beam collimated with a diffractive lens is particularly sensitive to wavefront aberrations [45, 40] and also to wavelength deviations. Light diffracted into orders close to the design order is propagating within the "signal window" (the area of the collimated beam) over much larger distances behind the lens than it is the case for focusing lenses.

The mutual interference of the present diffraction orders leads to undesired effects over a large range of propagation [40, 49]. Such effects have to be taken into account for the design of applications, which rely on a high beam quality.

As a example, we will investigate the irradiance distribution of a Gaussian beam with $b = 180\,\mu m$ and a wavefront curvature radius $R_c = 4\,mm$ in the lens plane. The collimation is accomplished with a first order diffractive lens with a focal length of $4\,mm$ designed for $\lambda_0 = 0.633\,\mu m$, so that the waist of the collimated beam lies in the lens plane.

The lens design is identical to the one described above for the focusing of plane waves. Figure 3.8 a) illustrates the irradiance distribution for $\lambda = 0.7\,\mu m$ ($\alpha = 0.9$) at an axial distance $z = 2f$. The dashed curve indicated the (fitted) shape of the ideal Gaussian profile.

The irradiance pattern in figure 3.8 a) differs significantly from the ideal Gaussian distribution. Particularly in the central region, the intensity tends to oscillations already for small phase errors of the diffractive lens [40], which leads to a high sensitivity to wavelength deviations.

Consequently, the use of diffractive lenses for applications with high beam quality requirements is limited to a very small spectral range. For example, a wavelength deviation by a factor of 0.01 has already a significant effect on the quality of a collimated Gaussian beam [40, 45] (see also publication II).

Thus, we employ again the zone-size modulation concept in order to improve the diffractive performance under conditions of wavelength deviations. The above conventional diffractive lens design is again optimized by simulated annealing. The deviation of the irradiance distribution in the image plane ($z = 2f$) from the ideal Gaussian function serves as a quality criterion. Since the width of the collimated beam in the image plane is wavelength-dependent, the mean square error (MSE) of the irradiance with respect to a Gaussian fit function is used for this purpose.

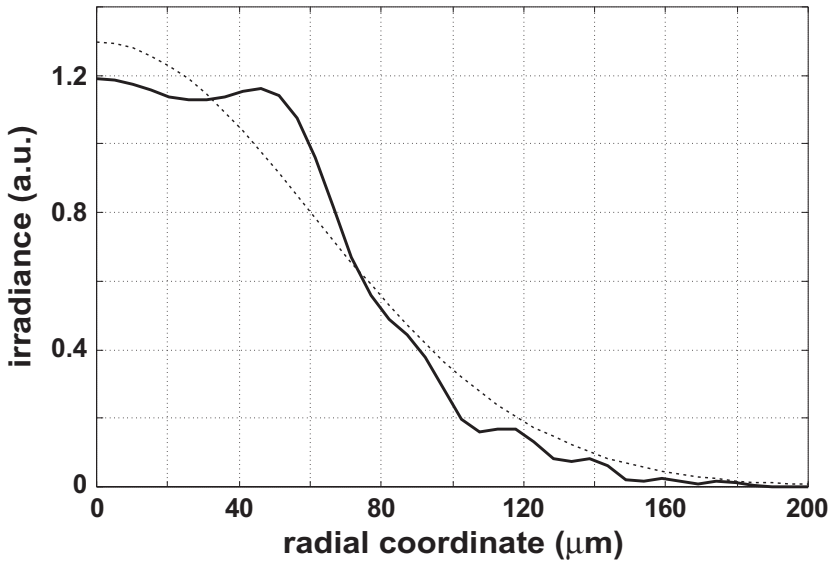

a)

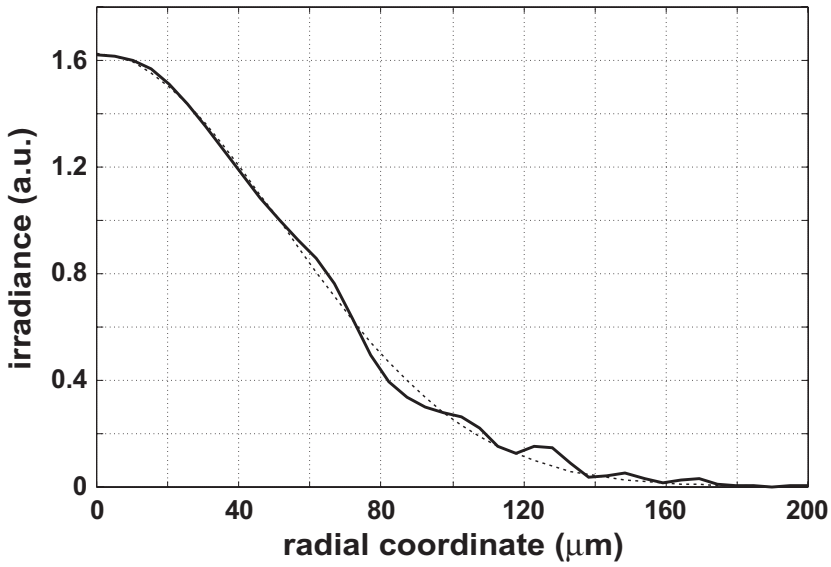

b)

Figure 3.8: Calculated lateral irradiance distribution of a Gaussian beam at $z = 2f$, collimated with a) a non-optimized diffractive lens and b) an optimized diffractive lens.

The diffraction properties of the lens are optimized for a spectral range $\lambda_A > \lambda_0 > \lambda_B$. Therefore, the merit function for the SA-optimization is defined as a weighted sum of the mean square errors at λ_A and λ_B.

In our example, the diffractive lens is improved for $\lambda_a = 0.575\,\mu m$, $\lambda_b = 0.7\,\mu m$ and a maximum relative zone-size variation factor $\Delta_\rho = 0.3$. The irradiance distribution of the optimized lens at $\lambda = 0.7\,\mu m$ is shown in figure 3.8 b). Compared to the conventional diffractive lens, the beam shape is significantly improved.

The improvement of the beam quality holds for the entire optimization range $[\lambda_A, \lambda_B]$. Table 3.2 list some values for the MSE of the conventional and the optimized diffractive lens for different wavelengths (a more detailed list can be found in publication II).

Table 3.2: Calculated MSE (arbitrary units) of a conventional and a zone-size modulated diffractive lens, optimized for $\lambda = 0.575, ..., 0.7\,\mu m$ and $\lambda_0 = 0.633\,\mu m$. $f = 4\,mm$, $r_A = 400\,\mu m$, $b = 180\,\mu m$ and $z = 2f$.

α	$\lambda(\,\mu m)$	MSE non-optimized	MSE optimized
0.90	0.700	0.089	0.030
1.00	0.633	0.000	0.000
1.10	0.575	0.125	0.074

The table also shows, that the improvement is more significant for wavelengths $\lambda < \lambda_0$, while the beam abberations are higher for shorter wavelengths. Therefore, if optimizing a predefined spectral range, the optimum choice for the design wavelength is not necessary in the center of the range - depending on application specific requirements.

It has to be noted that for an illumination with a Gaussian beam the influence of the zone boundary positioning is decreasing with the distance from the beam center. Qualitative observations have shown that zone-size variations have negligible effect on the beam quality when the local field intensity drops below a factor of ≈ 0.1 of the peak amplitude ($r \gtrsim 1.2b$).

On the other hand, the lens aperture radius r_A should be at least $2b$, in order to avoid aperture diffraction effects [45].

This circumstances should be taken into consideration for the design and impose certain limitations of the design parameters. The choice of the first or second diffraction order can be advantageous in order to obtain a sufficient number of zones for the optimization in the central region of the lens.

3.6 Conclusions

The concept of zone size modulation provides an additional degree of freedom for the design of DOEs within the domain of scalar diffraction theory. Simulations by rigorous diffraction analysis showed similar results for blazed gratings with periods $\Lambda/M \lesssim 10\lambda_0$. The suppression of unwanted diffraction orders with blazed gratings could be successfully demonstrated by theoretical optimization results and have been confirmed by experimental measurements.

Furthermore, the concept was theoretically applied to focusing and collimating diffractive lenses. In analogy to blazed gratings, the presence of stray-light diffraction orders for wavelength other than the design wavelength could be significantly decreased by zone-size optimization. The same holds for the quality of a collimated Gaussian beam.

Chapter 4

Fabrication and replication of deep photolithographic micro-structures

The low-cost production of micro-optical elements and optical micro-systems in large quantities is typically assured by the use of standard fabrication technologies. However, for specific applications, for which deep optical or mechanical structures are required, standard methods are not always appropriate. To overcome the problem of cost-ineffectiveness, the use of replication techniques is one possibility [13, 3].

This chapter introduces two application examples for a non-standard origination of deep micro-structures for subsequent replication: The production of mid-infrared diffractive optical elements for injection molding and the fabrication of mechanical fiber-guides for the UV-casting replication (using a Sol-Gel material) on VCSEL chips or wafers.

4.1 DOEs for infrared applications

Diffractive optical elements (DOEs) have found many applications in the visible wavelength range. Elements for the mid infrared ($\lambda \approx 8-12\,\mu m$) typically have lower requirements on the lateral resolution of the fabrication technology, but require the use of different materials.

The profile depths of DOEs designed for this wavelength range are typically in the order of $d = 2-5\,\mu m$, when high refractive index materials such as germanium (Ge) or zinc selenide (ZnSe) are used (refractive indices at $\lambda = 10\,\mu m$: $n_{Ge} = 2.4$, $n_{ZnSe} = 4.0$). This depth range is covered by standard photoresist processing and etch techniques [50].

On the other hand, plastic materials such as polyethylene (PE), with a low absorption in the infrared, offer the potential for low cost elements fabricated by facilitating the use of replication techniques such as hot embossing or injection molding [13, 3].

The main consequence of using plastic materials is the increase of the profile depth up to $20\,\mu m$, due to their low index of refraction (PE: $n=1.51$ at $\lambda = 10\,\mu m$). The conventional fabrication of deep profile DOEs of this kind is typically accomplished by surface micro-machining techniques, such as single point diamond turning [51]. That way, extremely fine surfaces with deep profiles can be achieved. However, for more sophisticated structures without rotational symmetry or arrays of optical elements, photolithographic masking or direct writing techniques are favorable.

Therefore, the ability to fabricate deep micro-structures by photolithography is the key for applying plastic diffractive optics in the mid-infrared wavelength region. Since such continuous-relief profile depths are beyond the limits of standard lithography techniques, special emphasis has to be put on the optimization of film preparation and exposure parameters.

In the following, we will describe the fabrication of photoresist structures up to $20\,\mu m$ depth by direct laser writing (see chapter 2) and present its application to a passive infrared detector system.

4.1.1 Thick resist lithography by direct laser writing

For the standard fabrication of direct laser written micro structures, photoresist films of typically $d=2-4\,\mu m$ are used [52, 13]. In order to evaluate the processing of deeper structures in resist layers with a target thickness $d = 20\,\mu m$, films of high-viscosity positive photoresist were spun on glass substrates in a single step.

The film was exposed at a wavelength of $0.442\,\mu m$ using a high-quality microscope objective with a numerical aperture of 0.65. The diameter of the focal spot was in the order of $0.8\,\mu m$ (full width at half maximum). For a sufficient exposure of the resist layer, intensities in the order of $10^4\,W/cm^2$ (which corresponds to doses in the order of $500\,mJ/cm^2$ for a single pixel written with a scan speed of $50\,mm/s$) were required, which is $10-20$ times higher than for the standard thin-film exposure. Due to the high beam intensity, the level of stray light in the laser writing system had to be reduced, in order to avoid an increased surface roughness in exposed, as well as unexposed regions after development.

As another consequence of the high exposure doses and the high film thickness is the requirement for a careful spin-coating and soft-bake of the resist layer [53]. An insufficient soft-bake results in an increased surface

roughness after development or even film degradation already during exposure [54]. The soft-bake procedure also affects the uniformity of the layer thickness and the stress in the film. The time and the temperature had to be optimized. In addition, a successive ramping up of the temperature an a slow cooling down was required.

Thick photoresist films have additional consequences for the laser writing process that result in a reduction of the resolution [55, 56]. First, the bulk absorption effect of the photoresist reduces the effective dose at the bottom of the film and thus leads to a decreasing etch rate during the course of the development. Second, simulations on similar photoresist materials show that the wet etch process has an isotropic character, which causes smoothed and sloped profiles of originally sharp transitions in the exposure characteristics. Third, the depth of focus of the writing beam, which is in the order of two times the Rayleigh range ($\approx 3\,\mu m$), is significantly smaller than the film thickness. It is therefore obvious that a focusing of the writing beam on the photoresist surface will not lead to optimum results.

It has been shown [55, 56], that the aspect ratio of thick resist microstructures produced by wafer-stepper exposure can be improved by an offset of the focus position. Similar results have been found for direct laser writing.

Figure 4.1 a) shows a scanning electron microscope (SEM) image (cross-section) of a single exposure scan line for a writing beam focused at the resist surface. The resulting profile after development has an undercut sidewall shape. The width of the groove increases with the depth to a maximum of approximately $4\,\mu m$. At the surface, the width is approximately half this value and the depth of the groove is $10\,\mu m$. It has to be noted, that the exposure intensity chosen for the single lines corresponds to the value, which is required for the thorough exposure of a $20\,\mu m$ thick layer with consecutive lines with a pitch of $0.4\,\mu m$ (given by the resolution of the writing system).

In figures 4.1 b) and 4.1 c), the corresponding views of single lines with a defocusing of $5\,\mu m$ and $7\,\mu m$ towards the substrate are shown, respectively. The latter exhibits a significant sloping effect and an almost v-shaped groove profile with a width of $5\,\mu m$ and a depth of $7\,\mu m$.

The grooves written with the $5\,\mu m$ defocusing are $4\,\mu m$ wide and $10\,\mu m$ deep. The cross sectional profile represents a good compromise between the two other examples and has been chosen for the fabrication of the DOEs. The effective writing spot size therefore was in the order of $4\,\mu m$ (see chapter 2) for definition).

The results for the different focal positions show analogies to the simulations of thick photoresist lithography with wafer-stepper exposure presented in reference [55].

The writing of multiple lines at a distance of $0.4\,\mu m$ yields a profile as

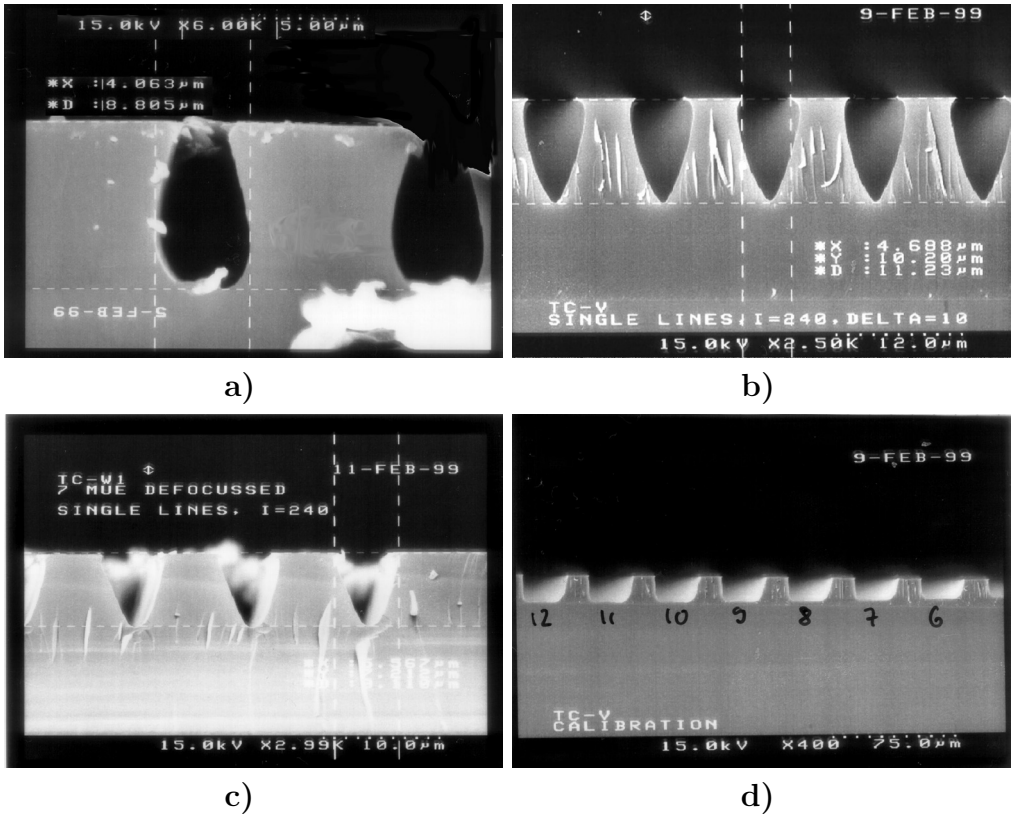

Figure 4.1: Scanning electron microscope (SEM) images (cross-sectional view) of direct laser written structures in $20\,\mu m$ thick photoresist films. Single scan lines, written with a) $0\,\mu m$, b) $5\,\mu m$ and c) $7\,\mu m$ spot defocusing (towards substrate) and a line pitch of $10\,\mu m$; d) $25\,\mu m$ wide calibration grooves.

depicted in figure 4.1 d). It shows calibration grooves of $25\,\mu m$ width and a depth of $12-20\,\mu m$ (from right to left). The $20\,\mu m$ deep groove was written with the same intensity as the examples shown in figure 4.1 a-c) and a focus offset of $5\,\mu m$. Due to the mutual overlapping of the exposure profiles of individual scan lines, the resulting structure is approximately twice as deep as a single line groove.

It has to be noted that the choice of a focusing objective with a smaller numerical aperture did not yield a better resolution, although the focal depth was increased. A qualitative experimental analysis has shown that the objective with a numerical aperture of 0.65 provided the best trade-off between spot size and focal depth.

Based on the measured depth values of a test structure similar to figure

4.1 d), consisting of a series of grooves written with different intensities, a lookup table has been build for the calibration of the exposure profiles for arbitrary structures.

For the evaluation of the lateral resolution of deep continuous reliefs, blazed gratings with a design depth of $20\,\mu m$ have been fabricated with different periods. Figure 4.2 shows cross-sectional scanning electron micrographs of gratings with $20\,\mu m$, $30\,\mu m$ and $40\,\mu m$ period lengths.

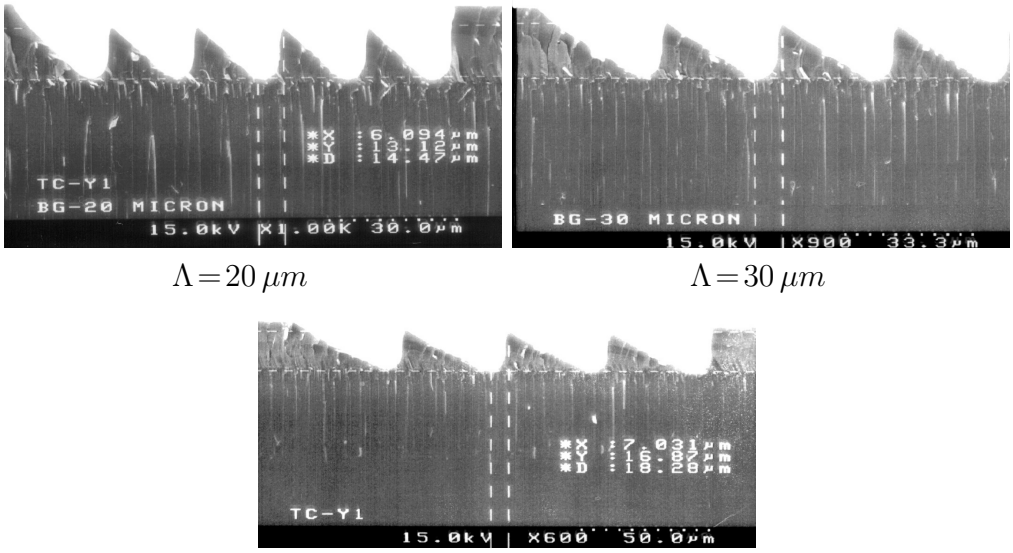

$\Lambda = 20\,\mu m$ $\Lambda = 30\,\mu m$

$\Lambda = 40\,\mu m$

Figure 4.2: Cross-sectional scanning electron micrographs of direct laser written blazed gratings with a design depth of $20\,\mu m$ and periods of 20, 30 and $40\,\mu m$.

It is well perceptible, how the profile steps are smoothed due to the convolution with the large effective writing spot. The affected area is approximately $6-7\,\mu m$ wide. As a consequence of the smoothing, the profile depth decreases with the period of the grating (depends on the blaze angle). The slopes of the gratings prove an excellent linearity, accomplished by the exposure calibration. For mid-infrared applications, the extend of the smoothed profile transitions is in the order of one wavelength .

As might be supposed, a compensation of the convolution effect (as described in chapter 2) provides no improvement for this kind of structures. For a sufficient compensation, the resist layer thickness must be significantly larger than the design profile depth. However, choosing a resist layer with a thickness $d \gtrsim 25\,\mu m$ would result in a significantly lower lateral resolution due to higher exposure doses and in additional difficulties with the resist

processing.

4.1.2 Diffractive lens array

The technology described in the previous section has been utilized for the origination of diffractive lens arrays for an infrared intrusion-detection application with custom directional characteristics.

An array of 24 first order anamorphic diffractive lenses have been fabricated over an area of $40 \times 50\,mm$. The lenses have been designed for a wavelength of $\lambda_0 = 10\,\mu m$, considering the thermal emission spectrum of an object with a temperature of $25°C - 30°C$ and the sensitivity of a pyroelectric detector. For a subsequent replication into polyethylene (by injection molding), the design depth for λ_0 was $\approx 20\,\mu m$.

Figure 4.3 shows a surface profiler scan of an example lens, direct laser written in photoresist. The measured profile shape is compared to the design function and shows good agreement at the profile slopes. At the central zone, the profile deviations are higher than in the outer zones. However, the maximum deviation at the slopes is below $\pm 1\,\mu m$, which corresponds to $\lambda/10$.

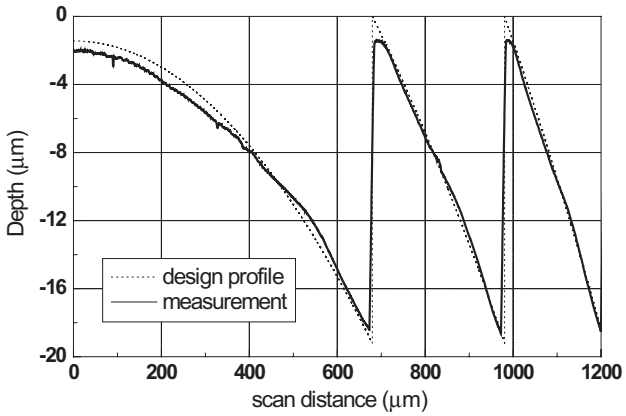

Figure 4.3: Surface profiler scan of an example lens (solid line), compared to the design profile (dotted line).

The vertical and horizontal focal lengths of the individual lenses are optimized for the recognition of a human intruder. The horizontal focal length determines the observation range (typically $10-15\,m$) and varies from $10-25\,mm$ over the whole array. By setting the vertical focal length to a higher value (typically up to $80\,mm$) the optical signal of an IR source with a predominantly vertical shape (human body) can be increased, compared

to a source with a horizontal form (pets). In the final product housing, the lens is mounted on a curved surface, which assures an angular observation range of approximately 90°.

The original lens array in photoresist is depicted in figure 4.4 a). After formation of a nickel shim [52], the device has been mass fabricated (by a customer) via injection molding in PE. Figure 4.4 b) shows a sample of the final product.

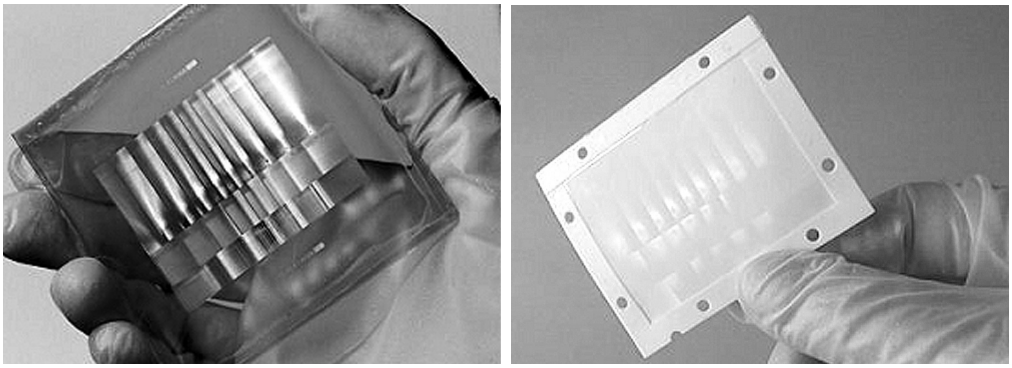

a) **b)**

Figure 4.4: Diffractive lens array for passive infrared detector application: a) Original structure in photoresist, b) final product, injection molded in PE.

Based on the direct laser writing of deep micro-structures, the photoresist processing has been extended to the fabrication of alignment features by conventional mask-aligner exposure, primarily for optical fibers. The following section outlines the concept and processing of such fiber alignment structures and deals with its replication on VCSEL chips or wafers.

4.2 Fiber guiding structures

The fabrication of optical microsystems requires the precise alignment of optical microsystem components such as fibers, microlenses and other micro-optical components with respect to other components or to optoelectronic devices (e. g. laser diodes, VCSELs, detectors, optical waveguides). This can be accomplished in various ways, including the etching of grooves into glass substrates or silicon wafers for the placement of the components. The fabrication of such supporting substrates and the mounting of components on them often requires time and cost intensive techniques. Typical structures used for this purpose, such as V-grooves are also not optimal for aligning

components oriented vertically to a wafer or device plane, for example a fiber or a fiber array to devices on a wafer.

For a cost-effective production, passive alignment techniques are preferred in which the components can be simply inserted into mechanical alignment structures produced during or subsequent to the basic microsystem or device fabrication process. An active alignment of the components typically results high precision, but is generally time consuming and not suitable for wafer scale processing.

A particular interest in the scope of this thesis is the passive alignment and assembly of optical fibers and fiber arrays on VCSEL chips. Some of the established methods and our approach using diffractive lenses integrated on the chip are described in chapter 5. In the following section, we demonstrate the concept and fabrication od smooth-edged mechanical fiber guiding structures for on-chip integration.

4.2.1 Fiber guide concept and fabrication

We describe a simple method for the fabrication of smooth-edged fiber guiding structures for monolithic integration with the VCSEL chip. These structures have a pure mechanical functionality and serve as an optical subassembly to guide an optical fiber in place and to enable a simple fixing with a suitable adhesive or encapsulation material. Therefore, a passive alignment is accomplished.

For this purpose, they have a circular symmetric groove shape with rounded edges at the top and require a minimum thickness $d \approx 50\,\mu m$, to provide a sufficient mechanical stability. Figure 4.5 schematically illustrates the shape of the guiding structures, which are replicated on top of a VCSEL chip. It also depicts inserted and encapsulated fibers.

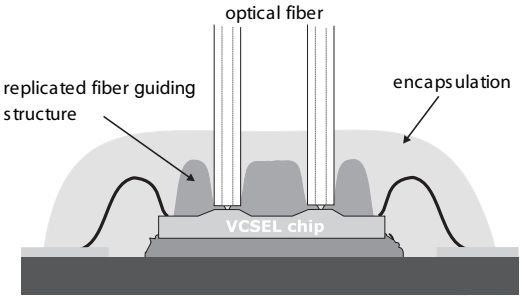

Figure 4.5: Schematic cross-section view of a VCSEL chip with integrated fiber guides and inserted and encapsulated fibers.

The structure has been lithographically originated by thick-film positive

photoresist processing. We have processed resist films with a thickness up to $d = 70\,\mu m$. As already mentioned in section 4.1.1, such ultra-thick resist layers require a careful soft-bake procedure with an appropriate temperature ramp cycle. The exposure of the film has been carried out using a standard mask aligner.

A thermal reflow cycle with optimized parameters after development accomplished the desired smooth-edged profile for a facilitated fiber insertion. For the determination of the optimum groove diameter for use with a $125\,\mu m$ diameter fiber, a lithography mask with different scalings of the structure have been used. Empirical tests have shown, that a hole diameter of $128\,\mu m$ on the mask yields the best results for the chosen lithography process. Figure 4.6 shows a microscope image of a 1×2 array of fiber guide structures with a separation of $250\,\mu m$ and a hole diameter of $128\,\mu m$ on a glass substrate after thermal reflow.

The layout dimensions for the guiding structure can be adapted to the layout of the VCSEL chip. Other samples with vertical vias in the ring of the guide have been fabricated. Such a layout facilitates the dispensing of the adhesive for the fiber attachment and lowers the risk of bubble formation

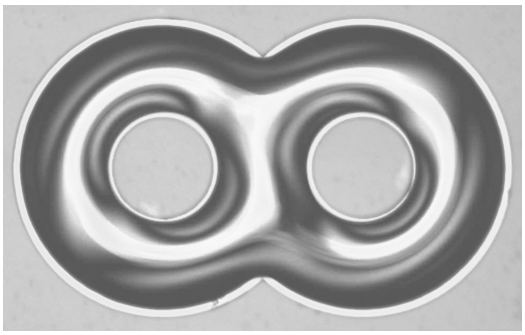

Figure 4.6: Microscope image of a test sample. A 1×2 array of fiber guides in photo resist with an inner hole diameter of $128\,\mu m$ is shown (after thermal reflow).

Due to the lithographic processing, custom arrays of fiber guides can be produced. In the course of this thesis, only discrete chips have been processed. However, the aim of the work is to extend the method to wafer scale processing. This can be accomplished either by direct processing of the device wafer [57] or by transferring the structure via a replication process. Optical fibers can then be passively inserted and subsequently encapsulated with the device.

The following section briefly outlines the replication of the guiding structures by a UV-casting process and the insertion of the fiber.

4.2.2 Replication and assembly

First experiments have been carried out with individual $850\,nm$ multimode VCSEL chips with 1×2, which have a separation of $250\,\mu m$. The devices have been die-bonded on a ceramic chip carrier substrate and wedge wire-bonded. The diameter of the effectively emitting surface is approximately $10-12\,\mu m$. A detailed description of the emission characteristics of the used devices can be found in sections 5.2.1 and 5.2.2.

For the replication transfer of the guiding structures to the chip surface, a UV-casting process using ORMOCER® [58] materials has been employed. This method will be described in more detail in section 4.3. The positioning of the replication mold with respect to the chip during the UV-casting has been accomplished using a cartesian robot.

In this manner, lateral alignment tolerances better than $\pm 5\,\mu m$ and a distance between the laser aperture and the bottom of the alignment grooves smaller than $10\,\mu m$ could be achieved.

For a production at wafer scale level, the UV-casting process can be done with help of a modified conventional mask aligner system [59]. This allows a precise alignment with the wafer. In addition to the relief transfer, the casting-mold for a wafer scale process must also have lithographic functionality, in order to spare out vias for wire bonding and dicing (sawing).

After replication, the fiber has been attached with assistance of a manual three-axis translational stage. The required visual pre-alignment has been accomplished using a microscope or imaging system, respectively. Then, the fiber has been inserted by pushing it into the "bore" of the structure. The rounded conical shape assists the guiding of the fiber and thus, enables a passive alignment. For the dispensing of an optical adhesive, the fiber has been vertically withdrawn again. Finally, after slow re-insertion, the adhesive has been cross-linked by UV exposure.

Figure 4.7 shows a photograph of the above mentioned test sample with inserted and encapsulated fibers.

The fiber coupling efficiency (normalized to the total output of the VCSEL) has been measured as a function of the driving current. The results for the two lasers are plotted in figure 4.8. Using a cleaved standard multimode step-index fiber with a core diameter of $50\,\mu m$ and a numerical aperture of 0.20, we could achieve maximum coupling efficiencies between $\eta = 0.8$ and $\eta = 0.9$ while the maximum fiber launch power at $I = 10\,mA$ was 1.0–1.2 mW. The maximum value as well as the decrease in coupling efficiency for currents $> 5\,mA$ are comparable to the coupling of an unprocessed VCSEL (in air) to a fiber placed at an lateral position, which yields the maximum efficiency and a distance of $5-10\,\mu m$ from the chip surface.

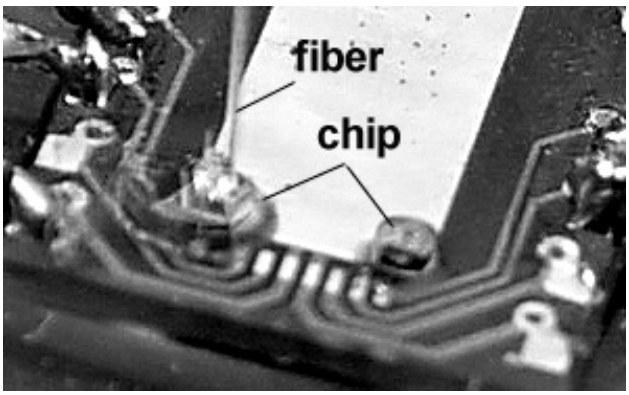

Figure 4.7: Picture of a VCSEL chips mounted and wire bonded on a test chip carrier substrate and a fiber attached to one chip. The chips are equipped with replicate fiber guides.

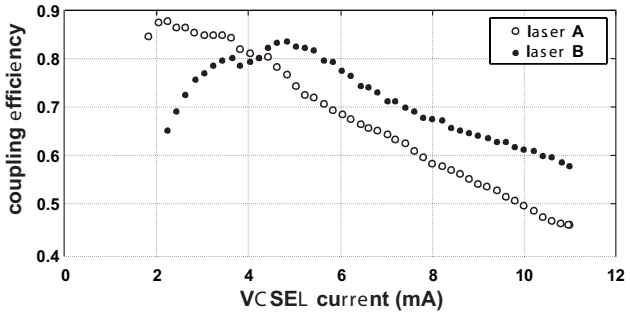

Figure 4.8: Measured coupling efficiencies of a 1×2 multimode VCSEL array into cleaved standard multimode step-index fibers with $50\,\mu m$ core diameter and NA=0.20. The fibers have been attached by help of on-chip replicated fiber guides.

The pre-alignment, insertion and encapsulation of the fiber with the guiding structures can also be performed in an automated or semi-automated setup (e. g. a pick and place robot). A similar approach is described in reference [57].

4.3 Chip-level replication by UV-ORMOCER casting

The replication of microstructures in organic UV-photopolymer materials such as optical adhesives is a well known fabrication method for photonics applications [13]. The technology is suitable for low-cost, mass production of surface-relief microstructures with high lateral resolution (sub-micrometer). Typical applications include the fabrication of diffractive or refractive micro-optical elements on glass or fused silica substrates.

Materials for telecom and datacom application have to fulfill stringent requirements in terms of reliability and long-term stability. In addition, for a cost-effective processing at wafer-scale level, the compatibility with standard lithographic processing equipment is essential.

We have incorporated a UV-replication process based on ORMOCER® materials for the monolithic integration of optical and mechanical micro-structures on VCSEL chips.

This class of materials has been successfully used as lithographically patternable dielectrica for printed circuit boards and multi-chip modules [60], as a waveguide material in integrated optics [9], and for the fabrication of micro-optical elements [61, 7, 59] - among other applications.

4.3.1 Material properties and processing

ORMOCERs® (Organically modified ceramics) are inorganic-organic hybrid polymers and can be classified as Sol-Gel materials. They consist of a Si-O-Si matrix, which is synthesized during a Sol-Gel process by a controlled hydrolysis and condensation of inorganic alcoxysilanes. A co-polymerization with other inorganic metallic alcoxides can be used to influence the mechanical and optical properties of the material [8]. Furthermore, organic (typically acrylate or epoxy based) functional groups are added as the connecting unit for the building of the polymer network. At this stage, the Sol-Gel process is already completed and the material is typically in the state of a viscous liquid solution consisting of nanometer-scale particles (Oligomers).

A variety of ready-to-use ORMOCER® solutions is commercially availably. Before lithographic processing, the material has to be made photosensitive (UV) by adding an amount of a suitable photo-initiator in the order of one weight percent.

The material can be deposited on a glass substrate (or quartz, etc.) or on an optoelectronic wafer by spin-coating. dip-coating or dispensing. The cross-linking is accomplished by exposure with UV-light. For the structur-

ing, the material can be processed similar to a negative resist by mask-exposure for producing binary structures or by a UV-casting method with a UV-transparent mold for the production of three-dimensional relief structures. A combination of the two methods is also possible [59]. Due to the low UV-absorption compared to conventional photoresists (cf. figure 4.9), films of several hundred micron thickness can be exposed.

If a masked exposure is to be carried out, the non-exposed material can be removed with an appropriate solvent. Subsequently to the exposure of the ORMOCER® layer, a thermal annealing at $150°C - 180°C$ assures the chemical stabilization and durability of the composite.

After exposure and annealing, the material becomes an amorphous, non-crystalline and glass-like matter with excellent optical and mechanical properties. It is transparent in the visible wavelength range, as well as in the near-infrared telecom spectral bands at $1.3\,\mu m$ and $1.55\,\mu m$ wavelength. Figure 4.9 shows the measured transmission spectra of two different ORMOCER® type layers deposited on a quartz wafer with a thickness of $250\,\mu m$.

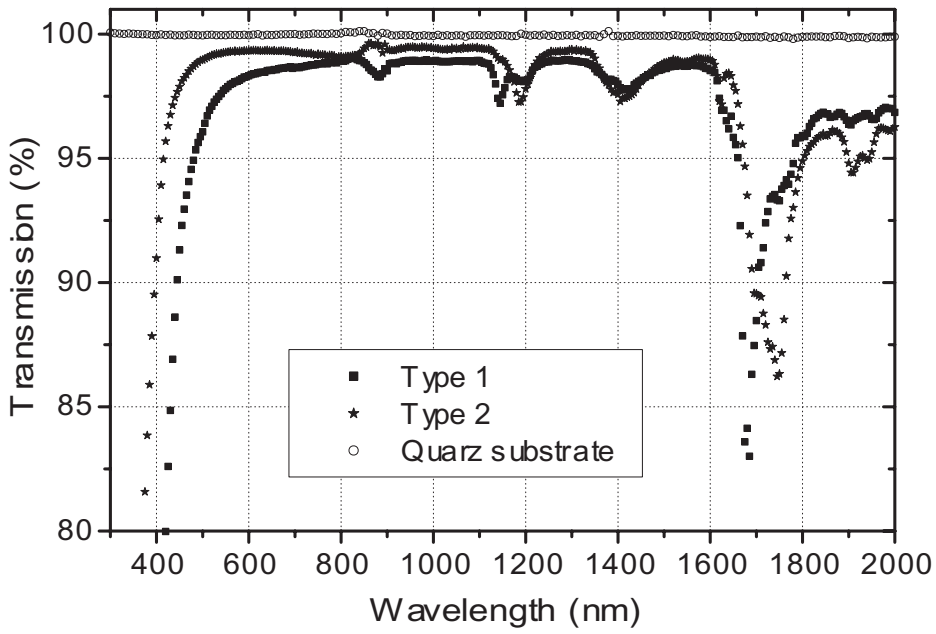

Figure 4.9: Measured spectral transmission of two different ORMOCER types ($250\,\mu m$ thick layers on quartz). The curves are normalized to the transmission of the quartz substrate. Measurements courtesy of Susanne Westenhöfer.

For telecom wavelengths, the optical loss is in the order of 0.2–0.6 dB/cm and in the order of $0.2\,dB/cm$ at a wavelength of $0.85\,\mu m$. The refractive

index for wavelengths in the range of $0.5-0.9\,\mu m$ is in the order of $1.47-1.56$ [62].

Another important advantage of Sol-Gel materials for telecom and datacom applications is its thermal and chemical stability. ORMOCERs® are typically stable up to temperatures of $300°C$, which is important for the compatibility with soldering processes [62]. Furthermore, the stability against moisture is superior to most other polymers for photonics applications (such as PMMA).

Therefore, ORMOCERs® are a suitable material for the monolithic integration with VCSEL chips. We have adapted the process for the chip-level replication of the fiber guiding structures and diffractive lenses (chapter 5).

4.3.2 Application to chip-level replication

The ORMOCER® processing can be applied to a replication of optical and mechanical structures on VCSELs. Figure 4.10 schematically illustrates the UV-casting procedure used therefore.

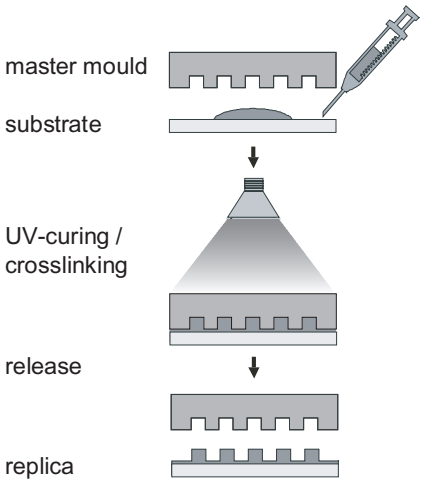

Figure 4.10: Schematic of the sequential process steps of ORMOCER UV-casting.

We have used a UV-transparent PDMS (polydimethylsiloxane) casting mold, copied from the original structure in photoresist. A precise positioning of the replication mold with respect to the the wafer is required and in our case accomplished by a micron-precision cartesian robot. This robot is equipped with an imaging system and distance sensors for sufficient alignment within tolerances better than $\pm 10\,\mu m$ in all three coordinates. Once the mould is positioned with respect to the substrate or wafer, the material

is cross-linked by UV-exposure and the mould can then be lift-off. A subsequent thermal annealing of the devices at $150°C - 180°C$ has been carried out.

In order to extend this technology to full wafer-scale compatibility, the silicone relief-mould can be combined with a lithographic mask for a locally selective cross-linking of the UV-material. In doing so, the problem of sparring out areas for bonding pads and channels for chip dicing can be addressed. Furthermore, additional rods or ridges for the mechanical alignment of other system parts may be implemented in the vicinity of the actual element. If the replication process can be done with a mask-aligner adapted for this purpose, the positioning tolerances can be further improved. A wafer-scale processing is the key for a production at low cost.

4.4 Conclusions

The processing of thick positive photoresist ($d \approx 20\,\mu m$) films with direct laser writing has used for sensing applications in the mid-infrared wavelength range. Based on this first results with deep resist structures, the processing has been adapted to mask-aligner lithography with film thicknesses up to $d = 70\,\mu m$. Combined with thermal reflow techniques, guiding structures for passive fiber alignment have been fabricated and replicated as optical subassemblies directly on VCSEL chips using ORMOCER® materials. The following chapter will describe the use of this process for the integration of diffractive lenses for fiber coupling on multimode VCSEL chips and wafers.

Chapter 5

VCSELs with replicated micro-optics for datacom applications

5.1 Introduction

Within only ten or fifteen years, Vertical Cavity Surface Emitting Lasers (VCSELs) have moved from the laboratory into commercial high performance data communications equipment. Due to numerous advantages over other optoelectronic sources, they have become a preferable choice in a broad range of datacom applications.

First of all, VCSELs can be produced at low-cost, because of their small size and because they are manufacturable with standard microelectronics fabrication methods. The individual devices can be probe-tested already on the chip before packaging. Therefore, the use of VCSELs in optical sub-assemblies can offer a higher yield than for example, edge-emitting lasers. It is also possible, to integrate other devices on the same chip or wafer (e. g. detectors or electronic circuits).

With a typical threshold current between $I = 1$ and $I = 6\,mA$, they provide an efficient power conversion and can deliver transmission rates up to $10\,Gbit/s$. Nowadays, multimode VCSELs are widely implemented in transceivers for high speed, short range fiber links for Fiber Channel and Ethernet transfer protocols [1]. Most of today's local area network (LAN) and storage area network (SAN) routers and switches are already equipped with VCSEL based transmitters and the market for such systems is still growing. Recent market forecasts (November 2000) predict the global market volume for VCSEL based transceivers to grow from 262 million US$ in 1999

to 3.4 billion US$ in 2004 and 14.1 billion US$ in 2009 [2]. The largest increase thereby is predicted for very short range optical fiber links, as future trends indicate a move of the technology to applications such as intra-system links (e. g. optical backplanes), board to board interconnects, chip to chip communication or optoelectronic integrated circuits.

Another important advantage of VCSEL is the inherent capability to build one- and two-dimensional arrays on a single chip, which eases the adaption to fiber-arrays. In addition, the typically low divergent and circular symmetric output beam is well suited for the coupling into fibers.

From the perspective of systems integration, fiber coupling is an issue of particular interest. The established methods for packaging and fiber coupling of optical transceiver subassemblies include the manual or automated active alignment of optical fibers with subsequent encapsulation (pig-tailing), the mounting of lenses or lens arrays (diffractive, refractive or index-gradient) [63] and the use of micro-prisms in combination with horizontally mounted fiber arrays or ribbons and the use of flexible waveguide structures as interconnecting part between lasers and fiber sockets [64, 65]. Some of these approaches are sketched in figure 5.1.

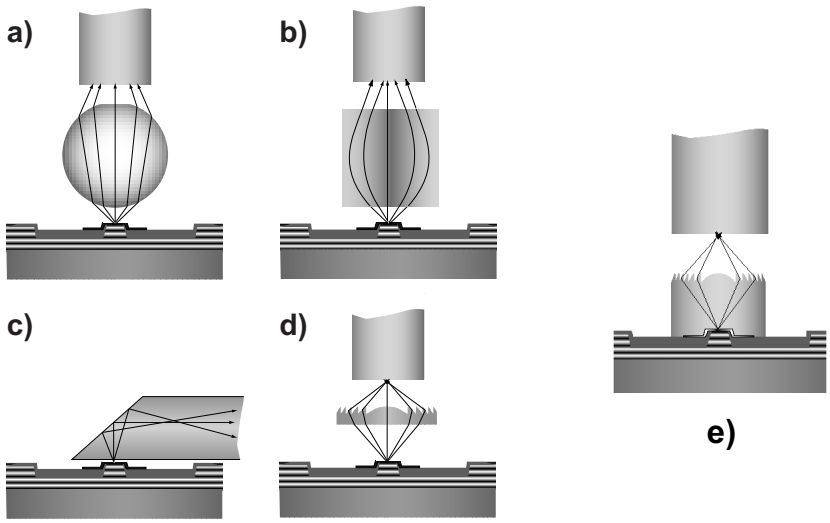

Figure 5.1: Schematic drawing of some commonly used methods for multimode fiber coupling : a) ball lens, b) graded index lens, c) flexible waveguide with coupling prism, d) diffractive lens element. Our approach for monolithic integrated diffractive lenses is shown in drawing e).

However, many of these approaches require time-consuming and costly techniques [66], since only single elements or small arrays can be processed

at a time and an accurate alignment of all components with respect to each other is required. Furthermore, for high data-rate transmissions and small form-factor modules, highly miniaturized elements are required [66].

Based on the experience gained with the on-chip replication of mechanical fiber guides introduced in the previous chapter, we have extended this technology for the monolithic integration of diffractive optical micro-structures on VCSEL chips or wafers (see also publications IV and V).

We demonstrate the technology and design of a system for coupling a multimode VCSEL into a multimode optical fiber using diffractive microlenses. With ORMOCER® as the material of choice, we can profit from the same advantages in terms of fabrication, alignment and compatibility with wafer-scale processing as in the case of the mechanical fiber guides. Although we are only treating the example of replicated diffractive lenses in this chapter, the fabrication principle is not restricted to this case. It is also possible, to adopt it for refractive microlenses or beam shaping elements, for example.

5.2 Characterization of the VCSELs

The devices used for the work presented here, have exclusively been oxide-confined multimode VCSELs with a nominal wavelength of $\lambda = 0.85\,\mu m$, which have been produced by Avalon Photonics. The lasers typically operate up to a maximum output power $p = 2\,mW$ at a current $I = 15\,mA$, above a threshold current $I_{th} \approx 1\,mA$. In figure 5.2 a), the output power is plotted as a function of the current. The typical operation range is between $p = 0.5\,mW$ and $p = 1.5\,mW$ optical output power, which corresponds to a driving current between $I = 3\,mA$ and $I = 9\,mA$.

The spectral properties strongly depend on the driving current. Figure 5.2 b) illustrates output spectra for currents from $I = 1\,mA$ to $I = 12\,mA$. Is is clearly discernible, how the mode distribution is changing with the current. Just above the threshold current I_{th}, the fundamental mode is dominant (the highest peak), but already from $I = 2\,mA$, higher order modes begin to dominate and the number of emitting modes increases. The entire spectrum is shifting by approximately $3\,nm$ towards longer wavelengths, when increasing the current from $I = 1\,mA$ to $I = 12\,mA$. A more detailed insight to the mode characteristics can be gained by taking a look at the near-field intensity distribution at the VCSEL output.

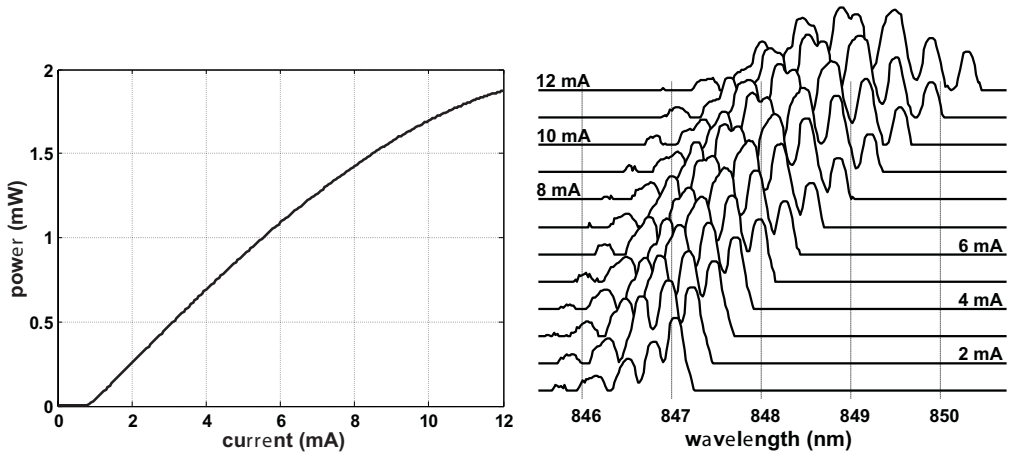

Figure 5.2: a) Multimode VCSEL output power as a function of the current. b) Emission spectra for currents from $I = 1\,mA$ to $I = 12\,mA$ (arbitrary units, logarithmic scale).

5.2.1 Near-field mode characteristics

The optical field emitted by the VCSEL depends on the transverse mode characteristics within the cavity, mainly influenced by the geometry of the resonator structure and by the shape and diameter of the oxide aperture, which is located above the active layer between the two Bragg-mirrors. Figure 5.3 shows a cross-sectional scanning electron microscope image of a VCSEL cavity. The described devices have a circular oxide aperture with a specified diameter $d_{ox} = 11 - 12\,\mu m$.

For measuring the near-field intensity distributions, the emission at the VCSEL output has been imaged onto a CCD camera chip using a high-quality microscope objective. As already indicated by the spectral measurements, the mode characteristics change with the operation current. Figure 5.4 shows the measured near-field intensity distribution for $I = 2, 4, 6$ and $8\,mA$.

It shows, that just above threshold only the fundamental mode of the cavity is present. With increasing current, additional higher order modes appear. In general, the near-field intensity distribution is nearly radially symmetric.

If a linear polarization filter is placed within the characterization setup, it can be qualitatively observed, that the shapes of the individual modes closely resemble the shapes of linear polarized modes (LP-modes) of a circular multimode step index fiber.

It also shows, that typically two orthogonal orientations of LP modes with

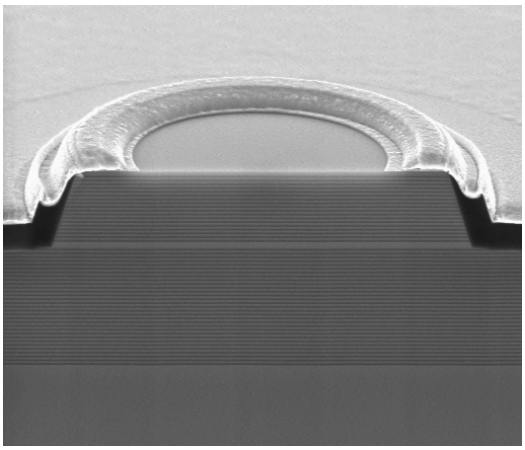

Figure 5.3: Scanning electron microscope cross section image of the VCSEL cavity.

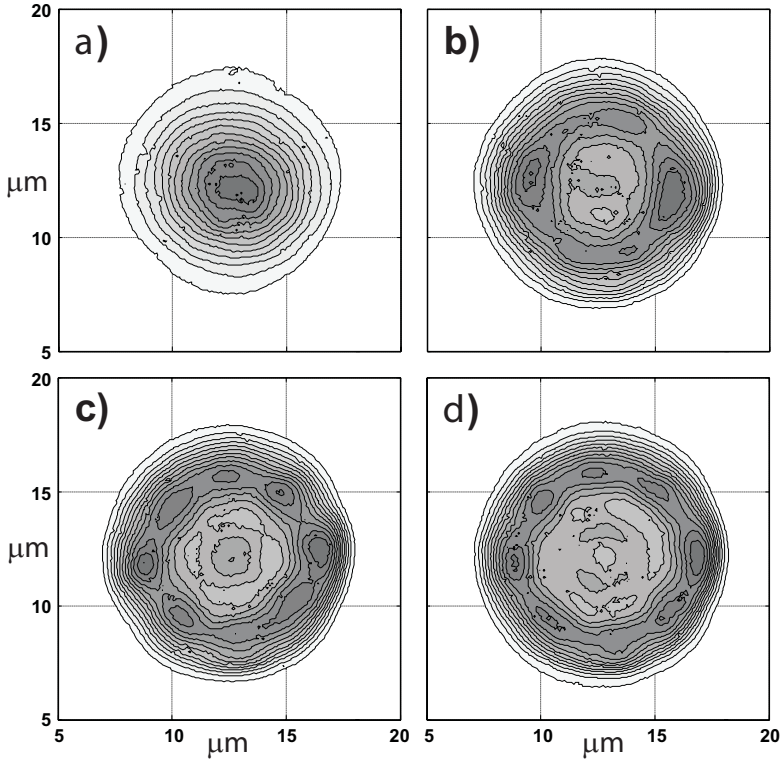

Figure 5.4: Contour plots of measured near-field intensity distributions at the VCSEL output for an operation current of a) $I = 2\,mA$, b) $I = 4\,mA$, c) $I = 6\,mA$ and d) $I = 8\,mA$.

non-zero radial mode index exist with different polarizations and carry approximately the same fraction of power. Both orthogonal mode orientations add up incoherently to a radially symmetric intensity distribution.

However, as the driving current of the VCSEL is increased, the different mode orientations do not appear exactly at the same point. The overall polarization state is therefore not constant throughout the operation range and exhibits a complex behavior [67, 68].

It has been shown, that the measured near-field intensity distributions can in fact be well approximated by LP-modes of a step index fiber model [69]. For the used devices, a corresponding core diameter of $11\mu m$ and an index difference between core and cladding $\Delta n = 0.01$ of the model fiber showed the best fit. These values are in good agreement with the specification for the oxide aperture diameter and the expected values for the refractive indices [69]. The mathematical treatment of the LP-mode model will be discussed in more detail in section 5.3.

Another important indicator for the characteristics of the emitting modes is the intensity distribution in the far-field.

5.2.2 Far-field characterization

The VCSEL emission has been measured in the far-field by use of a goniometric scanning stage. A photodetector with a pin-hole aperture has been used to determine the angular intensity distribution at a distance of $200\,mm$. Again, the measurements have been repeated for different operation currents.

The results for the angular intensity scans are shown in figure 5.5 for currents from $1\,mA$ to $12\,mA$. It is clearly discernible, that the circular symmetry in the intensity distribution is also present in the far-field.

At $I = 1 - 2\,mA$, only the fundamental mode (LP_{01}) occurs and already at $I = 3\,mA$, also the LP_{11} mode is present in the intensity distribution. For higher currents, the number and distribution of the contributing modes can only be determined qualitatively and only in combination with the near-field measurements.

Figure 5.5 also illustrates, how the beam divergence depends on the mode distribution and thus, on the operation current. It is readily seen, that the divergence strongly increases with the current and that the intensity maximum is moving away from the center. For currents above $\approx 3\,mA$, the predominant appearance of the far-field intensity distribution corresponds to a ring-shape.

As a quantitative measure for the divergence, the emission angle, which corresponds to circular radiation cone containing a fraction of 86.5 % of the

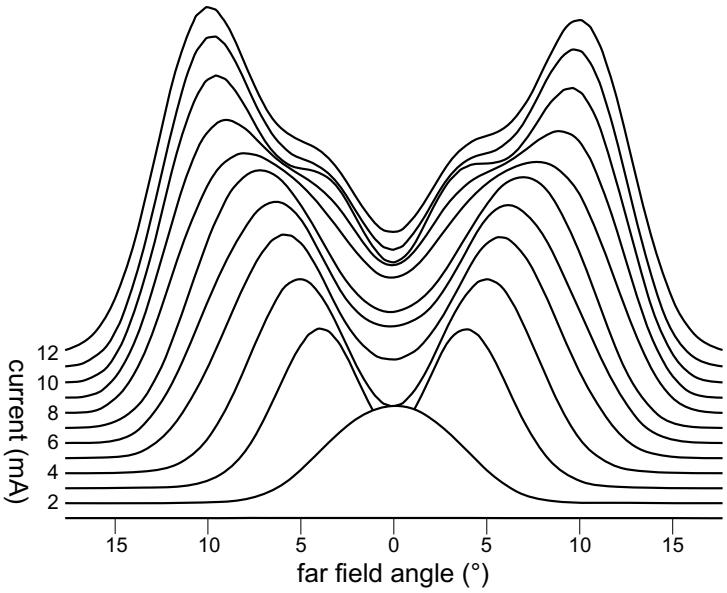

Figure 5.5: Measured angular far-field intensity distribution (arbitrary units) in free space for operation currents from $1\,mA$ to $12\,mA$ (one dimensional scan).

total power has been calculated by radiometric integration. These values are listed in Table 5.1.

The table also gives the analogue divergence angles for a propagation of the beam within a homogeneous material with a refractive index $n = 1.54$. This number corresponds to the refractive index of the Sol-Gel material (ORMOCER®), chosen for the replicated lenses at the VCSEL wavelength ($\lambda \approx 0.85\,\mu m$).

With the measurement data obtained from the near- and far-field observations, a mathematical description for the field at the VCSEL output has been developed for the simulation of the coupling system.

Qualitative measurements based on the observations of the far-field, as well as the near-field intensity patterns confirm that the modes with the highest significance are LP_{01}, LP_{11}, LP_{21}, LP_{31}, LP_{41} and LP_{12}. With increasing current, more and more energy moves into higher order modes. At $p = 1\,mW$ ($I = 6 - 8\,mA$), approximately 50 % of the optical power is carried by the modes LP_{31} and LP_{41} and less than 10 % by the fundamental mode.

Table 5.1: Far-field divergence angles θ in degree and the corresponding numerical aperture for propagation in air ($n = 1.00$) and ORMOCER ($n = 1.54$). The values correspond to the angle of a radiation cone which contains 86.5% of the total emitted power.

	$n = 1.00$		$n = 1.54$	
I (mA)	θ	NA	θ	NA
2	6.64°	0.12	4.31°	0.08
3	7.88°	0.14	5.12°	0.09
4	9.16°	0.16	5.95°	0.10
6	11.1°	0.19	7.21°	0.13
8	12.2°	0.21	7.92°	0.14
10	12.7°	0.22	8.25°	0.14
12	13.3°	0.23	8.60°	0.15

5.3 Modelling of the VCSEL modes

In order to simulate the coupling performance of the entire system (for different geometrical arrangements), an adequate mathematical description for the VCSEL source beam is required. The modelling of the mode characteristics of the VCSEL is mandatory for a sufficient analysis of the beam propagation properties, the lens performance and estimation of the fiber coupling efficiency.

It has been demonstrated in reference [69], that the transverse modes field at the output of an oxide-confined VCSEL can be adequately modelled by linear polarized modes (LP-modes) of a weakly guiding step-index fiber. The following reasons justify this approximation:

The resonator of the described VCSELs is built up of two stacks of reflection layers (Bragg-mirrors) with an active region consisting of typically three quantum-well layers in between. An electrical, as well as an optical confinement is accomplished by an etched mesa structures (cf. figure 5.3) and the oxide-confinement layer, which has an circular aperture and is located immediately above the active layers.

Within the Al-oxide confinement layer (around the aperture), the refractive index is significantly lower than inside the aperture (semiconductor material). Therefore, a mode is laterally confined (guided) as it propagates though the aperture layer and diffracts after passage. Due to the short effective cavity length of a few micron and the periodic back and forth reflection between the mirrors, this lateral confinement is similar to a focusing.

In this manner, the VCSEL cavity acts like a periodic waveguide and the

periodically guided modes can be approximated by the modes of a circular symmetric step index fiber. The refractive indices for the core and cladding of this model can be estimated by calculating the mean refractive indices for a vertical round-trip propagation through the region inside the oxide aperture area and outside oxide aperture area, respectively [69]. The radius of the oxide aperture corresponds to the radius of the waveguide core.

5.3.1 Circular step index fiber mode model

We consider a circular symmetric step index fiber in cylindrical coordinates as a mathematical representation of the VCSEL. The radial solution of the wave equation for guided waves in the core and cladding region can be written as [70, 71, 72]:

$$u_{lm}(\rho) \propto \begin{cases} J_l(k_t\rho), & \rho \leq a \\ J_l(k_t a)/K_l(\gamma a)K_l(\gamma\rho), & \rho > a, \end{cases} \tag{5.1}$$

where J_l is the l-th order Bessel function of the first kind, K_l is the modified Bessel function of the second kind and order l. The radius of the fiber core is denoted by a. The parameters k_t and γ are given by

$$k_t^2 = n_1^2 k_0^2 - \beta^2, \quad \gamma^2 = \beta^2 - n_2^2 k_0^2, \quad k_0 = 2\pi/\lambda_0. \tag{5.2}$$

λ_0 is the vacuum wavelength, n_1 and n_2 are the refractive indices of the core and the cladding, respectively and β is the propagation constant of the mode. A mode will be guided, if k_t and γ satisfy the characteristic equation

$$k_t \frac{J_{l\pm1}(k_t a)}{J_l(k_t a)} = \pm\gamma \frac{K_{l\pm1}(\gamma a)}{K_l(\gamma a)}. \tag{5.3}$$

In case of a weakly guiding fiber, the guided waves can be approximated as transverse electromagnetic waves (TEM). Thus, the general solution for weakly guided waves can be described by a set of linearly polarized (LP_{lm}) modes [70, 71]:

$$\begin{aligned} u_{lm}^s(\rho,\phi,0) &= A u_{lm}(\rho)\cos(l\phi) \\ u_{lm}^p(\rho,\phi,0) &= A u_{lm}(\rho)\sin(l\phi), \end{aligned} \tag{5.4}$$

where A denotes the mode amplitude, ϕ the azimuthal angle and the superscripts s and p account for the two orthogonal orientations of the mode (l, m).

For the modelling of the real VCSEL device, a core radius $a = 5.5\,\mu m$ and a refractive index difference $\Delta n = 0.01$ has yielded the best agreement

with the measurements of the near- and far-field intensity distributions (see sections 5.2.1 and 5.2.2). However, the far-field divergence of the modelled beam is slightly lower (5%-10%) as the divergence of the measured beam. One possible reason therefore is that the curvature of the wave field emerging from the VCSEL is not known, since its phase can not be retrieved by measuring the near-field intensity.

The calculated values of k_t and γ for the model described above are quoted in tables 5.2 and 5.3

Table 5.2: Calculated values of k_t for $a=5.5\,\mu m$, $\Delta n=0.01$, $\lambda=0.85\,\mu m$

m	$l=0$	$l=1$	$l=2$	$l=3$	$l=4$
1	0.399	0.635	0.850	1.054	1.252
2	0.912	1.157	1.383	1.597	1.799

Table 5.3: Calculated values of γ for $a=5.5\,\mu m$, $\Delta n=0.01$, $\lambda=0.85\,\mu m$

m	$l=0$	$l=1$	$l=2$	$l=3$	$l=4$
1	1.855	1.788	1.697	1.578	1.426
2	1.664	1.504	1.299	1.025	0.602

The analytical evaluation of the far-field properties of an LP-mode has been done by calculating the Fraunhofer diffraction integral [26], assuming a phase of the source field, which has no curvature.

5.3.2 Fraunhofer diffraction of LP-modes

In order to gain more insight in the propagation properties of individual step-index fiber LP-mode, the (scalar) diffracted field of the mode has to be calculated. For simplicity ,we take one angular mode orientation (cosine) as an example: $u_{lm}(\rho,\phi,0)=u^s_{lm}(\rho,\phi,0)$.

If the distance of the image plane z from the VCSEL plane is sufficiently large ($z\gg ka^2/2$), the Fraunhofer approximation can be used for the evaluation of the far-field intensity distribution of an individual mode:

$$u_{lm}(r,\vartheta,z)=\frac{\exp(ikz)}{i\lambda z}\exp\left(\frac{ikr}{2z}\right)U_{lm}\left(\frac{r}{\lambda z},\vartheta,0\right). \tag{5.5}$$

Here, r and ϑ are the radial and angular corrdinate in the image plane and $U_{lm}(\zeta, \vartheta, 0)$ denotes the two-dimensional Fourier transform ($\mathcal{FF}$) of the mode field at the VCSEL output ($z=0$):

$$U_{lm}(\zeta, \vartheta, 0) = \mathcal{FF}\{u_{lm}(\rho, \phi, 0)\} = G_{lm}(\zeta)\cos(l\vartheta). \tag{5.6}$$

$U_{lm}(\zeta, \vartheta, 0)$ can be separated into a radial function $G_{lm}(\zeta)$ and the factor $\cos(l\vartheta)$. Therefore, it is readily seen, that the diffracted mode in the far-field keeps its azimuthal angle-dependence. The radial function derives to [71, 73]:

$$\begin{aligned} G_{lm}(\zeta) &= 2\pi A a i^l \left\{ \frac{\bar{\zeta} J_{l-1}(\bar{\zeta}a) J_l(k_t a) - k_t J_{l-1}(k_t a) J_l(\bar{\zeta}a)}{k_t^2 - \bar{\zeta}^2} \right. \\ &\quad \left. - C \frac{\bar{\zeta} J_{l+1}(\bar{\zeta}a) K_l(\gamma a) - \gamma K_{l+1}(\gamma a) J_l(\bar{\zeta}a)}{\gamma^2 + \bar{\zeta}^2} \right\}, \\ &\quad with \quad \bar{\zeta} = 2\pi\zeta; \quad C = J_l(k_t a)/K_l(\gamma a). \end{aligned} \tag{5.7}$$

Consequently, the intensity in the image plane is given by

$$I(r, \vartheta, z) = |u_{lm}(r, \vartheta, z)|^2 = \frac{\cos^2(l\vartheta)}{(\lambda z)^2} \left| G_{lm}\left(\frac{r}{\lambda z}\right) \right|^2. \tag{5.8}$$

The radial shape of the intensity distribution of a mode (l, m) in the far-field depends on the parameters k_t and γ. For the chosen model (as described in the previous section), the shape of the modes with an radial index $m=1$ is nearly propagation-invariant. On the other hand, modes with $m > 1$ have a different radial shape of the intensity distribution in the far-field. In this case, the intensity maxima typically move from the central lobes to the outer lobes with propagation (the mode has m radial lobes). Figure 5.6 illustrates the intensity distribution of the modes LP_{01}, LP_{11}, LP_{21}, LP_{31}, LP_{02} and LP_{12} in the near- and far-field.

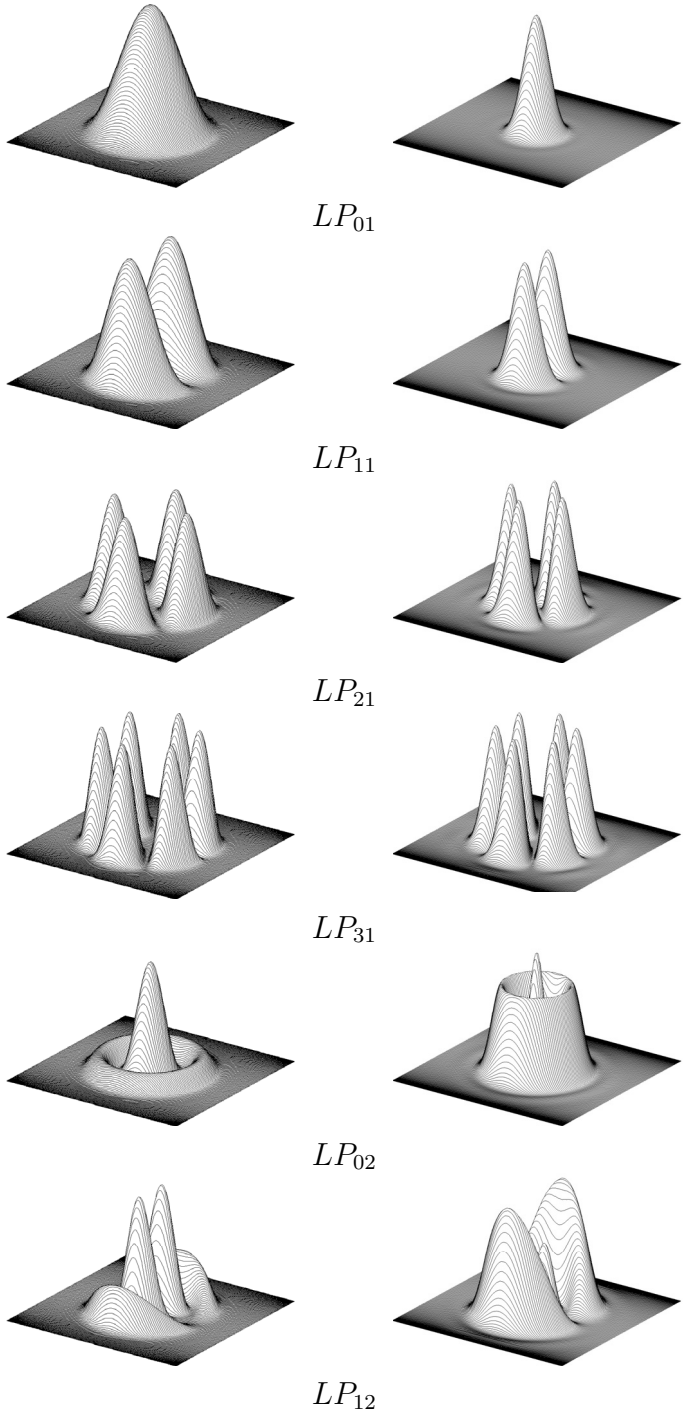

Figure 5.6: Illustration of the shape of some exemplary LP-modes (intensity) of the described fiber model in the near field (left) and the corresponding far-field shape (right).

5.4 Simulation of the coupling system

Based on the mathematical model for the mode characteristics of the VCSEL introduced in section 5.3.1, the simulation of the entire coupling system can be accomplished. The aim of the simulation is to evaluate the influence of the geometrical dimensions and the performance of the diffractive lens on the coupling behavior of the individual modes. The geometrical setup of a VCSEL chip with a monolithic integrated diffractive lens (replicated in ORMOCER® material by UV-casting) is sketched in figure 5.7.

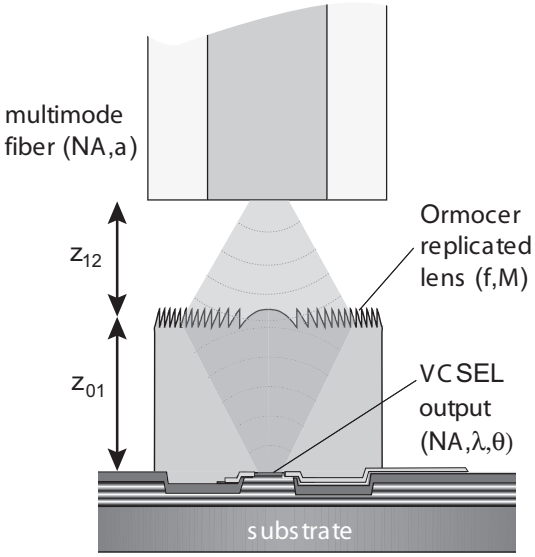

Figure 5.7: Schematic cross-section of a VCSEL chip with a monolithic integrated (replicated) diffractive lens in Sol-Gel (ORMOCER) material.

For arrays of VCSELs (and fibers), the maximum diameter of the lens is limited by the array pitch (typically $250\,\mu m$). On the other hand, for a compatibility with wafer-scale processing, the lens diameter may also be constrained by the layout of the VCSEL wafer (bonding pads, dicing channels, etc.). In addition, the divergence or numerical aperture (NA) of the source beam and the $NA$of the fiber have to be taken into account. Furthermore, application-specific geometrical limitations might be imposed.

We seek for an optimized solution for the geometrical setup within these constraints. Therefore, the propagation of the source modes through the replicated structure, the transmission through the lens and the coupling into the multimode fiber have to be simulated.

For a phenomenological study of the optimization problem, the simulation has been split into the following design aspects:

1. calculating the coupling efficiencies of individual modes for different geometrical arrangements and fiber positioning errors, assuming an ideal diffractive lens,

2. calculating the coupling efficiencies of individual modes for different diffraction orders of a non-ideal lens.

3. simulating the diffraction efficiency of a diffractive lens fabricated by direct laser writing.

Points 1 and 2 are treated in section 5.4.3, respectively and point 3 in section 5.4.2. For the simulation, a suitable method for the propagation of the mode through the system and for the coupling into the fiber is required.

5.4.1 Mode propagation and coupling efficiency estimation

According to the notations given in figure 5.7, the steps required for the simulation can be outlined as follows:

- propagate the mode field from the VCSEL plane to the lens plane (distance z_{01}), within medium 1 (the replication material),

- apply the transfer function of the diffractive lens,

- propagate the field emerging from the lens over distance z_{12} within medium 2 (air),

- calculate the coupling efficiency.

For the calculation of the field in the lens plane, the Fraunhofer diffraction formula given by equation 5.5 can be used, since the distance between the lens and the VCSEL is typically large, compared with the VCSEL aperture. However, we have chosen an alternative (Fourier-optical) approach for this simulation, which is more versatile for the given problem.

We use the first Rayleigh-Sommerfeld diffraction integral in form of a convolution for the propagation of a scalar field within a homogeneous medium with a refractive index n and a wavenumber $k = nk_0$ [26, 74, 27]:

$$u(x, y, z_b) = \mathcal{F}^{-1}\left\{\mathcal{F}\left[u(x, y, z_a)\right] H(\xi_x, \xi_y)\right\}, \tag{5.9}$$

$$H(\xi_x, \xi_y) = \begin{cases} exp\left[ikz_{ab}(1-\Omega)^{1/2}\right], & \Omega < 1, \\ 0, & otherwise, \end{cases} \tag{5.10}$$

$$\Omega = \lambda^2(\xi_x^2 + \xi_y^2). \tag{5.11}$$

$\mathcal{F}$ and $\mathcal{F}^{-1}$ denote the forward and inverse Fourier-transform, respectively. Consequently, $\mathcal{F}[u(x, y, z_a)]$ represents the plane-wave spectrum of the field $u(x, y, z_a)$ in the transverse plane at $z = z_a$ with spatial frequencies ξ_x and ξ_y [26].

$H(\xi_x, \xi_y)$ is the transfer function in Fourier space for the propagation over a distance $z_{ab} = z_b - z_a$ in a homogeneous medium. The condition $\Omega < 1$ in equation 5.10 assures, that evanescent waves are neglected.

In this manner, the fields are propagated from the source to lens plane and from the lens to the fiber plane, respectively. For a fast and efficient numerical implementation of this procedure, fast-Fourier-transform (FFT) and inverse fast-Fourier-transform (IFFT) algorithms are employed. In order to avoid numerical artifacts due to aliasing effects, a minimum lateral field sampling resolution of $\lambda/2$ is required. In case that the resulting resolution of the plane-wave spectrum is insufficient, the number of original field sampling points needs to be increased by zero-padding [75] (the sampling of the FFT-spectrum ranges from $-f_{Ny}$ to $+f_{Ny}$, specific to the algorithm).

The transfer function of the diffractive lens is applied in real space (object space) using the thin element approximation. The mathematical description of the used transfer function is given in section 3.3.2, by equations 3.16 - 3.18.

For the estimation of the coupling efficiency of the mode into a multimode fiber with a core radius r_c and a numerical aperture NA_f, we make the following assumptions:

First, the light must be incident within the core area. Therefore, the fraction of optical power encircled within the fiber core area and normalized by the totally emitted power is denoted by a factor η_{core}, corresponding to the "spatial" coupling efficiency.

Second, the incident beam must not exceed the numerical aperture of the fiber. From a ray-optical point of view, this means that rays whose angle with the fiber axis θ_f exceeds the value $\arcsin(NA_f)$, do not fulfill the condition for total internal reflection. This limitation can be expressed as a cut-off condition in Fourier space. It is equivalent to a spatial filtering of the plane-wave spectrum. It derives to:

$$\Omega < NA_f^2. \tag{5.12}$$

Consequently, we introduce a second factor η_{NA}, which is determined by the encircled power in Fourier space according to the above condition and normalized to the total power (this is justified by the Parseval-theorem [26]). The estimated total coupling efficiency derives then to $\eta = \eta_{core}\eta_{NA}$.

The entire procedure for the propagation and coupling efficiency calculation is carried out for each individual mode (and mode-orientation). Due to the orthogonality of the LP-modes, the total field intensity in the image plane can be obtained by an incoherent superposition of the propagated modes.

In the following section, the influence of the distances between VCSEL, lens and fiber on the fiber coupling efficiency of individual modes is investigated, as well as the effect of a displacement of the fiber.

5.4.2 Geometrical system design aspects

One goal for the direct integration of diffractive lenses on the VCSEL chip is to achieve tolerances for the positioning of the fiber, which can be met by passive alignment. For this reason, it is necessary to simulate the effect of a fiber displacement and to find a geometric configuration, which provides sufficient tolerances.

Effects related to an angular or axial displacement of the diffractive lens itself are not investigated, since we assume that the fabrication of the element on a wafer-scale level is sufficiently accurate (in the order of a few micron - read also section 3.2 in publication V).

First, we assume an infinitely thin diffractive lens with a diffraction efficiency $\eta = 1.0$. Based on the LP-mode model and the propagation procedure described in sections 5.3 and 5.4.1, respectively, the coupling behavior of individual modes is investigated.

The actual purpose of the lens can be regarded as an imaging of the VCSEL-output onto the facet of the fiber. Therefore, the magnification of the image should be optimized to achieve high coupling efficiencies. We consider a cleaved standard step-index multimode fiber with a core diameter $d_f = 50\,\mu m$ and a numerical aperture $NA_f = 0.20$.

In the paraxial approximation (from ray-optical considerations), the magnification factor m is given by

$$m \approx \frac{n_1}{n_2}\frac{z_{12}}{z_{01}}. \tag{5.13}$$

Hereby, n_1 and n_2 denote the refractive indices of the medium in front of the lens (replication material) and behind the lens (air), respectively.

A magnification $m < 1$ can lead to an partial excess of NA_f, since the $NA$of the VCSEL at high operation currents ($I = 10 - 12\,mA$) is already in the order of $0.14 - 0.15$ ($NA$of the 86.5 % power equivalent cone angle within the replication material, cf. table 5.1).

For given geometrical distances z_{01} and z_{12}, the focal length of the diffractive lens is chosen as

$$f = \left[\frac{n_1}{n_2 z_{01}} + \frac{1}{z_{12}}\right]^{-1}, \tag{5.14}$$

which corresponds to the ray-optical paraxial approximation.

We have simulated the coupling efficiencies as a function of the lateral displacement of the fiber from the center for the modes LP_{01}, LP_{11}, LP_{31} and LP_{41}, as an example. In figure 5.8, the results are plotted for three different geometrical configurations, corresponding to magnification factors $m \approx 0.75, 1.5$ and 3.0 (given by the distances z_{01} and z_{12}, according to equation 5.13). In all three cases, $z_{01} = 200\,\mu m$ has been chosen.

The first plot, figure 5.8a), shows the calculated tolerance curves for $z_{12} = 400\,\mu m$ or a magnification $m \approx 3$. It is readily seen, that the coupling efficiency reaches 1.0 within lateral displacement tolerances in the order of $10\,\mu m$. The tolerances depend to a low degree on the mode number. The lateral tolerance for the maximum coupling efficiency is significantly smaller than the fiber core radius, due to the large magnification. In this case, the diameter of the image spot is in the order of 50 % to 60 % of the fiber core diameter, depending on the mode order.

A case with a low magnification of $m \approx 0.75$ is shown in figure 5.8b). Here, the lateral displacement tolerances for maximum coupling efficiency are approaching the dimensions of the fiber core ($50\,\mu m$ diameter). However, the maximum coupling efficiency depends strongly on the mode number and is significantly below 1.0 for the higher order modes. The reason therefore is, that they already partially exceed the numerical aperture of the fiber. Since the angular intensity distribution of the higher order modes typically has a ring-shape (see section 5.2.2), a considerable fraction of optical intensity within the lens plane can lie outside the acceptance cone of the fiber.

Finally, in figure 5.8c) a configuration with distances $z_{01} = z_{12} = 200\,\mu m$ or a magnification of $m \approx 1.5$ is considered. It can be regarded as a compromise between the first two cases. The *NA*of the beam emerging from the lens is smaller than the *NA*of the source beam, while the imaged spot is still significantly smaller than the fiber core. As a consequence, the tolerance curves are nearly identical for the indicated modes and the coupling efficiency reaches $\eta \approx 1.0$ within a lateral displacement range larger than $\pm 15\,\mu m$.

The latter example represents almost an ideal case for the coupling conditions: All modes are coupled into the fiber with efficiencies reaching 1.0 within fiber displacement tolerances primarily determined by the radius of the fiber core. This is a good starting point for an optimized design.

In the following two sections, some of the effects on the coupling behavior

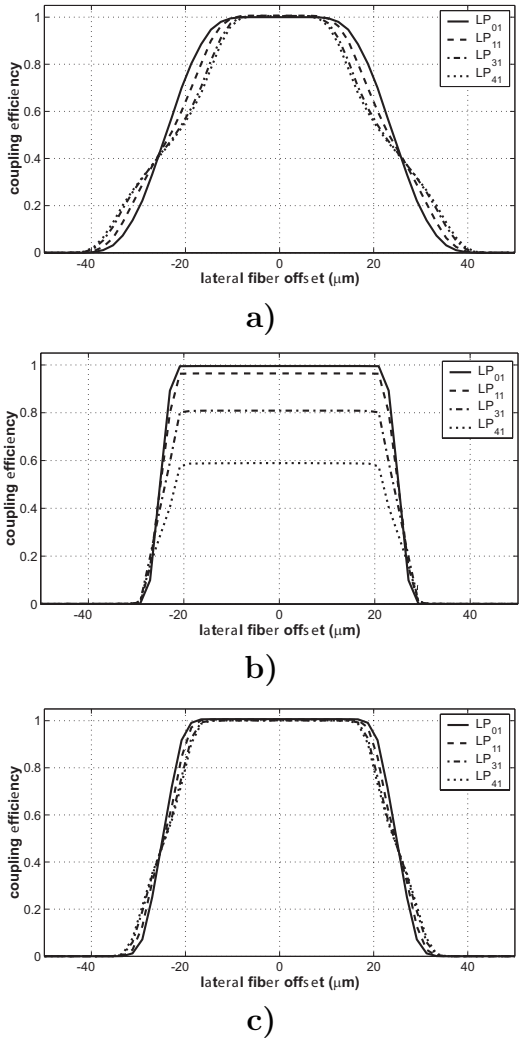

Figure 5.8: Simulated coupling efficiencies for the modes LP_{01}, LP_{11}, LP_{31} and LP_{41}, as a function of the lateral displacement of the fiber. The three plots correspond to different geometrical setups: a) $z_{12} = 400\,\mu m$, b) $z_{12} = 100\,\mu m$ and c) $z_{12} = 200\,\mu m$. In all three cases, $z_{01} = 200\,\mu m$.

of individual modes caused by the diffraction efficiency of the diffractive lens are described.

5.4.3 Estimation of the diffractive lens efficiency

So far, an ideal diffractive lens with a diffraction efficiency of $\eta_l = 1.0$ has been assumed. However, the efficiency of a real fabricated diffractive lens for the focusing of a beam with such a high numerical aperture is significantly

lower.

The fiber coupling efficiency of the system is not only determined by the imaging properties, but also by the performance of the diffractive lens. The elements used for this work have been fabricated by direct laser writing (see section 2.1).

Due to the high $NA$of the diffractive lens (typically in the order of $0.15-0.25$), significant losses in the diffraction efficiency have to be taken into account. The fabrication of such elements requires zone sizes in the order of a few micron at the outer regions of the lens. The limited resolution of the fabrication process can be modelled by help of the convolution method introduced in Section 2.2.

In doing so, an estimation for the local diffraction efficiency as a function of the lens radius can be given. Taking also the measured far-field data into account, the intensity distribution in the lens plane can be determined. Thus, the overall diffraction efficiency of the lens can be calculated by zone-wise integration of the power diffracted into the design order.

Figure 5.9 summarizes the according results for the integrated diffraction efficiency as function of the distance between the VCSEL and the lens for the examples of $z_{12}=200\,\mu m$ and $z_{12}=400\,\mu m$.

In these figures, three different design diffraction orders $M = 1$, $M = 2$ and $M = 4$ have been considered. The integrated diffraction efficiencies for these orders are plotted for an irradiance distribution in the lens plane which correspond to an VCSEL operation current of $5\,mA$ and $10\,mA$, respectively.

Due to the ring-like intensity distribution in the lens plane for higher operation currents, the efficiency decreases with increasing design distance z_{01}, even though the numerical aperture of the lens relaxes (f gets larger). The same effect holds for an increasing operation current, since then the beam divergence increases. The efficiency drops approximately by a factor of $0.05-0.1$ if the current is changed from $I=5\,mA$ to $I=10\,mA$.

The most significant influence on the diffraction efficiency is imposed by the chosen design order M. As indicated in figure 5.9, the integrated diffraction efficiencies for $M = 2, 3, 4$ are drastically higher than for $M = 1$. With higher design orders, the number of diffractive zones reduce by a factor of M, compared to $M = 1$ and thus, the zones become larger. As a consequence, the convolution effect becomes less significant and the efficiency increases. However, not only the zone sizes, but also the relief depth increases. For lenses designed for $M > 3$, the smoothing effect becomes more dominant, due to an increasing convolution spot. Thus, the optimum value for M is typically in the range of $3-4$.

The maximum fiber coupling efficiency of the beam diffracted into the design order is naturally determined by the diffraction efficiency of the lens.

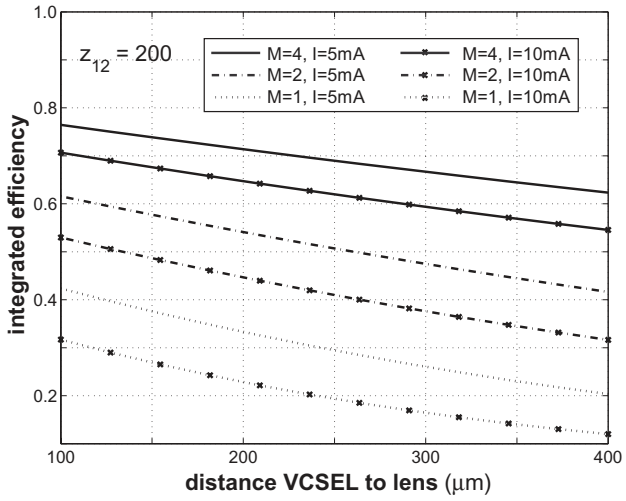

a)

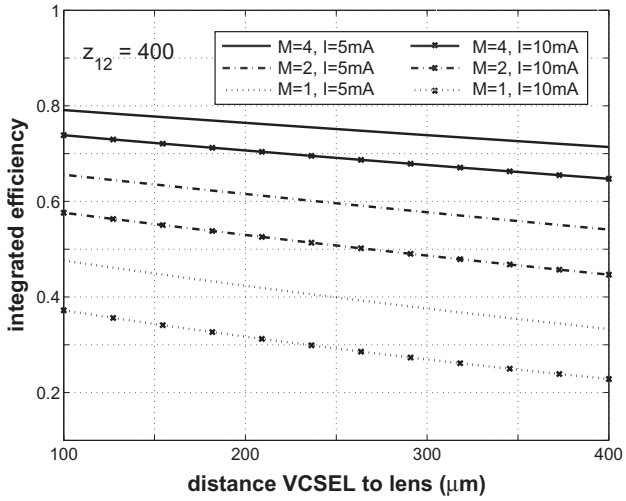

b)

Figure 5.9: Integrated (total) efficiencies of diffractive lenses as a function of the distance between the VCSEL and the lens for a) $z_{12} = 200\,\mu m$ and b) $z_{12} = 400\,\mu m$, calculated for a convolution of the lens profile with a Gaussian writing beam with a diameter of $1.5\,\mu m$ FWHM. The lines correspond to design diffraction orders $M = 1, 2$ and 4 for laser operation at $I = 5\,mA$ (unmarked lines) and $I = 10\,mA$ (marked lines).

For an estimation of the real fiber coupling efficiency, the results derived in section 5.4.2 have to be multiplied by this factor.

The light, which is not diffracted into the design order is distributed among other diffraction orders. An important question arises, which is rele-

vant for the overall performance of the coupling system: Whether the light contained in this "stray-light" orders will contribute to the overall loss or will (at least partially) still be guided by the fiber? This important issue will be discussed in the following section.

5.4.4 Coupling of stray light diffraction orders into the fiber

In section 5.4.2, the fiber coupling coefficients of individual LP-modes have been calculated only under the assumption of a perfect diffractive lens. An important issue for the evaluation of the overall performance of the system is the coupling of individual modes into the fiber, which are not only diffracted into the design diffraction order, but also into "stray-light" orders.

As described in section 3.3.2, the diffraction orders of a diffractive lens focus at different axial distances, according to equation 3.22.

In this manner, the coupling efficiencies associated with an individual diffraction order can be determined by treating it as a separate "lens" with the same procedure as used in section 5.4.2. Therefore, a quantitative measure for the amount of stray light, which is launched into the fiber can be given. A detailed treatment of the fraction of light in "stray-light" orders, which is not coupled into the fiber can not be accomplished by the described methods and will therefore not be further discussed. It will be partially reflected from the fiber facet and partially radiate away through the fiber cladding.

The Tables 5.4 and 5.5 list the calculated coupling efficiencies of some of the most important VCSEL modes diffracted into different orders m. Two different lens designs are considered. The first one with $M=4$, $z_{01}=200\,\mu m$, $z_{12}=400\,\mu m$ and the second with $M=4$, $z_{01}=400\,\mu m$, $z_{12}=400\,\mu m$. The two designs have also been realized experimentally (see section 5.5).

Both tables show, that the coupling coefficients strongly depend on the mode number. The fundamental mode is coupled into the fiber almost with an efficiency $\eta = 1.0$ for $m = 2, ..., 6$, whereas for higher modes, only the neighboring orders $m=3$ and $m=5$ contribute to a significant coupling. The main reason therefore is, that the spot size in the fiber plane is larger for $m \neq M$ and the numerical aperture can be exceeded (especially for $m < M$). The density of focal points on the optical axis increases with M and decreases with the chosen distance between the lens and the fiber. Thus the lens with $z_{12}=400\,\mu m$ (table 5.5), exhibits less tolerant efficiency values, compared to the lens with $z_{12}=200\,\mu m$ (table 5.4).

Another important result of the calculations is the effect of an axial dis-

Table 5.4: Calculated coupling efficiencies of the modes LP_{01}, LP_{11}, LP_{31} and LP_{41} for different diffraction orders m of a fourth order lens. The geometrical distances are: $z_{01} = 200\,\mu m$ and $z_{12} = 400\,\mu m$. Values are given for axial fiber displacements $\Delta z = -100$, 0 and $+100\,\mu m$.

m	$\Delta z\,(\mu m)$	LP_{01}	LP_{11}	LP_{31}	LP_{41}
	-100	0.99	0.87	0.21	0.06
2	0	0.97	0.73	0.10	0.02
	$+100$	0.92	0.58	0.05	0.01
	-100	1.00	0.99	0.92	0.74
3	0	0.99	0.98	0.87	0.67
	$+100$	0.99	0.95	0.77	0.57
	-100	1.00	1.00	1.00	1.00
4	0	1.00	1.00	1.00	1.00
	$+100$	1.00	1.00	0.99	0.98
	-100	1.00	1.00	1.00	1.00
5	0	0.96	0.90	0.71	0.60
	$+100$	0.86	0.67	0.28	0.14
	-100	0.96	0.88	0.60	0.43
6	0	0.82	0.56	0.08	0.02
	$+100$	0.66	0.28	0.01	0.01

Table 5.5: Calculated coupling efficiencies of the modes LP_{01}, LP_{11}, LP_{31} and LP_{41} for several diffraction orders m of a fourth order lens. $z_{01} = 400\,\mu m$ and $z_{12} = 400\,\mu m$.

m	LP_{01}	LP_{11}	LP_{31}	LP_{41}
2	0.89	0.48	0.03	0.01
3	0.99	0.98	0.64	0.33
4	1.00	1.00	1.00	1.00
5	0.99	0.96	0.85	0.76
6	0.86	0.48	0.02	0.00

placement of the fiber with respect to the design focal position. Table 5.4 additionally list the results for the coupling efficiency of the modes for axial fiber displacements $\Delta z = \pm 100\,\mu m$.

Such a longitudinal shift of the fiber has interesting consequences: A displacement within this range has only a minor effect on the coupling of

the diffraction order. On the other hand, the coupling efficiencies for light in other orders can be significantly improved if the fiber is placed closer to the lens ($\Delta z < 0$). In particular, light in the orders $M \pm 1$ can be collected more efficiently. This orders typically contain the major fraction of "stray-light", if we consider diffractive lenses with a convolved profile.

The optimal value for Δz generally depends on the chosen design order, the geometrical distances and the diffraction characteristics of the lens. If the fiber is placed too close to the lens, the efficiencies can decrease. The same holds in general for displacements $\Delta z > 0$.

Not only the maximum coupling efficiency and misalignment tolerances are influenced by the coupling behavior of individual modes. It can also affect the transmission properties of the coupling system at high frequencies (e. g. for transmissions in the GHz-range). In particular, a differential coupling of the modes can cause mode partitioning within the VCSEL cavity. This in turn can give rise to modal noise with a detrimental effect on the transmission bandwidth [76].

5.5 Experimental Results

Starting from the theoretical design considerations, first experimental samples of VCSELs with on-chip integrated diffractive lenses for multimode fiber coupling have been fabricated by the UV-replication method described in section 4.3.2. For this tests, the UV-replication in ORMOCER® material has been done on chips, which were already packaged on a TO-header and contacted by wire-bonding. The material has been directly dispensed on top of the chip. Figure 5.10 shows an example picture of such a device with a replicated 2x2 lens array on top.

For the characterization of the coupling efficiencies, a tuneable precision laser current source and a fiber-optical power-meter have been used. The alignment of the fiber with respect to the VCSEL has been accomplished with a triaxial precision translational stage and a vision system. The axial distance between VCSEL and fiber facet has been measured with help of a linear displacement sensor. With the same setup, the lateral fiber displacement tolerance curves have been determined in an automated measurement.

The two presented sample chips have been prepared with diffractive lenses (designed for the fourth diffraction order and originated by direct laser writing) in a robot-assisted replication process, as described in section 4.3.

The designed distance between the lens and the fiber has been chosen as $z_{12} = 400\mu m$ for both examples. In order to compare the measurements with the theoretical results of section 5.4.2, two different distances between

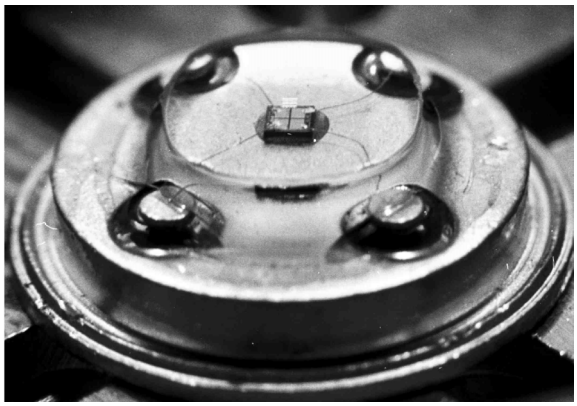

Figure 5.10: 2x2 VCSEL array mounted on a TO-39 package header with diffractive lenses, replicated in ORMOCER for multimode fiber coupling.

the VCSEL and the lens have been chosen: $z_{01} = 200\,\mu m$ (lens A) and $z_{01} = 400\,\mu m$ (lens B), respectively.

Lens A is designed analogue to the theoretical example represented in figure 5.8a) and lens B is equivalent to the lens represented by figure 5.8c), in terms of the imaging properties.

From figure 5.9b), the diffraction efficiencies for lens A and lens B are expected to be in the order of $\eta_l = 0.6$ and $\eta_l = 0.7$, respectively. The characterization results for both samples are summarized in the figures 5.11 and 5.12, respectively.

The curves shown in figures 5.11a) and 5.12a) display the absolute fiber coupling efficiencies (normalized to the output of the VCSEL) as a function of the operation current. Plots 5.11b) and 5.12b) show the fiber launch power as a function of the transversal displacement of the fiber from the optimum position. In addition, the lateral scans and the current curves have been repeated for different axial fiber positions. The solid, dashed and dotted lines in the plots account for longitudinal displacements $\Delta z = -100$, 0 and $+100\,\mu m$ of the fiber with respect to the designed focal position.

The measurements confirm that losses in the fiber coupling efficiency less than $0.5\,dB$ (0.1), compared to the maximum can be achieved with lateral alignment tolerances of $\pm 10\,\mu m$. As expected from the estimations of the diffractive lens efficiency (section 5.4.3), the coupling efficiency decreases with the VCSEL current, due to the increasing beam divergence. Both lenses yield similar maximum fiber launch efficiencies.

Taking the estimated values for the diffraction efficiency of the diffractive lens into account, a fraction of approximately $30\,\% - 40\,\%$ of the optical power is distributed among "stray-light" diffraction order. These orders are

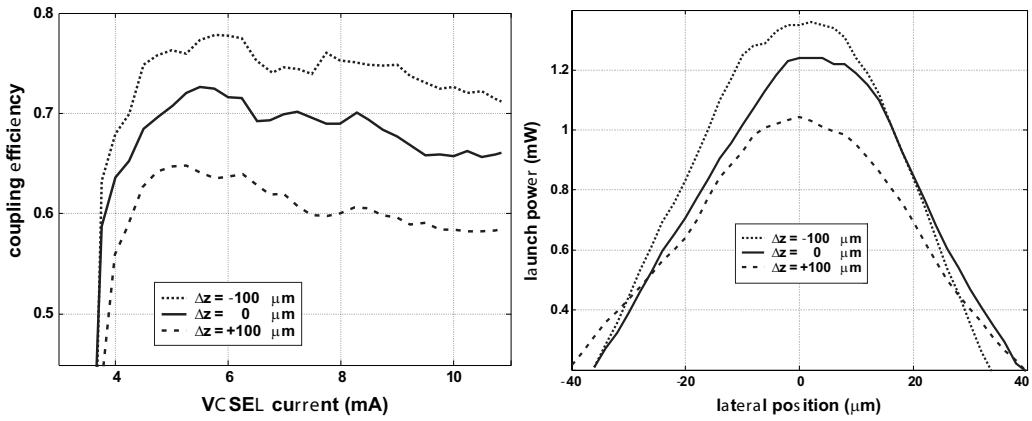

Figure 5.11: Lens A: a) absolute coupling efficiency as a function of the VCSEL current and b) fiber launch power at $I = 10\,mA$ as a function of the lateral fiber displacement for $z_{01} = 200\,\mu m$, $z_{12} = 400\,\mu m$ and $M = 4$. The different lines refer to a longitudinal displacement Δz of $-100\,\mu m$ (solid), $0\,\mu m$ (dashed) and $+100\,\mu m$ (dotted) of the fiber with respect to the designed focal position.

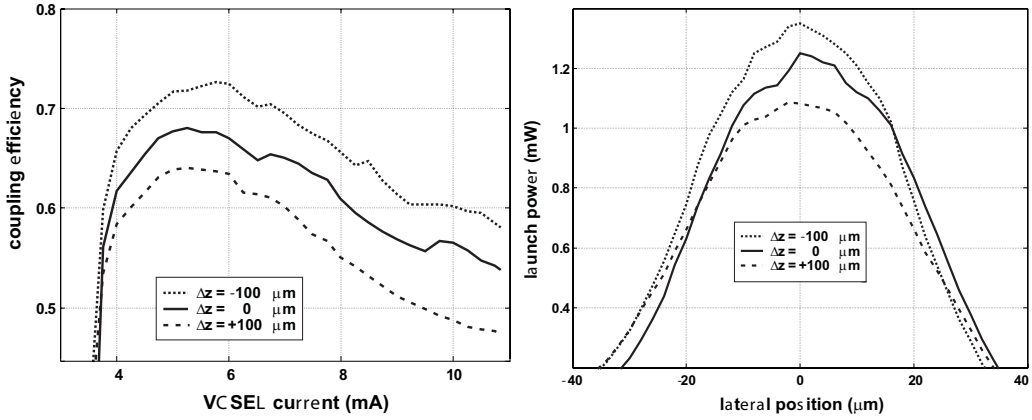

Figure 5.12: Lens B: a) absolute fiber coupling efficiencies as a function of I and b) fiber launch power at $I = 10\,mA$ as a function of the lateral fiber displacement for $z_{01} = 400\,\mu m$, $z_{12} = 400\,\mu m$ and $M = 4$.

also partially coupled into the fiber, as theoretically predicted by the results of section 5.4.4. A confirmation therefore is given by the fact, that both samples show an increase of the fiber launch efficiency, if the fiber is shifted closer to the lens from the design focal position. For an axial displacement

$\Delta z = -100\,\mu m$, this increase is between a factor of 0.05 and 0.1. This values agree well with the theoretical results summarized in tables 5.4 and 5.5.

An explanation for the more significant decrease of the fiber launch efficiency for lens B can also be derived from this theoretical studies, since here most of the "stray-light" orders are coupled in with lower efficiency. In particular, higher order LP-modes (which are dominant for $I \gtrsim 3\,mA$) are coupled less efficient with diffraction orders $m < M$, in comparison to lens A.

The two presented examples have been processed with discrete chips after dicing and bonding. However, as mentioned in section 4.3.2, the aim of the future work is to extend the ORMOCER® replication process to full wafer-scale compatibility. Therefore, it is required to combine the relief transfer via UV-replication with lithographic masking.

First experiments using this technology have shown very promising results. Figure 5.13 illustrates an example of a diffractive lens replicated on top of a VCSEL wafer.

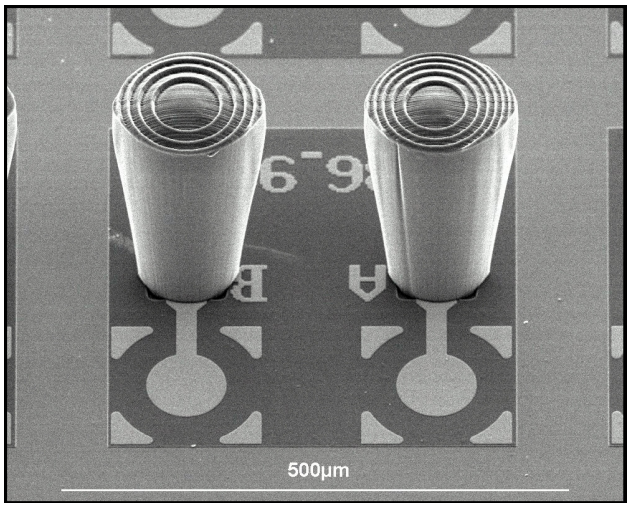

Figure 5.13: Scanning electron microscope image of monolithic integrated diffractive microlenses on a VCSEL wafer The distance of the diffractive lenses to the chip surface is approximately $250\,\mu m$. The devices have been fabricated by a combined Sol-Gel replication and lithography process on wafer-scale level. Picture courtesy of Christiane Gimkiewicz.

The picture shows two columns of replicated ORMOCER® material, defined by lithographic apertures of $125\,\mu m$ diameter and a transferred relief of a diffractive lens on top. The height of the columns is approximately $250\,\mu m$ and the pitch of the VCSELs is $250\,\mu m$.

5.6 Conclusions

A monolithic integration of diffractive micro-lenses on VCSEL chips and wafers by a ORMOCER® casting process has been successfully demonstrated. It has been shown, that the process is feasible and has the potential to be extended to full wafer-scale compatibility. Early experiments with combined UV-casting and lithography have shown very promising results. A wafer-scale processing is the enabling factor for a low-cost fabrication in large quantities and for the integration of other elements, or the realization of more complex microsystems.

The characterization of first fabricated test samples, has proven a coupling efficiency better than $\eta = 0.7$ over the full operation range of the VCSEL. Assuming maximum lateral fiber offset tolerances of $\pm 10\,\mu m$, a loss in the maximum fiber launch power less than $0.5\,dB$ for a lateral displacement and less than $0.1\,dB$ for a longitudinal displacement has been found. Such tolerances are sufficient for passive fiber alignment in most practical applications.

Furthermore, a mathematical description for the source characteristics of the VCSEL based on a step index fiber model has been developed and fitted to the measured beam properties. A mathematical procedure for the propagation of the (scalar) mode fields through the system, the calculation of the fiber coupling efficiency and a model for the estimation of the efficiency of the diffractive lens has been presented. In addition, the coupling behavior of individual modes has been investigated for different system geometries and also for non-design diffraction orders of the lens. In this manner, the coupling of "stray-light" diffraction orders could be investigated. The results of these simulations have shown a very good agreement with the experimental data.

Chapter 6

Summary

Direct laser writing is a versatile method for a fast prototyping or production of smaller quantities of micro-optical elements. It is well suited for the origination of elements for subsequent replication. However, due to the finite size of the writing spot, the resolution for this fabrication method is limited.

We have presented a mathematical method for the consideration of the fabrication inherent smoothing effects during the design phase of diffractive optical elements and have shown theoretical as well as experimental examples for the optimization of the diffraction efficiency of blazed gratings and fan-out elements. Therefore, different optimization methods based on pure geometrical considerations and on a iterative Fourier transform algorithm based on scalar diffraction theory have been discussed. In addition, a full vectorial diffraction optimization method by simulated annealing has been presented and promising theoretical results could be demonstrated.

One disadvantage of diffractive optical elements over conventional refractive elements is the typically higher level of stray light in presence of fabrication errors or a mismatch between illumination wavelength and design wavelength. We have introduced an alternative concept for the non-regular encoding of a diffractive phase function, which can be used to lower stray-light effects under such circumstances. The application of this method typically results in an unconventional type of elements with non-periodic zones, which we have called diffractive optical elements with modulated zone sizes. It has been demonstrated, that such elements can still be classified as diffractive optical elements. Several numerical and experimental examples for the improvement of the spectral tolerances and the relaxation of fabrication tolerances of diffractive lenses and blazed gratings could be given.

Elements for specific applications, such as diffractive optical elements for mid-infrared wavelengths or mechanical alignment and assembly features, often require the fabrication of structures with profile depths in the order of

$d = 20\,\mu m$ or more. Standard photolithographic resist processing techniques do not address this range. We could demonstrate the successful fabrication of diffractive lens arrays for a infrared sensing application by direct laser writing with thicknesses up to $d = 20\,\mu m$. A photoresist processing for films of thicknesses up to $d = 70\,\mu m$ has been developed for the fabrication of mechanical fiber guide assembly structures by mask lithography.

Although such non-standard lithographic techniques are not suitable for low-cost production, they can be used for the fabrication of master originals for replication (e. g. injection molding, hot-embossing or UV-casting). We have described a UV-casting method, which is suitable for the replication of deep structures, but also of structures with sub-micron feature sizes, using hybrid inorganic-organic polymers of type ORMOCER® (which are commercially available Sol-Gel materials). This materials have very good optical, chemical and mechanical properties and can be lithographically processed. Therefore, they are also suitable for a replication of micro-optical or mechanical elements on wafer-scale.

The advantages of the ORMOCER® replication technique have been exploited for a monolithic integration of diffractive microlenses on VCSEL chips or wafers for multimode fiber coupling. For this purpose, a detailed description of the characterization of the VCSELs, the modelling of the source beam by LP-modes of a circular step index fiber and the simulation of the mode propagation through the system has been given. In addition, methods for the estimation the diffractive lens efficiency and the fiber coupling efficiency has been described. The coupling behavior of individual modes has been investigated for different system geometries and also for non-design diffraction orders of the lens, which has given an insight to effects of stray-light caused by relief imperfections of the diffractive lens.

Samples of diffractive lenses integrated on discrete VCSEL chips have been fabricated and characterized. The measured results agree very well with the numerical simulations and have yielded coupling efficiencies better than 0.7, almost constant over the whole operation range. Such efficiencies have been achieved while maintaining fiber misalignment tolerances, which can be met by passive alignment. Finally, we have presented first experimental results of a replication of diffractive lenses on VCSELs in a full wafer-scale process, which look very promising. The aim of the future work on this subject should be the further development of this wafer-scale processing and its application to the fiber guiding structures and possibly other micro-optical or -mechanical elements. This process has a high potential for low-cost mass fabrication and for the realization of more complex optical and opto-mechanical subassemblies or microsystems.

Acknowledgements

This work has been carried out with the Photonics Group of the Centre Suisse d'Electronique et de Microtechnique (CSEM) in Zürich, Switzerland. I am grateful to all people who where involved or have supported me somehow or other during the course of this work. In particular i would like to thank:

- Prof. René Dändliker for directing this thesis and his enduring support during good and hard times.
- Dr. Markus Rossi (Heptagon) for supervising this work, for many useful discussions, for his fruitful contributions to this work and for his participation in the jury.
- The members of the jury Prof. Hans-Peter Herzig and Prof. Jürgen Jahns (Fernuni Hagen) for their kind assistance.
- Michael T. Gale for his supervision and constant support.
- Dr. Gerd Blau (Alcatel) as well as Dr. Christiane Gimkiewicz, Susanne Westenhöfer, Christian Zschokke and Hans Thiele of the CSEM Zürich for their friendship, their active support of my work and for countless discussions.
- Prof. Hans Beck, Prof. Yves Baer and Prof. Fausto Pellandini for their patience and assistance in my preparation for additional examinations.
- All other members of the Photonics group and the other groups of CSEM Zürich for the good time and atmosphere.
- The members of the Applied Optics group of the Institute of Microtechnology (University of Neuchâtel).
- Dr. Ilkka Kallioniemi (Heptagon) and Dr. Andreas Schilling (OVD Kinegram) for their contribution to this work and for many pub visits.

- Dr. Gian Luca Bona, Dr. Roland Germann and Dr. Christoph Berger of IBM Zurich Research Laboratory.
- Dr. Michael Moser, Dr. Stephan Hunziker, Dr. Marcel Brunner, Dr. Hans-Peter Gauggel, Arthur Vonlanthen and their colleagues of Avalon Photonics for providing many VCSELs and tons of information.
- My friends Dr. Philipp Zeller, Dr. Robert Lange, Michael Richter and Gerben Boer for many shared beers, whiskey and grappa.
- My girlfriend Irena for her patience and for enduring all the troubles.
- And last not least, my parents for their moral support.

Bibliography

[1] I. Aeby, "Oxide VCSELs rise to the challenge," *Compound Semiconductor Magazine*, vol. 7, no. 5, 2001.

[2] Electronicast, "Vertical surface emitting laser (VCSEL) transceiver market forecast," November 2000. www.electronicast.com.

[3] J. Turunen and F. Wyrowski, *Diffractive Optics for Industrial and Commercial Applications*. Berlin: Akademie Verlag, 1997.

[4] H. Dammann, "Blazed synthetic phase only holograms," *Optik*, vol. 31, pp. 95–104, 1970.

[5] L. B. Lesem, P. Hirsch, and J. A. Jordan Jr., "The kinoform: a new wavefront reconstruction device," *IBM Journal of Research & Development*, vol. 13, no. 2, p. 150, 1969.

[6] J. A. Jordan Jr., P. M. Hirsch, L. B. Lesem, and D. L. Van Rooy, "Kinoform lenses," *Appl. Opt.*, vol. 9, no. 8, p. 1883, 1970.

[7] P. W. Oliveira, H. Krug, H. Künstle, and H. Schmidt, "The production of fresnel lenses in sol-gel derived ormocers by holography," *Proc. SPIE*, vol. 2288, pp. 554–562, 1994.

[8] P. Äyräs, J. T. Rantala, S. Honkanen, S. B. Mendes, and N. Peyghambarian, "Diffraction gratings in sol-gel films by direct contact printing using a UV-mercury lamp," *Opt. Comm.*, vol. 162, pp. 215–218, 1999.

[9] S. I. Najafi, T. Touam, R. Sara, M. P. Anrews, and M. A. Fardad, "Sol-gel glass waveguide and grating on silicon," *J. Lightwave Technol.*, vol. 16, no. 9, pp. 1640–1646, 1998.

[10] T. J. Suleski, "Roadmap for micro-optics fabrication," *Proc. SPIE*, vol. 4440, pp. 1–15, 2001.

[11] M. Ekberg, F. Nikolajeff, M. Larsson, and S. Hård, "Proximity-compensated blazed transmission grating manufacture with direct-writing electron lithography," *Appl. Opt.*, vol. 33, pp. 103–107, 1994.

[12] F. Nikolajeff, J. Bengtsson, M. Larsson, M. Ekberg, and S. Hård, "Measuring and modelling the proximity effect in direct write electron-beam lithography kinoforms," *Appl. Opt.*, vol. 34, pp. 897–903, 1995.

[13] H. P. Herzig, *Micro-Optics: Elements, Systems and Applications.* Bristol: Taylor and Francis, 1997.

[14] D. A. Pommet, M. G. Moharam, and E. B. Grann, "Limits of scalar diffraction theory for diffractive phase elements," *J. Opt. Soc. Am. A*, vol. 11, pp. 1827–1834, 1994.

[15] T. Hessler, *Continous-Relief Diffractive Optical Elements: Design, Fabrication and Application.* PhD thesis, University of Neuchâtel, Switzerland, 1998.

[16] J. Bengtson, "Direct inclusion of the proximity effect in the calculation of kinoforms," *Appl. Opt.*, vol. 33, pp. 4993–4996, 1994.

[17] P. Ehbets, *Efficient phase gratings for beam splitting and beam shaping.* PhD thesis, University of Neuchâtel, Switzerland, 1996.

[18] R. W. Gerchberg and W. O. Saxton, "A practical algorithm for the determination of phase from image and diffraction plane pictures," *Optik*, vol. 35, pp. 227–246, 1972.

[19] M. T. Eismann, A. M. Tai, and J. Cederquist, "Iterative design of a holographic beamformer," *Appl. Opt.*, vol. 28, pp. 2641–2650, 1989.

[20] D. Daly, S. M. Hodson, and M. C. Hutley, "Fan-out gratings with a continuous profile," *Opt. Comm.*, vol. 82, p. 183, 1990.

[21] H. P. Herzig, D. Prongué, and R. Dändliker, "Design and fabrication of highly efficient fan-out elements," *Proc. SPIE*, vol. 1359, p. 219, 1990.

[22] D. Prongué, H. P. Herzig, R. Dändliker, and M. T. Gale, "Optimized kinoform structures for highly efficient fan-out elements," *Appl. Opt.*, vol. 31, p. 5706, 1992.

[23] P. Ehbets, M. Rossi, and H. P. Herzig, "Continuous-relief fan-out elements with optimized fabrication tolerances," *Opt. Eng.*, vol. 34, p. 3456, 1995.

[24] J. R. Fienup, "Iterative method applied to image reconstruction and to computer-generated holograms," *Opt. Eng.*, vol. 19, pp. 297–305, 1980.

[25] F. Wyrowski and O. Bryngdahl, "Iterative fourier-transform algorithm applied to computer holography," *J. Opt. Soc. Am. A*, vol. 5, pp. 1058–1065, 1988.

[26] J. W. Goodman, *Introduction to Fourier Optics*. New York: McGraw-Hill, 1968.

[27] J. D. Gaskill, *Linear Systems, Fourier Transforms and Optics*. New York: John Wiley & Sons, 1978.

[28] B. E. A. Saleh and M. C. Teich, *Fundamentals of Photonics*. New York: John Wiley & Sons, 1991.

[29] A. G. Kirk and T. J. Hall, "Design of binary computer generated holograms by simulated annealing: coding density and reconstruction error," *Opt. Comm.*, vol. 94, no. 6, pp. 491–496, 1992.

[30] A. G. Kirk and T. J. Hall, "Design of binary computer generated holograms by simulated annealing," *J. mod. Opt.*, vol. 39, no. 12, pp. 2531–2539, 1992.

[31] D. Daly, S. M. Hodson, and M. C. Hutley, "Fan-out gratings with a continuous profile," *Opt. Comm.*, vol. 82, pp. 183–187, 1991.

[32] N. Sergienko, J. J. Stamnes, V. Kettunen, M. Kuitinnen, J. Turunen, P. Vahimaa, and A. T. Friberg, "Comparison of electromagnetic and scalar methods for evaluation of diffractive lenses," *J. mod. Opt.*, vol. 46, no. 1, pp. 65–82, 1999.

[33] N. Sergienko, J. J. Stamnes, V. Kettunen, M. Kuitinnen, J. Turunen, P. Vahimaa, and A. T. Friberg, "Asymptotic methods for evaluation of diffractive lenses," *J. Opt. A: Pure Appl. Opt.*, vol. 1, pp. 552–559, 1999.

[34] N. Sergienko and J. J. Stamnes, "Diffracted-ray approach to the fast evaluation of diffractive lenses," *Appl. Opt.*, vol. 39, no. 16, pp. 2539–2544, 2000.

[35] M. Rossi and R. E. Kunz, "Phase-matched fresnel elements for fan-out application," *Proc. IEE*, vol. 379, p. 27, 1993.

[36] W. C. Sweatt, "Mathematical equivalence between a holographic optical element and an ultra-high index lens," *J. Opt. Soc. Am.*, vol. 69, p. 486, 1979.

[37] M. G. Moharam and T. K. Gaylord, "Rigorous coupled-wave analysis of planar-grating diffraction," *J. Opt. Soc. Am.*, vol. 71, pp. 811–818, 1981.

[38] M. G. Moharam and T. K. Gaylord, "Three dimensional vector coupled-wave analysis of planar-grating diffraction," *J. Opt. Soc. Am.*, vol. 73, p. 1105, 1983.

[39] A. Schilling, *Diffractive and Refractive Optical Microstructures: Theory, Design and Applications.* PhD thesis, University of Neuchâtel, Switzerland, 2000.

[40] M. Rossi and T. Hessler, "Stray-light effects of diffractive beam-shaping elements in optical microsystems," *Appl. Optics-IP*, vol. 38, no. 14, pp. 3068–3076, 1999.

[41] R. E. Kunz and M. Rossi, "Phase matched fresnel elements," *Opt. Comm.*, vol. 97, pp. 6–9, 1993.

[42] M. Born and E. Wolf, *Principles of Optics.* Cambridge USA: Cambridge University Press, 1977.

[43] D. A. Buralli and G. M. Morris, "Optical performance of holographic kinoforms," *Appl. Opt.*, vol. 28, pp. 976–983, 1989.

[44] T. Hessler, M. Rossi, R. E. Kunz, and M. T. Gale, "Analysis and optimization of fabrication of continuous-relief diffractive optical elements," *Appl. Optics-OT*, vol. 37, no. 19, pp. 4069–4079, 1998.

[45] A. E. Siegman, *Lasers.* Mill Valley: University Science Books, 1986.

[46] D. Faklis and G. M. Morris, "Spectral properties of multiorder diffractive lenses," *Appl. Opt.*, vol. 34, pp. 2462–2468, 1995.

[47] J. J. Stamnes, *Waves in Focal Regions.* Bristol: Adam Hilger, 1986.

[48] M. Abramowitz and I. A. Stegun, *Handbook of Mathematical Functions with Formulas, Graphs and Mathematical Tables.* New York: Dover Publications, 1965.

[49] J. A. Waddie and M. R. Taghizadeh, "Interference effects in far-field diffractive optical elements," *Appl. Opt.*, vol. 38, no. 28, pp. 5915–5919, 1999.

[50] M. Rossi and T. Ammer, "Replicated diffractive optical elements for IR applications," *European Optical Society Topical Digest Meetings Series*, vol. 22, pp. 44–45, 1999.

[51] C. G. Blough, M. Rossi, S. K. Mack, and R. L. Michaels, "Single-point diamond turning and replication of visible and near-infrared diffractive optical elements," *Appl. Opt.*, vol. 36, no. 20, pp. 4648–4654, 1997.

[52] M. T. Gale, M. Rossi, J. S. Pedersen, and H. Schütz, "Fabrication of continuous-relief micro-optical elements by direct laser writing in photoresist," *Opt. Eng.*, vol. 33, pp. 3556–3566, 1994.

[53] M. Cumme, H. Hartung, L. C. Wittig, and E. B. Kley, "Thick refractive beam shaping elements applied to laser diodes," *Proc. SPIE*, vol. 4440, pp. 25–33, 2001.

[54] V. P. Korolkov, V. P. Koronkevich, A. I. Malyshev, and V. G. Nikitin, "New fabrication method for diffractive elements with deep phase relief," *Proc. SPIE*, vol. 3010, pp. 180–191, 1997.

[55] W. Flack, G. Newman, D. Bernard, J. Rey, Y. Granik, and V. Boksha, "Advanced simulation techniques for thick photoresist lithography," *Proc. SPIE*, vol. 3049, pp. 789–804, 1997.

[56] W. W. Flack, W. P. Fan, and S. White, "The optimization and characterization of ultra-thick phototresist films," *Proc. SPIE*, vol. 3333-67, 1998.

[57] M. S. Cohen, M. J. Cordes, S. A. Cordes, J. D. Gelorme, D. M. Kuchta, D. L. Lacey, J. Rosner, and J. L. Speidell, "Lithographically fabricated fiber guides for optical subassemblies," *Proc. 51th. Electronic Components & Technology Conference (ECTC), Orlando, Fl.*, pp. 229–237, 2001.

[58] *Trademark of Fraunhofer Gesellschaft.*

[59] P. Dannberg, L. Erdmann, R. Bierbaum, A. Krehl, and A. Bräuer, "Micro-optical elements and their integration to glass and optoelectronic wafers," *Microsys. Technol.*, vol. 6, pp. 41–47, 1999.

[60] M. Popall, A. Dabek, M. E. Robertsson, O. J. Gustafsson, G. andHagel, B. Olsowski, R. Buestrich, L. Cergel, M. Lebby, P. Kiely, J. Joly, D. Lambert, M. Schaub, and H. Reichl, "ORMOCERs - new, photo-patternable dielectric and optical materials for MCM-packaging," *Proc. 48th Electronic Components and Technology Conference (ECTC), Seattle, WA*, p. 1018, 1998.

[61] M. Popall, J. Kappel, J. Schulz, and H. Wolter, "Ormocers, inorganic-organic polymer materials for applications in micro systems technology," *Proc. 4th Int. Conf. on Micro Electro, Opto, Mechanical Systems and Components, Berlin*, p. 271, 1994.

[62] U. Streppel, C. Dannberg, P. Waechter, A. H. Braeuer, P. Nicole, L. Froehlich, R. Houbertz, and M. Popall, "Multilayer optical fan-out device composed of stacked monomode waveguides," *Proc. SPIE*, vol. 4453, p. paper 11, 2001.

[63] M. S. Cohen, G. W. Johnson, J. M. Trewhella, D. L. Lacey, M. M. Oprysko, D. L. Karst, S. M. DeFoster, W. K. Hogan, M. D. Peterson, and J. A. Weirick, "Low-cost fabrication of optical subassemblies," *IEEE Trans. on Components, Packaging and Manufucturing Technol. Part B: Adv. Packaging*, vol. 20, pp. 256–264, 1997.

[64] G. Nakagawa, K. Miura, M. Makiuchi, and M. Yano, "Highly efficient coupling between LD aray and optical fiber array using si microlens array," *IEEE Photonics Techn. Letters*, vol. 5, p. 1056, 1993.

[65] K. H. Hahn and D. W. Dolfi, "POLO: A gigabyte/s parallel optical link," *SPIE Optoelectronic Interconnects and Packaging*, vol. CR62, pp. 393–404, 1996.

[66] H. Karstensen, F. Auracher, N. Ebel, J. Fiedler, V. Plickert, L. Melchior, L. Leininger, M. Bittner, M. Festag, M. Wicke, S. Meyer, R. Miller, G. Kuhn, H.-L. Althaus, and A. Ebberg, "Module packaging for high-speed serial and parallel transmission," *Proc. 50th. Electronic Components & Technology Conference (ECTC), Las Vegas, NV*, pp. 479–486, 2000.

[67] H. P. Zappe, F. Monti di Sopra, H. P. Gauggel, M. Moser, R. Hövel, and K. Gulden, "Polarization and noise behaviour of narrow-linewidth 850 nm VCSELs," *Proc. Europ. Conf. on Opt. Comm. (ECOC), Nice*, vol. 2, p. 308, 1999.

[68] C. Degen, *Transverse mode formation in oxide-confined Vertical-Cavity-surfac-Emitting-Lasers: Analysis of the underlying mechanisms*. PhD thesis, Technische Universität Darmstadt, 2001.

[69] M. Brunner, *Design and Characterization of Single and Dual Cavity Oxide-Apertured VCSELs*. PhD thesis, École Polytechnique Fédérale de Lausanne, Switzerland, 2000.

[70] D. Gloge, "Weakly guiding fibers," *Appl. Opt.*, vol. 10, pp. 2252–2258, 1971.

[71] D. Marcuse, *Theory of Dielectric Optical Waveguides*. London: Academic Press, 1974.

[72] A. Yariv, *Quantum Electronics*. New York: John Wiley & Sons, 1988.

[73] C. Won, S. H. Yoo, K. Oh, U.-. C. Paek, and W. Jhe, "Near-field diffraction by a hollow-core optical fiber," *Opt. Comm.*, vol. 161, pp. 25–30, 1999.

[74] N. Delen and B. Hooker, "Free-space beam propagation between arbitrarily oriented planes based on full diffraction theory: A fast fourier transform approach," *J. Opt. Soc. Am. A*, vol. 15, no. 4, pp. 857–867, 1998.

[75] E. O. Brigham, *The Fast Fourier Transform*. Englewood Cliffs, N. J.: Prentice-Hall, 1974.

[76] D. G. Cunningham, M. C. Novell, P. Dowd, L. Raddatz, and I. H. White, "Modal noise penalties for data communication links employing large area VCSELs," *Electron. Lett.*, vol. 31, pp. 2147–2148, 1995.

Publications

List of Publications and Patents

I.* I. Kallioniemi, T. Ammer and M. Rossi, "Optimization of continuous profile blazed gratings using rigorous diffraction theory", Opt. Comm. 177, pp. 15-24, 2000.

II.* T. Ammer and M. Rossi, "Diffractive optical elements with modulated zone sizes", J. mod. Optics 47, pp. 2281-2293, 2000.

III.* M. Rossi, T. Ammer,M. T. Gale, A. Maciossek and J. Schtig, "Diffractive optical elements for passive infrared detectors", Technical Digest, OSA Conf. on Diffractive Optics and Micro-Optics, Quebec, CA, pp. 290, 2000.

IV.* T. Ammer, M. T. Gale and M. Rossi, "On-chip replication of micro-optical elements for VCSEL to fiber coupling", Proc. SPIE 4440, pp. 238-245, 2000.

V.* T. Ammer, M. T. Gale and M. Rossi, "Chip-level integrated diffractive optical microlenses for VCSEL to fiber coupling", submitted to Optical Engineering, 2001

VI. T. Ammer and M. Rossi, "Blazed gratings with non-periodic grating structure", Proc. Diffractive Optics Conf, Jena, Germany, pp. 28, 1999

VII. M. Rossi and T. Ammer, "Replicated diffractive optical elements for IR applications", Proc. Diffractive Optics Conf, Jena, Germany, pp. 44, 1999

VIII. G. Blau, M. Rossi, T. Ammer, M. T. Gale, H. P. Gauggel and K-. H. Gulden, "Aspherical Microlenses for Beam Shaping of VCSEL Arrays", Proc. Europ. Conf. on Opt. Comm. (ECOC), pp. 350, Nice 1999.

IX. T. Ammer, G. Blau and M. Rossi, "On-chip ORMOCER microlens replication for VCSEL to fiber coupling", Proc. Appl. Optics and Optoelectronics Conf., Loughborough, UK, pp. 89, 2000.

* *Publications I.-V. are attached to the thesis*

Patents

- T. Ammer and M. T. Gale, "Fabrication of continuous-relief alignment and assembly structures for optical microsystem integration", patent pending.

Abstracts of Publications

Publication I.

Optimization of continuous profile blazed gratings using rigorous diffraction theory

I. Kallioniemi, T. Ammer and M. Rossi

Surface-relief elements with a high diffraction efficiency play an important role in the industrialization of diffractive optics. Optimal methods for the design, analysis, and fabrication of diffracting structures are essential for producing high quality applications. Due to recent developments in the fabrication processes, it is possible to utilize continuous-profile gratings with periods on the order of few micrometers.

We present optimization results for deep continuous-profile blazed gratings with periods between 4 and 6 μm designed to work in the 3rd, 4th, or 5th diffraction order in the visible range. These gratings possess large diffraction angles, and thus they appear in the outer zones of diffractive lenses with a high numerical aperture (NA). The optimization is performed by the simulated annealing method and the diffraction is modelled with the Rigorous Coupled Wave Analysis, also taking into account the physical model of fabrication process. Improvements of several tens of percents in the diffraction efficiency are achieved. The sensitivity of the optimized structures to fabrication errors is analyzed.

Publication II.

Diffractive optical elements with modulated zone sizes

T. Ammer and M. Rossi

The standard design for phase-only diffractive optical elements comprises a transformation of the continuous phase function into a surface relief by means of wrapping the phase into regular intervals of $M2\pi$. This results in a structure with diffractive zones aligned in a horizontal plane. We present an alternative design concept with modulated zone sizes leading to non-periodic boundary positions and non-aligned surface structures. The diffractive properties are compared to those of conventional diffractive optical elements. It can be shown that they are fully equivalent for the design wavelength, but

exhibit a different spectral behavior for deviating wavelengths. Those properties are exploited for the improvement of the optical performance of blazed gratings and diffractive lenses under conditions of deviating wavelengths. Special emphasis is put on the optimization of the ratio between diffractive efficiencies of the design order and other orders for blazed gratings and focusing diffractive lenses as well as the suppression of interference effects within Gaussian beams collimated with diffractive lenses.

Publication III.

Diffractive optical elements for passive infrared detectors
M. Rossi, T. Ammer, M. T. Gale, A. Maciossek, J. Söchtig and C. Ferrari

Complex diffractive lens arrays for passive infrared detection systems have been designed and fabricated by laser beam writing and injection moulding. Continuous relief profiles with depths up to $20\,\mu m$ were originated, characterized and replicated.

Publication IV.

On-chip replication of micro-optical elements for VCSEL to fiber coupling
T. Ammer, M. T. Gale and M. Rossi

We present the design and fabrication of optical microsystems based on UV-replication techniques using Ormocer® materials. An integration of the optical and mechanical structures on chip level is demonstrated for Vertical Surface Emitting Lasers (VCSEL). VCSEL's are of increasing interest for various fields such as telecommunication, optical sensing and optical interconnects. UV-replication techniques using Ormocer® materials offer a cost-effective way of integrating micro-optical elements directly on the chip with reduced assembly effort. Structures up to several hundred microns thickness and alignment tolerances in the order of few microns can be produced. The method is suitable for the fabrication of single elements, arrays and is extendable to wafer-scale processing. The presented example is a system for the coupling of VCSEL arrays into multimode optical fibers. Two different approaches are followed: Focussing of the VCSEL output into the fiber using replicated microlenses and fiber butt-coupling of the VCSEL lasers

with help of replicated fiber alignment/guiding structures. Origination of the structure elements is accomplished by direct laser writing in photoresist and resist reflow techniques, respectively. Specific limitations of the corresponding fabrication method are already taken into account during element design and modelling. Results for the replicated lenses show a total fiber launch efficiency better than 70 % over the laser operational range. This performance can be met by passive fiber alignment with tolerances of approximately $\pm 10 \mu m$. In case of the replicated fiber alignment / guiding structures, fiber launch efficiencies better than 50 % over the operation range and maximum values better than 80 % are reported.

Publication V.

Chip-level integrated diffractive optical microlenses for VCSEL to fiber coupling

T. Ammer, M. T. Gale and M. Rossi

The standard assembly technologies for VCSEL to fiber coupling systems involve the integration of discrete elements with demanding requirements for alignment effort and time. We present a method for the monolithic integration of diffractive micro-lenses on chip-level. This process is based on a UV-casting replication technique using Ormocer® materials (hybrid organic-inorganic polymers). This method also offers the capability to be extended to a wafer-scale process.

A mathematical description for the propagation of the laser modes through the system and the resulting fiber coupling efficiency is presented. We use a model for the source characteristics of the VCSEL based on a step index fiber model for the simulation of the mode-field propagation. Furthermore, a model for the estimation of the diffraction efficiency of the lens is developed. Finally the simulations are compared with first experimental results of single replicated elements.

Experimental coupling efficiencies for a multimode fiber (50/125, $NA = 0.20$) better than 0.7 over the entire operation range of the VCSEL could be achieved. Losses below $0.5\,dB$ (10 %) were observed within lateral fiber displacement tolerances of $\pm 10\,\mu m$.

Publication VI.

Blazed gratings with non-periodic grating structure
T. Ammer and M. Rossi

The standard design of a phase-only blazed diffraction grating comprises a regular periodic structure with phase steps of $M2\pi$. We show that a regular periodicity is not a necessary condition for diffractive behavior and present an alternative design concept with arbitrarily varied zone sizes and boundary positions. The scalar diffraction efficiencies are compared to those of common periodical gratings. It can be shown that the diffraction properties are fully equivalent for the design wavelength, but exhibit a different spectral behavior for deviating wavelengths. In addition to the discrete diffraction orders of a regular grating, new orders occur in the vicinity of the design order and peak stray light levels are lowered. These specific properties are used to optimize the signal to noise ratio of such an element by means of simulated annealing.

Publication VII.

Replicated diffractive optical elements for IR applications
M. Rossi and T. Ammer

Diffractive elements replicated in plastic materials have found many applications in the visible wavelength range. Elements for the infrared typically have lower requirements on the lateral resolution of the fabrication technology. However, when the commonly used materials as germanium or zinc selenide are to be replaced by replicated plastic materials with low indices of refraction profile depths of up to $20\,\mu m$ have to be fabricated for diffractive lenses, which is no longer in the range of standard photolithography fabrication processes. We optimized the processing parameters of direct laser beam writing to obtain high-quality continuous reliefs suited for applications in the mid-infrared. The fabrication limits and tolerances of $20\,\mu m$ deep diffractive profiles are modelled and compared with experimental data. The ability to fabricate deep photoresist profiles with a direct write technology opens many new applications for low-cost diffractive optical elements operating in the infrared. As an example we will present experimental results of high numerical aperture (NA), large area ($50x45mm$) lens arrays.

Publication VIII.

Aspherical Microlenses for Beam Shaping of VCSEL Arrays
G. Blau, M. Rossi, T. Ammer, M. T. Gale, H. P. Gauggel and K-. H. Gulden

Vertical Cavity Surface Emitting Lasers (VCSELs) for gas sensing, optical interconnects or waveguide applications require in most cases well collimated or focussed output beams. Refractive and diffractive lens arrays have been designed for a $125\,\mu m$ spaced $2x2$ custom-made, top emitting VCSEL array at a wavelength of $762\,nm$. The lenses have been fabricated by replication of a laser written, continuous profile, Diffractive Optical Element (DOE) or a commercial spherical lens. The combination of a diffractive surface profile on a refractive lens for spherical aberration correction and monolithic integration of the microlens onto the VCSEL chip are discussed.

Publication IX.

On-chip ORMOCER microlens replication for VCSEL to fiber coupling
T. Ammer, G. Blau and M. Rossi

We present an approach towards optical microsystem design and fabrication using a UV-casting technique based on ORMOCER® materials. Microlens singlets and arrays are directly integrated on chip level with Vertical Cavity Surface Emitting Laser (VCSEL) arrays. An application for the coupling of VCSEL's into multimode optical fibers is discussed. The lenses are designed, fabricated by direct laser writing and replicated onto the VCSEL chip

Publication I

15 April 2000

ELSEVIER

Optics Communications 177 (2000) 15–24

OPTICS COMMUNICATIONS

www.elsevier.com/locate/optcom

Optimization of continuous-profile blazed gratings using rigorous diffraction theory

Ilkka Kallioniemi [a,*], Thomas Ammer [b], Markus Rossi [b]

[a] *Helsinki University of Technology, Dept. of Engineering Physics and Mathematics, FIN-02015 HUT, Finland*
[b] *Centre Suisse d'Electronique et de Microtechnique, Zürich, Switzerland*

Received 7 December 1999; received in revised form 27 January 2000; accepted 10 February 2000

Abstract

Surface-relief elements with a high diffraction efficiency play an important role in the industrialization of diffractive optics. Optimal methods for the design, analysis, and fabrication of diffracting structures are essential for producing high quality applications. With direct laser beam writing it is possible to produce deep continuous-profile diffractive lenses and gratings with periods on the order of few micrometers. The finite size of the writing beam cannot be neglected as the period becomes comparable to the wavelength of the laser. We present optimization results for deep continuous-profile blazed gratings with periods between 4 and 6 μm designed to work in the 3rd, 4th, or 5th diffraction order in the visible range. These gratings possess large diffraction angles, and thus they appear in the outer zones of diffractive lenses with a high numerical aperture (NA). Optimization of the profiles is essential for practical applications, since the diffraction efficiency drops significantly because of smoothing caused by the finite size of the writing beam. The proposed optimization scheme utilizes the simulated annealing method and models the diffraction with the rigorous coupled wave analysis. Improvements of several tens of percents in the diffraction efficiency are achieved. The sensitivity of the optimized structures to fabrication errors is analyzed.

PACS: 42.79.D; 02.60.Pn; 42.82.Cr
Keywords: Blazed gratings; Direct laser writing; Simulated annealing

1. Introduction

An important and growing branch of applications in diffractive optics is based on surface-relief microstructures. Applications include, among others, the focusing, shaping, steering, and splitting of an incident laser beam. These optical functions are realized by modifying the amplitude and/or phase of light. An advantage of diffractive optics is the possibility for miniaturization in both the size and weight of the optical elements. Even more importantly, diffractive optics enables completely new solutions which have no refractive counterparts.

Well-established lithographic methods adapted from the VLSI technology are utilized for the fabrication processes. Furthermore, the elements can be tightly packed to form arrays of, e.g., micro lenses,

* Corresponding author. Helsinki University of Technology, Materials Physics Laboratory, P.O. Box 2200, FIN-02015 HUT, Finland. Tel. +358-9-451 3157; Fax. +358-9-451 3164; e-mail: Ilkka. Kallioniemi@hut.fi

0030-4018/00/$ - see front matter
PII: S0030-4018(00)00570-8

or they can be integrated into larger systems with laser diodes and optical waveguides [1,2].

Diffractive optical elements (DOE) are often categorized according to their surface profile. It can either be binary or continuous. The former has a staircase-like structure, typically consisting of 2^N discrete depth values where N is the number of fabrication steps. The latter has a continuously changing depth profile shape which became technically feasible in the 1970's even for small periods [3]. Continuous surface-relief profiles are generated by direct laser beam writing, electron-beam writing, or by gray-tone lithography methods [1,4]. In this paper, we restrain ourselves to the optimization of continuous profiles produced by direct laser beam writing. Thereby, we consider profiles generated by scanning a focused laser beam over the surface of a thin photoresist film. The beam intensity is modulated in proportion to the computed exposure data. In this manner, continuous surface profiles can be achieved with one exposure- and development step.

It is often beneficial, or even necessary, to take into account the finite size of the writing laser beam when analyzing continuous-profile structures. This is done by convoluting the ideal designed profile with a Gaussian intensity distribution, resulting in a smoothed profile shape.

Blazed gratings are a preferred object to study the characteristics of the convolution effect since they play an important role in diffractive optics. In particular, the relief shape of the outer zones in a diffractive lens is well approximated by local blazed grating sections. In this fashion, a good estimate for the overall diffraction efficiency of the lens is provided. As the period of the grating becomes comparable to the beam size, the smoothing effect results in a significant drop of the diffraction efficiency, well below 100%. Thus, optimization of the relief shape is required to compensate for the smoothing. Therefore, we focus on the optimization of continuous-profile blazed gratings working in a design diffraction order denoted by M, without loss of generality.

Modeling the diffraction from microstructures is customarily divided into methods based on the rigorous electromagnetic theory and methods based on the approximate scalar theory. The latter is valid for structures whose smallest features are on the order of 10 wavelengths or more, whereas rigorous diffraction theory is required when the grating has smaller feature sizes [5,6]. The most commonly used method for analyzing gratings with rigorous theory is the Rigorous Coupled Wave Analysis (RCWA) [7]. It is well suited in particular for binary gratings but can be used with continuous-profile gratings as well, assuming the profile is approximated with a large number of binary layers. Although the RCWA sets no restrictions for the smallest size of the features in the structure, it has the disadvantage of being restricted to periodic structures. However, the performance of several types of DOEs can be analyzed by approximating the structures locally as periodic gratings. Binary multilevel blazed gratings have been analyzed and optimized with RCWA by Noponen et al. in Ref. [8].

The next section will give a brief review on optimization of blazed gratings towards compensation of fabrication errors in the scalar domain. Sections 3 and 4 extend the analysis and concentrate on a more accurate and general approach employing an optimization algorithm based on the use of RCWA.

2. Review of the convolution model

The fabrication of DOEs is becoming an important factor for several industrial applications. A key role is assigned to diffractive gratings and lenses. A variety of manufacturing methods such as the diamond turning, binary mask lithography, gray-tone mask lithography, electron-beam lithography, and direct laser beam writing are already well established for this purpose [9].

The optical performance of DOEs is mainly determined by the reliability and precision of the fabrication process. In particular for diffractive lenses with a high value of NA or gratings with high diffraction angles, the smallest local feature size often reaches the resolution limits of the manufacturing process.

The factors that limit the resolution depend on the specific fabrication method. For raster scanning systems, such as the electron-beam lithography and direct laser beam writing, the dominant factors are the electron scattering (proximity effect) and the writing spot intensity distribution within the resist material, respectively. These effects tend to smooth sharp-edged vertical profile steps. Masking lithogra-

phy methods such as the binary mask (multilevel) and gray-tone lithography are mostly restricted to a minimum feature size due to mask diffraction and alignment errors. In addition, all lithographic processes are limited by the resist development characteristics. Diamond turned structures are smoothed by the finite radius of the stylus tip [10].

A mathematical model for the smoothing effect can be realized by convoluting the designed profile with an appropriate smoothing function. This function has to be separately determined for each specific fabrication method. In this fashion, the effect of relief smoothing on the diffraction efficiency of the DOE can be estimated numerically.

The smoothing effect due to binary mask lithography is exploited by Kuittinen et al. for improving the diffraction efficiency of gratings and diffractive lenses [11]. Ekberg and Nikolajeff et al. improve the efficiency for electron-beam written blazed gratings by precompensating the proximity effect [12,13]. They employ an iterative algorithm to optimize the electron dose profile. Hessler et al. have adapted a similar algorithm for the surface profile optimization of elements fabricated by direct laser beam writing [14].

The smoothing function in direct laser beam writing is adequately described by convoluting the designed exposure profile with a Gaussian laser spot intensity distribution. Hence, the normalized smoothing function is given by

$$g(x) = \frac{2}{w}\sqrt{\frac{\ln 2}{\pi}}\exp\left[-\left(\frac{2\sqrt{\ln 2}\,x}{w}\right)^2\right]. \qquad (1)$$

Here, w denotes the Gaussian spot diameter as full width at half maximum (FWHM). Notice that w does not necessarily coincide with the real writing spot diameter, since the circularly symmetric spot is reduced to a one-dimensional lateral exposure profile. This is physically justified by the fact that scanning over a certain location has the effect of integrating the intensity along the scanning direction. On the other hand, the spot size can also vary with the depth and development characteristics of the resist. Therefore, we shall refer to $g(x)$ as the 'effective writing spot'.

The convolution of the surface-relief profile, here denoted as $f(x)$, with $g(x)$ is accomplished by using the convolution theorem

$$\mathfrak{F}[f(x) \circledast g(x)] = F(\nu)\,G(\nu). \qquad (2)$$

Here $\mathfrak{F}$ denotes the Fourier-transform and $\circledast$ the convolution operation. Functions $F(\nu)$ and $G(\nu)$ are the Fourier transforms of $f(x)$ and $g(x)$, respectively. Since $g(x)$ is Gaussian, the transform $G(\nu)$ remains Gaussian with a size of the waist proportional to w^{-1}. Thus, Eq. (2) implies that the convolution has an effect similar to low-pass frequency filtering of $F(\nu)$. The larger the value of w, the more high spatial frequency components are suppressed from $F(\nu)$. Finally, by taking the inverse Fourier transform of Eq. (2), it is seen that the relief fidelity of the convoluted profile $[f(x) \circledast g(x)]$ is deteriorated from that of $f(x)$ due to smoothing. Consequently, as the local zones of the DOE reach feature sizes on the order of w, the convolution effect is no longer negligible. This is particularly the case for gratings designed to work with large diffraction angles and for lenses with high values of NA.

If the DOE is approximated as a thin phase element, the profile $f(x)$ can be directly converted into a phase transfer function. In this fashion, the scalar-diffraction efficiencies of convoluted phase reliefs can be easily derived by utilizing Eq. (2) in terms of Fourier optics [15].

Here, blazed gratings are considered with the diffraction geometry shown in Fig. 1. An initial,

Table 1
Diffraction efficiencies η_M calculated with scalar diffraction theory for smoothed blazed gratings. Results for three different non-optimized, $\eta_M(0)$, and convolution-optimized, $\eta_{M,\mathrm{opt}}$, blazed gratings of orders $M = 1,2$, and 4 are compared for different ratios w/Λ. Here w is the FWHM size of convoluting laser beam and Λ is the period of the grating.

w/Λ	$\eta_1(0)$ (%)	$\eta_{1,\mathrm{opt}}$ (%)	$\eta_2(0)$ (%)	$\eta_{2,\mathrm{opt}}$ (%)	$\eta_4(0)$ (%)	$\eta_{4,\mathrm{opt}}$ (%)
0.05	88.2	92.6	85.7	91.4	83.5	89.2
0.10	77.0	85.4	72.5	83.2	68.5	79.5
0.20	57.0	72.0	49.5	67.9	42.9	60.5
0.30	39.4	59.8	30.8	54.3	23.3	44.8
0.40	26.0	49.1	16.5	43.4	9.6	34.0
0.50	15.0	38.0	6.9	28.4	2.3	15.3

non-optimized value for the profile depth H is obtained from the thin element approximation, i.e.,

$$H(0) = \frac{M\lambda}{n_1 - n_0}. \quad (3)$$

Here λ is the wavelength, n_1 the refractive index of the element material and n_0 the ambient refractive index. The gratings are convoluted with the smoothing function given by Eq. (1). Calculated scalar-diffraction efficiencies η_M for various values of M and w, for non-optimized and optimized profiles are summarized in Table 1. The optimizations are done by using the iterative convolution-precompensation algorithm presented in Ref. [14]. From the table it can be observed that the diffraction efficiency for a blazed grating with $M = 1$ drops below 50% with as low values of w/Λ as 0.25. Here, Λ is the period of the grating.

It has to be emphasized that for a blazed grating with $M = 2$, the factor w/Λ only needs to be half as large as for the $M = 1$ case to obtain the same diffraction angle. Consequently, diffractive structures with $M > 1$ are less sensitive to convolution effects.

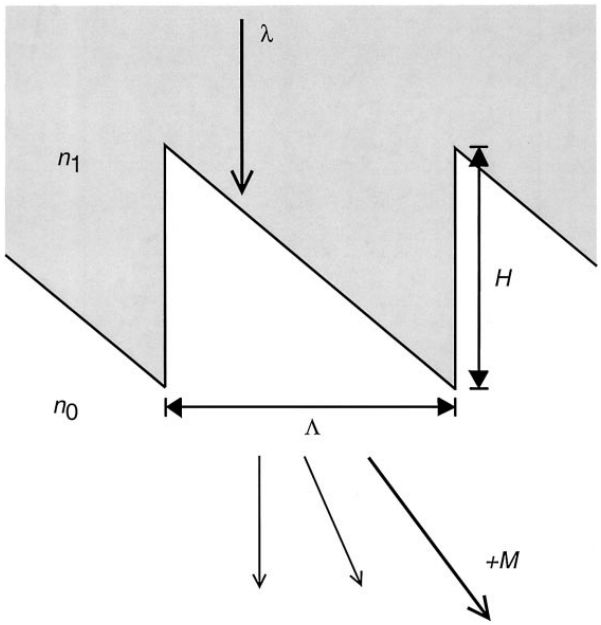

Fig. 1. Diffraction geometry for an ideal blazed grating. One period of the grating is denoted as Λ and the maximum depth as H. The incident light of wavelength λ is coming from a material with refractive index n_1 and is diffracted into a material with refractive index n_0. The grating is designed to steer the light into the Mth transmitted diffraction order.

The physical reason for this is that the convolution mainly affects sharp-edged discontinuities in the profile (between the zones) [14] – and the higher M, the less zones are required. Thus, by using $M > 1$ it is possible to fabricate blazed gratings with reasonable values of Λ, from the point of view of fabrication, even for large diffraction angles.

However, in spite of using gratings with $M > 1$, the period Λ can still become so small that scalar treatment fails. This can happen, e.g., in the outer zones of diffractive lenses with high values of NA. In this case the profiles need to be rigorously analyzed and optimized such that the beam size w is still taken into account. In the following sections we consider rigorous optimization of high order gratings with $M = 3$, 4, and 5 for values of Λ obtainable with a state of the art direct laser beam writing system.

3. Rigorous optimization algorithm

Here, blazed profiles are considered that work in the regime of rigorous diffraction theory, i.e., with $\Lambda \lesssim 10\lambda$. Furthermore, the maximum depth of the ideal profile is $H \approx 3$–$5\ \mu$m, depending on the value of M. An iterative optimization algorithm is used to choose the value of H and the shape of the non-convoluted profile such that the final, convoluted profile yields as high diffraction efficiency η_M as possible.

To start with, each period Λ in the ideal exposure profile (cf. Fig. 1) is divided into N_p non-overlapping pixels. Each pixel has a constant depth value h_j ($j = 1, \ldots, N_p$), normalized to H. The value of h_j is obtained by averaging the depth profile over region j, each of which is chosen 400 nm wide. This discretization is a typical value for state of the art laser writing systems [see chapter 4 in Ref. [2]] Thus the value of N_p is determined from

$$N_p = \frac{\Lambda\,(\mathrm{nm})}{400}. \quad (4)$$

An example of a discretized profile is shown in Fig. 2(a) with $N_p = 10$. The profile is subsequently smoothed by convoluting it with a Gaussian intensity distribution with FWHM of w, as explained in Section 2 in the context of the convolution theorem (2).

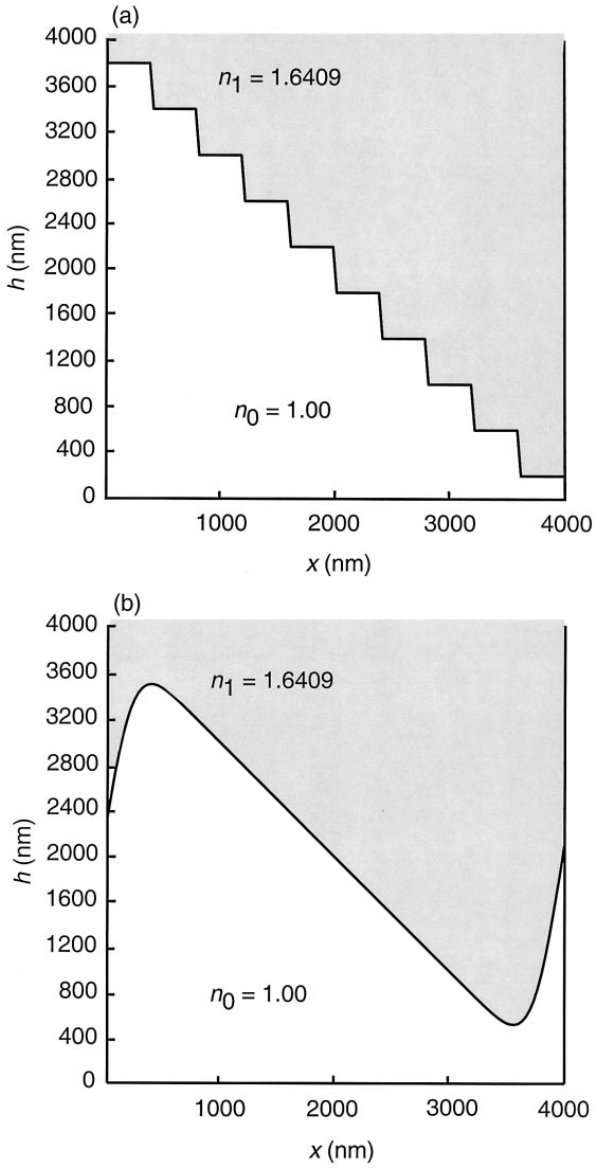

Fig. 2. Initial, non-optimized blazed grating with period $\Lambda = 4$ μm, designed to work in the $M = 4$th diffraction order. In (a) the discretized sawtooth profile with 400 nm wide steps, and in (b) the resulting continuous profile after convolution with a Gaussian beam from Eq. (1), using $w = 500$ nm.

An example of the smoothed profile is shown in Fig. 2(b).

Diffraction from the convoluted profile is calculated with the RCWA method by approximating the profile with 150 horizontal layers. Each layer has a piecewise-continuous refractive index distribution in the x direction. Total number of R diffraction orders are retained while calculating the field in each layer, and the calculation time is proportional to R^3. A trade-off value of $R = 31$ is chosen in the optimization in order that both the calculation time and achieved convergence of results remain acceptable. The resulting diffraction efficiencies η_i $(i = -N, \ldots, N)$ for transmitted propagating orders are used to evaluate a merit function. It is here chosen as

$$U[\boldsymbol{\eta}(n)] = \alpha_M [1 - \eta_M(n)]^2 + \sum_{p=-N, p\neq M}^{N} \alpha_p \eta_p(n)^2, \quad (5)$$

which is to be minimized. Here, the summation goes over all the retained diffraction orders, excluding M. The index n refers to an iteration step during the optimization. The coefficients α_i apply a weighting factor to each term. The merit function aims at

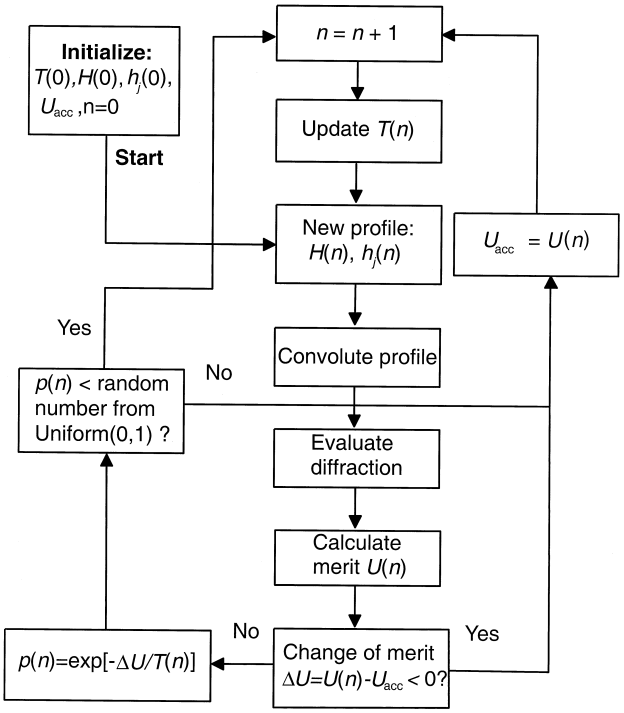

Fig. 3. Schematic diagram of the optimization algorithm used in this research. The algorithm combines the method of fast simulated annealing for changing the temperature $T(n)$, the convolution model of laser beam writing, and the rigorous diffraction theory for evaluating the diffraction from the convoluted profile. The iteration is stopped either after the accepted value of merit function, U_{acc} reaches a preset limit or a maximum number of iterations n has been finished.

maximizing the amount of light into the Mth order while it simultaneously tries to minimize light in the parasitic orders. Since the diffraction efficiencies for the merit function (5) are calculated from the smoothed grating profile, the convolution is accounted for in the optimization. Notice that the dependence of η_i on h_j is not explicitly denoted in Eq. (5).

As a result of the optimization, only the depth values h_j need to be preserved since they determine the profile. The smooth, continuous profile can be constructed by means of the convolution theorem if that is required. In practice, the exposure modulation for the fabrication process is determined from the values of h_j.

A suitable optimization algorithm is required to iteratively change the values of h_j such that the merit function (5) is minimized. A schematic diagram of the algorithm is shown in Fig. 3. Here, the adaptive simulated annealing (SA) [16] with fast cooling is applied to perform the optimization [17]. In addition to changing the values of h_j, the maximum depth H of the profile is allowed to change; the values of h_j need to be adapted after each change to H. It is necessary to set a maximum allowed value for H in order to avoid extremely peaky profiles. Because of the convolution effect, the depth of the fabricated profile is somewhat smaller than H [cf. Fig. 2(b)].

The free parameters can be changed one by time at each iteration step or as a lumped group. The former approach is chosen here. New candidates for the parameters are chosen from a limited range, namely

$$h_j(n) \in \left[h_{j,\mathrm{Best}} - \delta_j(n), h_{j,\mathrm{Best}} + \delta_j(n) \right], \qquad (6)$$

where $h_{j,\mathrm{Best}}$ represent the best values of the parameters found so far. Values of $\delta_j(n)$ are adjusted during the iteration. If the merit function does not improve for a certain number of iterations, the values of δ_j can be increased in order that larger changes in parameters become possible. However, it is advantageous to set maximum allowed values for δ_j in order to avoid peaky profiles and unrealistic situations from the point of view of fabrication. Initial values $h_j(0)$ and $H(0)$ have to be set before the iteration.

The SA algorithm has an adjustable internal parameter $T(n)$ which is called the temperature. It is slowly lowered during the iteration, and several schemes exist for managing this. Here, the value of $T(n)$ is continuously lowered according to

$$T(n) = T(0)\exp(-\beta n), \qquad (7)$$

where $T(0)$ is the initial temperature and β is a parameter governing the rate of change of the temperature. The latter should optimally depend on the number of free parameters and the final temperature one intends to achieve. An effective way for choosing β is proposed in Ref. [17]. The initial value $T(0)$ is chosen by first calculating the average value of the merit function (5) for random changes made to the initial values, $h_j(0)$. The value of $T(0)$ is then chosen as 1000 times larger than this average.

The core of SA is to accept changes to free parameters in such a way that the acceptance probability depends on $T(n)$. New values for $h_j(n)$ are accepted with probability one if they decrease the value of the merit function compared to the latest accepted value. On the contrary, if the value increases, the new parameters are accepted with the probability

$$p(n) = \exp\left[-\frac{\Delta U}{T(n)} \right]. \qquad (8)$$

Here $\Delta U = U[\boldsymbol{\eta}(n)] - U(\boldsymbol{\eta}_{\mathrm{acc}})$ is the change in the merit function from its last accepted (not necessarily the best) value. Thus, in the beginning of the optimization as the temperature is high, almost all of the changes are accepted, preventing the algorithm from being stuck to local minima. As the temperature lowers, the number of rejected changes increases. The algorithm is typically stopped after either a specified threshold value of the merit function is reached, or after a preset maximum number of iterations has been finished.

4. Optimization results

The optimization procedure discussed in Section 3 is applied for blazed gratings with three different periods $\Lambda = 4, 5.2$, or 6 μm designed to steer maximum amount of light into $M = 3$rd, 4th, or 5th diffraction order, i.e., nine cases in total. These examples illustrate the potential of rigorous diffraction theory in increasing the efficiency of high numerical aperture diffractive lenses.

Table 2
Rigorously calculated diffraction efficiencies into the Mth order for optimized, $\eta_{M,\mathrm{opt}}$, and initial, $\eta_M(0)$, smoothed blazed gratings. Smoothing is done with Gaussian beams [cf. Eq. (1)], using $w = 500$ nm. Efficiencies are shown as normalized to the total transmittance, which is given in columns 5 and 6 for optimized and initial profiles, respectively. Results are shown for three design orders, $M = 3,4$, and 5, with three values of period $\Lambda =$ 4,5.2, and 6 μm.

M	Λ (μm)	$\eta_{M,\mathrm{opt}}$ (%)	$\eta_M(0)$ (%)	Transmitted (%)	Transmitted(0) (0) (%)
3	4	**55.5**	28.1	90.5	59.1
3	5.2	**69.2**	51.7	89.1	82.6
3	6	**72.6**	61.7	85.4	86.1
4	4	**42.8**	3.7	73.2	32.6
4	5.2	**53.9**	10.3	91.8	49.7
4	6	**57.0**	26.7	80.2	76.9
5	4	**82.5**	3.9	90.1	63.5
5	5.2	**47.6**	7.8	80.3	29.5
5	6	**41.0**	0.3	78.5	29.5

As an initial guess for the profile, an ideal blazed grating (cf. Fig. 1) is convoluted with Gaussian beam shape from Eq. (1). The initial profile depth $H(0)$ is chosen by the thin element approximation, Eq. (3). Here we use TE-polarized incident light with wavelength $\lambda = 632.8$ nm, $n_0 = 1.0$ (air), and $n_1 = 1.6409$ for the resist material. The initial values $h_j(0)$ are obtained from $H(0)$ via

$$h_j(0) = \left[j - \tfrac{1}{2} \right] \frac{H(0)}{N_p}, \qquad (9)$$

where $j = 1, \ldots, N_p$. The corresponding optimized values, H_{opt} and $h_{j,\mathrm{opt}}$, are obtained with the algorithm from Section 3. The diffraction efficiencies η_M are calculated after the profile has been convoluted with the smoothing function (1), using $w = 500$ nm. It takes on the average 6.8 seconds to calculate diffraction with RCWA from one randomly modified profile with $R = 31$ retained orders, and the number of profiles generated is 50–100 times that of free parameters. Thus, for example with $M = 4$ and $\Lambda =$ 5.2 μm, the number of free parameters is 13 and the number of evaluations becomes 650–1300. Expressed in total computation time this corresponds to 73–146 minutes.

The rigorously calculated values of η_M for the initial and optimized profiles are shown in Table 2. Notice that the final values of η_M in this section are calculated with the number of retained orders $R = 81$ in order to yield well-converged results. The efficiencies are normalized to the sum of all transmitted diffraction orders. When the design order $M = 4$ or $M = 5$, it is seen that for the initial profile $\eta_M(0) <$ 10%, i.e., the non-optimized gratings completely fail to produce the desired optical function. This behavior has two explanations. Firstly, the initial depth

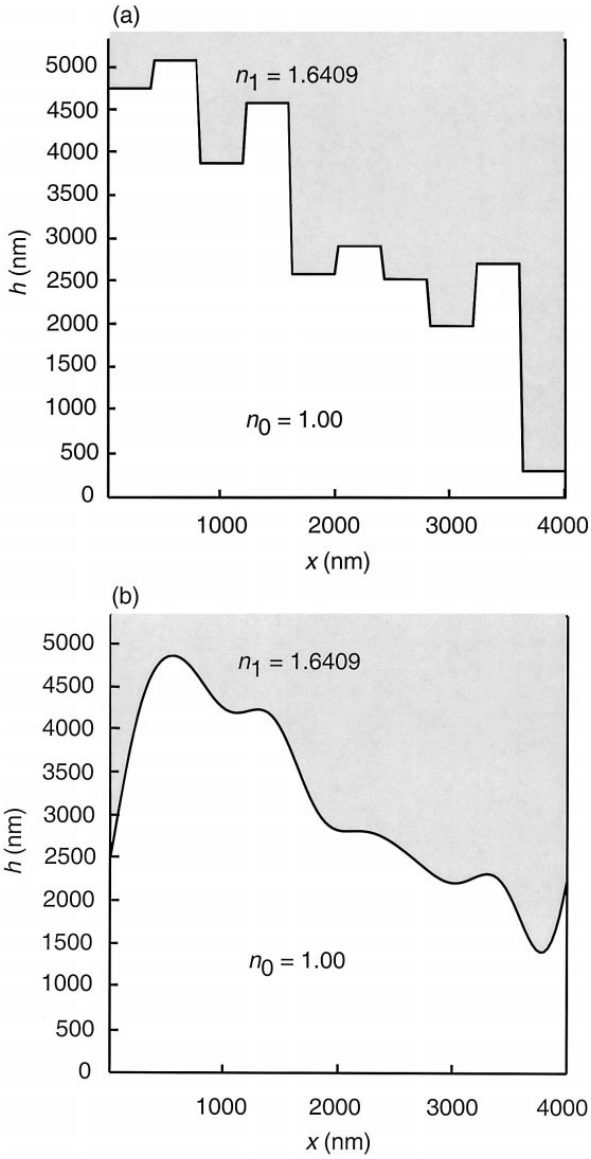

Fig. 4. Optimized blazed grating with period $\Lambda = 4$ μm, designed to work in the $M = 4$th diffraction order. In (a) the discretized profile with 400 nm wide steps, and in (b) the resulting continuous profile after convolution with a Gaussian beam from Eq. (1), using $w = 500$ nm.

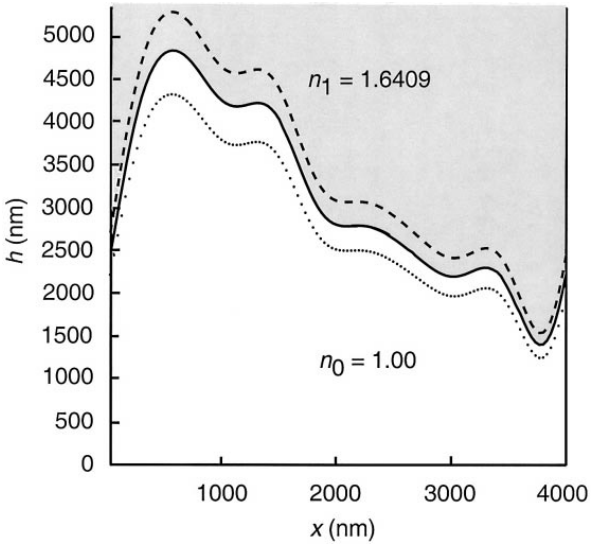

Fig. 5. The continuous line is the same optimized profile as that in Fig. 4(b). Two profiles with erroneous depth scaling are presented with 0.90×optimal depth (dotted) and 1.10×optimal depth (dashed).

$H(0)$, as calculated from the thin element approximation, is not rigorously valid for gratings with $M = 3 - 5$ whose profiles are several wavelengths deep. Secondly, scalar diffraction theory does not take into account the absolute value of Λ, thus ignoring the volume diffraction effects which inevitably arise as Λ gets small. However, even in these cases it is possible to optimize gratings such that they yield $\eta_M > 40\%$. Thus, optimization by utilizing rigorous diffraction theory is not only useful but necessary for high order gratings with a small period, i.e., profiles with high aspect ratios and large diffraction angles. An example of an optimized profile is shown in Fig. 4 where in (a) the optimized discrete depth values $h_{j,\mathrm{opt}}$ and in (b) the convoluted profile, are shown. This figure corresponds to the case $M = 4$ and $\Lambda = 4$ μm in Table 2. The Fig. 2(a) and Fig. 2(b) show the plots for the corresponding non-optimized profile.

Comparing Fig. 2(b) and Fig. 4(b) it is observed that both the depth and the shape of the smoothed profile have changed due to optimization. From Table 2 one observes that the corresponding change in η_4 is from 3.7% to 42.8%. This huge improvement can be understood if we analyze the effect of varying the depth of the profile. Since the wavelength $\lambda = 632.8$ nm, small changes of few hundreds of nanometers to the thin element approximation have a large effect on the diffraction characteristics of the grating.

The effect of depth scaling on the optimized profile is illustrated in Fig. 5. Here the profile from Fig. 4(b) is redrawn together with profiles that are erroneously scaled by the amount of $+10\%$ and -10%. With a high performance laser writing system, the achievable accuracy for the depth of the final profile is approximately 2–5% (see chapter 4 in [2]).

The effect of depth scaling on the values of η_M is calculated for gratings with the depth profile scaled ± 1, ± 5, or $\pm 10\%$ from the optimized value. This yields the results in Table 3 for three combinations of M and Λ. It is seen that in the cases $M = 4$ and $M = 5$, a clear break-down in the diffraction efficiency takes place when the depth of the grating is deviated $\pm 10\%$ from the optimum. In this light, it can be understood that the remarkably improved efficiencies in Table 2 for $M = 4$ and $M = 5$ are not surprising. They are mainly due to finetuning of the depth of the grating from the initial, thin element approximation value. It may be observed from the analysis that in the case of rigorously optimized blazed gratings, it is crucial to make the depth of the profile as close to the optimal as possible. Similar conclusion was drawn by Hessler et al. in Ref. [14] for scalar-optimized gratings. A curious feature in Table 3 is that the results with scaling of -1% are slightly better than the corresponding values in Table

Table 3
Design order efficiencies $\eta_{M,C}$ for smoothed grating profiles whose depth deviates $C = \pm 1\%$, $\pm 5\%$, and $\pm 10\%$ from the optimized profiles. Three cases from Table 2 are covered.

M	Λ (μm)	$\eta_{M,1}$ (%)	$\eta_{M,-1}$ (%)	$\eta_{M,5}$ (%)	$\eta_{M,-5}$ (%)	$\eta_{M,10}$ (%)	$\eta_{M,-10}$ (%)
3	5.2	69.0	69.3	64.0	66.1	51.5	54.7
4	4	41.7	43.1	32.2	35.8	18.1	19.1
5	5.2	46.2	47.9	31.8	38.3	8.4	14.8

2. This is because $R = 81$ retained orders are used to calculate the final diffraction efficiencies, whereas the value of $R = 31$ is used during optimization. Thus, it seems that the optimal solution would be slightly, but not significantly, different if $R = 81$ were used in optimization.

A sensitivity analysis is performed that reflects the error tolerances of the fabrication process. Firstly, the effect of varying the FWHM laser spot size w is analyzed, the results of which are summarized in Table 4 for some of the optimizations. Variation is realized by reconvoluting the optimized discrete profiles $h_{j,\mathrm{opt}}$ with a Gaussian beam shape, Eq. (1), using $w = 650$ nm and $w = 800$ nm. This analysis is necessary because of the practical difficulties in measuring and adjusting the beam size. It is seen in Table 4 that unfortunately the optimizations are fairly sensitive to the value of w which therefore should be experimentally characterized as accurately as possible in order to obtain the best possible results. However, even with the spot size $w = 800$ nm, the resulting diffraction efficiencies into the Mth order are in most cases higher than $\eta_M(0)$.

To further illustrate the sensitivity of optimization process to the spot size some of the optimizations have been redone by using $w = 650$ nm. The results are shown in Table 5. They are seen to be almost the same as those in Table 4. However, these reoptimizations have a slightly better tolerance with respect to the value of $w = 800$ nm than those optimized by using $w = 500$ nm. This observation suggests that the robustness of the solutions could be improved by taking several values of w into account simultaneously during the optimization. This is a topic for future research.

Table 4
Rigorously calculated diffraction efficiencies into the Mth order for three of the cases in Table 2. Here, optimized profiles are convoluted with Gaussian beams [cf. Eq. (1)], using values of w other than in optimization, namely $w = 650$ nm and $w = 800$ nm. The efficiencies are normalized to the total transmittance of the grating.

M	Λ (μm)	$\eta_{M,\mathrm{opt}}$ (%)	η_M ($w = 650$ nm) (%)	η_M ($w = 800$ nm) (%)
3	5.2	**69.2**	57.1	50.4
4	5.2	**53.9**	47.9	39.2
5	5.2	**47.6**	28.8	14.5

Table 5
Rigorously calculated diffraction efficiencies for the same cases as those shown in Table 4, except here the structures have been reoptimized using a Gaussian beam with FWHM $w = 650$ nm in the optimization algorithm.

M	Λ (μm)	η_M ($w = 500$ nm) (%)	$\eta_{M,\mathrm{opt}}$ (%)	η_M ($w = 800$ nm) (%)
3	5.2	59.0	**58.6**	54.7
4	5.2	51.5	**48.4**	40.3
5	5.2	44.2	**33.6**	21.5

5. Conclusions

We have successfully optimized continuous-profile blazed gratings that steer light into the 3rd, 4th, or 5th diffraction order with periods 4, 5.2, or 6 μm. Gratings of this small period possess large diffraction angles and they arise in, e.g., the outer zones of diffractive lenses with a high numerical aperture. These structures represent the state of the art of direct laser beam writing technique and their diffraction characteristics cannot be modeled with the scalar theory but require the utilization of the rigorous diffraction theory.

This is the first time to our knowledge that rigorous diffraction theory has been applied to the optimization of continuous-profile gratings such that the smoothing due to fabrication is taken into account. During the optimization with simulated annealing, the finite size w of Gaussian beam used in fabrication was taken into account with a convolution model. It was seen that for deep gratings working in the 4th and 5th order, diffraction efficiency drops under 10% for non-optimized gratings. This kind of behavioral break-down cannot be predicted with the scalar diffraction theory. With careful optimization it was possible to obtain diffraction efficiencies of over 40% even for the deep gratings with a short period. The effect of depth scaling and variations in the writing beam size were analyzed.

The presented optimization scheme could be straightforwardly applied to other fabrication methods as well, simply by changing the smoothing function.

Other optimization methods, such as gradient descent could be utilized, in particular in the final stages of iteration. Furthermore, the optimized profiles could probably be made less sensitive to the writing spot size w by taking into account several values of w simultaneously in the optimization.

Acknowledgements

Ilkka Kallioniemi acknowledges grants from the Academy of Finland and Suomen Kulttuurirahasto. Discussions with Dr. Eero Noponen on the optimization algorithms for blazed gratings are greatly acknowledged. The authors from CSEM acknowledge the support of the Swiss priority programme OPTIQUE II.

References

[1] H.P. Herzig, Micro-Optics: Elements, Systems and Applications, Taylor and Francis, Bristol, 1997.
[2] J. Turunen, F. Wyrowski, Diffractive Optics for Industrial and Commercial Applications, Akademie Verlag, Berlin, 1997.
[3] M. Hutley, Diffraction Gratings, Academic Press, New York, 1982.
[4] T.J. Suleski, D.C. O'Shea, Appl. Opt. 34 (1995) 7507.
[5] R. Petit (Ed.), Topics in Current Physics: Electromagnetic Theory of Gratings, Springer, Berlin, 1980.
[6] D. Maystre (Ed.), Diffraction Gratings, SPIE Milestone Series MS 83 (1993).
[7] M. Moharam, T. Gaylord, J. Opt. Soc. Am. 71 (1981) 811.
[8] E. Noponen, J. Turunen, A. Vasara, J. Opt. Soc. Am. A 10 (1993) 434.
[9] P. Rai-Choudhury, Microlithography, Micromachining, and Microfabrication, vol. 1, Microlithography, SPIE Press, Bellingham, 1997.
[10] M. Yamagata, Y. Tanaka, T. Sasano, Jpn. J. Appl. Phys. 37 (1998) 3695.
[11] M. Kuittinen, H.P. Herzig, P. Ehbets, Opt. Comm. 120 (1995) 230.
[12] M. Ekberg, F. Nikolajeff, M. Larsson, S. Hård, Appl. Opt. 33 (1994) 103.
[13] F. Nikolajeff, J. Bengtsson, M. Larsson, M. Ekberg. S. Hård, Appl. Opt. 34 (1995) 897.
[14] Th. Hessler, M. Rossi, R.E. Kunz, M.T. Gale, Appl. Opt. 37 (1998) 4069.
[15] J. Goodman, Introduction to Fourier Optics, 2nd ed., McGraw-Hill, San Fransisco, 1996.
[16] S. Kirkpatrick, C.D. Gelatt, M.P. Vecchi, Science 220 (1983) 671.
[17] L. Ingber, J. Math. Comp. Modelling 12 (1989) 967.

Publication II

JOURNAL OF MODERN OPTICS, 2000, VOL. 47, NO. 13, 2281–2293

Diffractive optical elements with modulated zone sizes

THOMAS AMMER and MARKUS ROSSI
CSEM Centre Suisse d'Electronique et de Microtechnique,
Badenerstrasse 569, CH-8048 Zürich, Switzerland

(*Received 2 February 2000*)

Abstract. The standard design for phase-only diffractive optical elements comprises a transformation of the continuous phase function into a surface relief by means of wrapping the phase into regular intervals of $M2\pi$. This results in a structure with diffractive zones aligned in a horizontal plane. We present an alternative design concept with modulated zone sizes leading to non-periodic boundary positions and non-aligned surface structures. The diffractive properties are compared to those of conventional diffractive optical elements. It can be shown that they are fully equivalent for the design wavelength, but exhibit a different spectral behaviour for deviating wavelengths. These properties are exploited for the improvement of the optical performance of blazed gratings and diffractive lenses under conditions of deviating wavelengths. Special emphasis is put on the optimization of the ratio between diffractive efficiencies of the design order and other orders for blazed gratings and focusing diffractive lenses, as well as the suppression of interference effects within Gaussian beams collimated with diffractive lenses.

1. Introduction

The surface relief depth function $d(x)$ of diffractive optical elements such as blazed gratings or diffractive lenses along an axis x is typically calculated using the formalism developed by Sweatt [1, 2] which connects $d(x)$ to the diffractive phase function $\Phi(x)$ by a linear relation. In most cases, the diffraction order M is the only parameter that is standardly used to map the desired phase function into the final surface relief of the diffractive optical element. However, there exist more free parameters for this mapping and consequently there exist a large variety of possibilities for realizing a particular surface relief corresponding to a given phase function $\Phi(x)$. In this fashion, an additional degree of freedom is given to influence the optical properties. In this paper we present a more general approach to address this problem within scalar theory. The calculation of the surface relief function $d(x)$ is derived from $\Phi(x)$ by taking only the most fundamental conditions for the design of diffractive structures into account. The general results can be classified as diffractive elements with modulated zone sizes. For the case of blazed gratings or diffractive lenses this means an irregular arrangement and different sizes of the zones.

In section 2 the physical background of this method will be explained. With the example of blazed gratings some of the basic optical properties are outlined. It will be demonstrated that for the case, where the illumination wavelength perfectly matches the design wavelength and the surface relief profile is realized without

Journal of Modern Optics ISSN 0950–0340 print/ISSN 1362–3044 online
http://www.tandf.co.uk/journals

fabrication tolerances, the performance of a grating with modulated zone sizes is identical to a regular blazed grating. By means of numerical simulations we will investigate in section 3 the properties of these elements when the above conditions are not fulfilled. In section 4 the concept is applied to diffractive lenses. Diffractive lenses used as collimators in optical microsystems are a promising application for this concept of surface relief calculation. Optimization of the individual zone sizes and positions reduces the interference effects of the stray light in this application.

2. Design principle

In a conventional way, the surface relief depth function $d(x)$ of a diffractive optical element is obtained from the phase function $\Phi(x)$ in two steps. First, the design phase function is wrapped to integer multiples M of 2π, leading to a new phase function

$$\Phi_w(x) = \mathrm{mod}\,(\Phi(x); 2\pi M). \tag{1}$$

Then, the surface relief depth function $d(x)$ is derived either by the use of the Sweatt approximation [1]:

$$d(x) = \Phi_w(x)\frac{\lambda_0}{n_1 - n_2}, \tag{2}$$

where n_1 and n_2 are the refractive indices of the ambient and the material, respectively, or by applying more exact methods relating the profile depth with the local period of the diffractive element [3].

For the case of a blazed grating, which is used as a simple model here, the method given by equations (1) and (2) results in a structure, which can be interpreted as a regular arrangement of equally sized and spaced microprisms. The profile step between two neighbouring prisms corresponds to a phase difference of $M2\pi$. An optically equivalent interpretation of this result can be formulated based on phase-sensitive ray-tracing [4]. The microprisms have a blaze angle so that the light is directed in the desired direction according to the law of refraction. In order to get constructive interference of all the wavelets emerging from the individual microprisms in the sense of the Huygens–Fresnel principle, their phase difference has to be an integer multiple M of 2π. In fact, these are the only two essential conditions for the design of the surface relief function of a blazed grating. The periodicity and regularity of a 'regular' blazed grating are more a consequence of the simple formalism given by equations (1) and (2) rather than a strict requirement [5].

Therefore, a blazed grating can be designed as a linear array of microprisms with the blaze angle given by the law of refraction, but having arbitrary sizes. The condition for constructive interference determines the relative position in the vertical direction of the neighbouring prisms. Such a structure can be designed to have no periodicity in the zone positions but nevertheless shows similar diffractive properties as a regular blazed grating. The same design principle can be applied to diffractive lenses as well. We will refer to such structures as blazed gratings and diffractive lenses with modulated zone sizes, respectively.

In order to understand the basic optical properties of blazed gratings with modulated zone sizes we analyse the phase function $\Phi(x) = \Phi_{\mathrm{mod}}(x)$ that can be translated into a corresponding surface relief in analogy to equation (2).

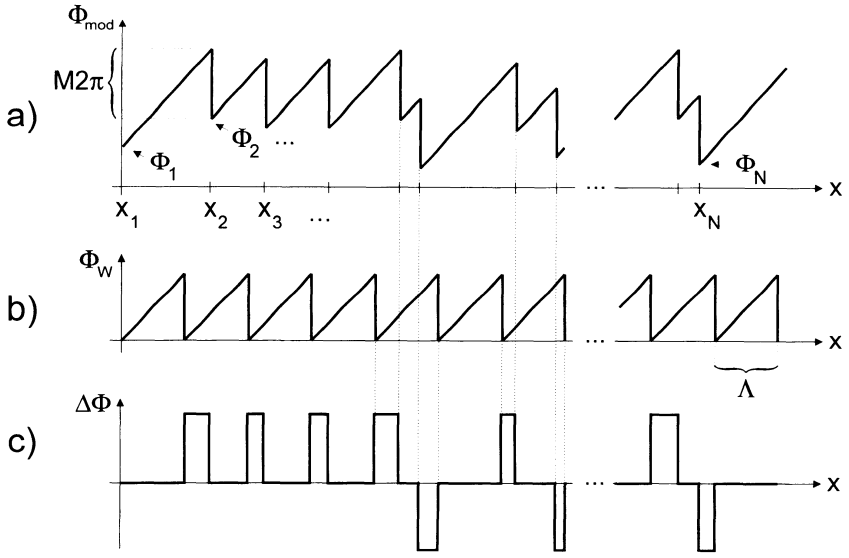

Figure 1. (*a*) Phase function $\Phi_{\mathrm{mod}}(x)$ of a blazed grating with modulated zone sizes, (*b*) phase function $\Phi_{\mathrm{w}}(x)$ of a corresponding regular blazed grating and (*c*) difference $\Delta\Phi(x) = \Phi_{\mathrm{mod}}(x) - \Phi_{\mathrm{w}}(x)$.

Figure 1 (*a*) shows an example of $\Phi_{\mathrm{mod}}(x)$ with N zones, which was constructed by taking the periodic boundary positions of a conventional blazed grating with a period Λ as a basis and varying it by a maximum factor of Δ_Λ. Consequently, the new boundary positions derive from $x_j = \Lambda(j + \epsilon_j \Delta_\Lambda)$, where all $\epsilon_j \in [-1, 1]$ (arbitrarily distributed) and $j = 1, \ldots, N$. The starting phases of each zone are defined recursively as $\Phi_j = \Phi_{j-1} + 2\pi M[(x_j - x_{j-1})/\Lambda - 1]$ with $\Phi_1 =$ arbitrary. In this fashion, all phase steps are equal to $M2\pi$.

We get an initial insight into the optical properties of $\Phi_{\mathrm{mod}}(x)$ when we compare it to the phase function $\Phi_{\mathrm{w}}(x)$ of a regular blazed grating (cf. figure 1 (*b*)) and analyse the difference of the two functions $\Delta\Phi(x)$ (cf. figure 1 (*c*)). It can be seen that all phase steps in $\Delta\Phi(x)$ are equal to $M2\pi$. Therefore, it is evident that adding such a phase function to that of a regular blazed grating will have no effect on its diffraction properties. Hence, in terms of a Fourier-optical diffraction analysis, the blazed grating with modulated zones is equivalent to a periodic one in the case where there are no deviations from the ideal phase functions. However, if the wavelength of the light differs from the design wavelength λ_0, the phase steps in $\Delta\Phi(x)$ will no longer be an integral multiple of 2π and thus give rise to spectral effects which will be discussed in more detail in the following section.

3. Numerical results for blazed gratings

Throughout this paper, we restrict the calculation of the diffracted fields of all diffractive optical elements (DOEs) to cases where scalar theory is applicable. This implies that the smallest local periods are at least one order of magnitude larger than the wavelength of the light [6, 7]. The complex-amplitude transmittance $t(x)$ of the element is based on the thin-element approximation. Consequently, the relation between the field u_0^+ immediately behind the DOE and the field u_0^- incident on the DOE is given by

$$u_0^+(x,0) = u_0^-(x,0)t(x). \tag{3}$$

Since we consider the modulus of $t(x)$ to be unity all over the element (phase-only elements), we can in general describe $t(x)$ in terms of the phase delay $\Phi(x)$ induced by the element:

$$t(x) = \exp\left[\mathrm{i}\alpha\Phi_{\mathrm{mod}}(x)\right]. \tag{4}$$

In order to perform calculations with wavelengths λ other than the design wavelength λ_0, a phase correction factor α, which is generally described as (although we will not consider material dispersion in this paper):

$$\alpha = \frac{\lambda_0}{\lambda}\frac{n(\lambda)-1}{n(\lambda_0)-1}\beta, \tag{5}$$

is introduced. The additional factor β can be used for taking a linear phase error into account, as it manifests itself, e.g. as a depth error after fabrication [8], but will not be discussed further in this paper. We describe the diffractive behaviour of both types of blazed gratings in terms of a Fourier optics approach. Under plane-wave illumination at normal incidence, the efficiency η_k of the kth diffraction order of a grating designed for a wavelength λ_0 and the Mth diffraction order can be directly derived from the Fourier transform of its complex-amplitude transmission function $t(x)$ [9, 10]. In this fashion, the efficiency of the kth diffraction order of a regular blazed grating is given by the well-known relation

$$\eta_k = \mathrm{sinc}^2\,(k - M\alpha). \tag{6}$$

Now we consider a blazed grating with modulated zone boundary positions. The Fourier transformation $T(\xi)$ of the transfer function $t(x)$ of such an element can be written as:

$$T(\xi) = \sum_{j=1}^{N-1} \exp\left[\mathrm{i}\alpha\left(\Phi_j = \frac{2\pi}{\Lambda}Mx_j\right)\right](x_{j+1}-x_j)\exp\left[-\mathrm{i}\pi(x_{j+1}+x_j)\left(\xi - \frac{M\alpha}{\Lambda}\right)\right]$$
$$\times\ \mathrm{sinc}\left[(x_{j+1}-x_j)\left(\xi - \frac{M\alpha}{\Lambda}\right)\right]. \tag{7}$$

The phase delays Φ_j at the beginning of the individual zones are thereby defined recursively as described in section 2 and the normalized efficiency evaluated at a spatial frequency ξ yields

$$\eta_\xi = \left|\frac{\Lambda}{x_N - x_1}T(\xi)\right|^2. \tag{8}$$

Here, the optical behaviour of the grating depends on the size of the individual grating zones. In the case of regular zones sizes ($x_{j+1} - x_j = \Lambda$ for all j), equation (8) reduces to equation (6). If we take $\alpha = 1$, we obtain exactly the same behaviour as for the regular blazed grating. All efficiencies $\eta_{\xi=k/\Lambda} = 0$ for $k \neq M$ and $\eta_{\xi=k/\Lambda} = 1$ for $k = M$. A difference is only observable if the wavelength of the diffracted light differs from λ_0.

The most significant effect is that additional diffraction orders occur at spatial frequencies in between the discrete orders $\xi = k/\Lambda$. The number of these additional orders equals the number of illuminated grating zones and its angular extents are determined by the dimensions of the aperture or the number of

illuminated zones, respectively [11, 12]. Furthermore, mutual overlapping of these additional orders typically leads to an additional 'ground noise'. Figure 2 shows a comparison of the diffraction efficiency spectra for (*a*) a first order periodic blazed grating and (*b*) a zone-size modulated blazed grating at $\alpha = 0.7$, respectively.

The zone sizes of the grating shown here have been optimized using a simulated annealing algorithm. A quality factor γ, described as the ratio of the diffraction efficiencies of the most dominant order $k \neq M$ and the design order $k = M$, served as a figure of merit:

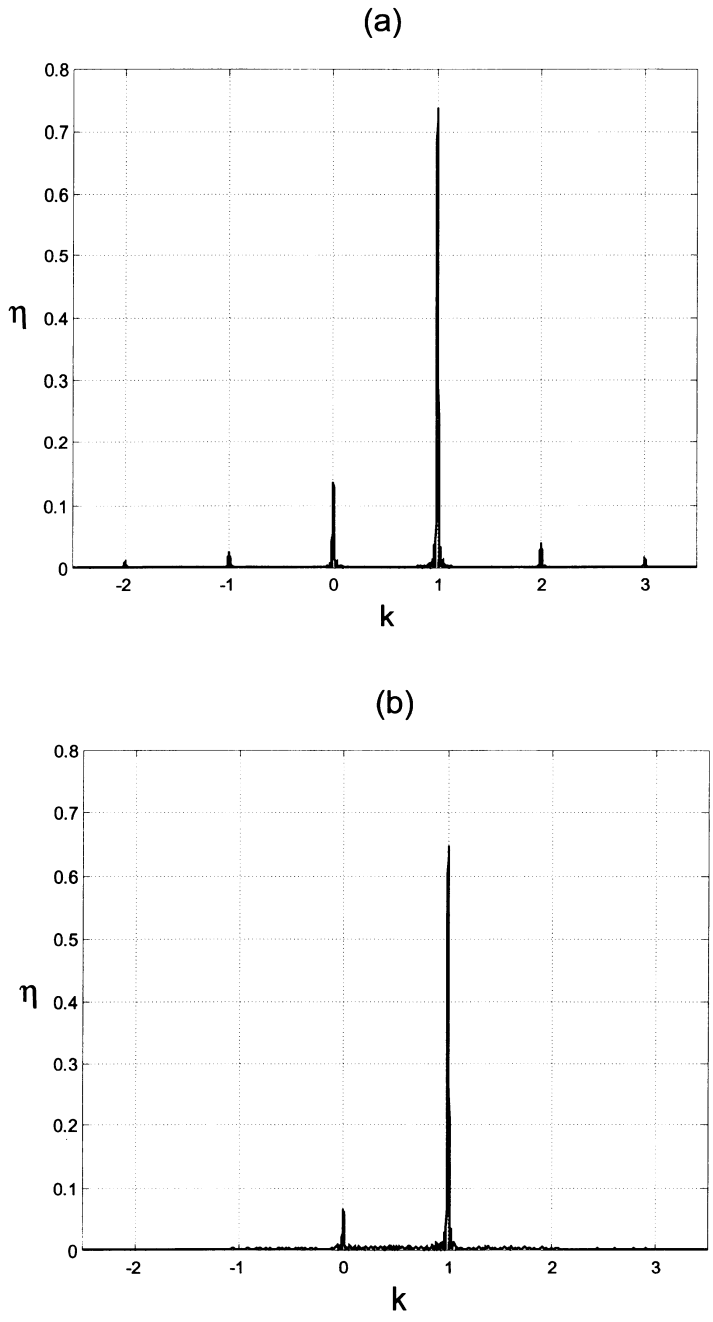

Figure 2. Calculated diffraction efficiency spectra of (*a*) a regular blazed grating and (*b*) an example of an optimized zone-size modulated grating. $\alpha = 0.7$, $M = 1$ and $N = 50$.

Table 1. Comparison of the diffraction efficiencies η_k of orders $k = 0, 1, 2$ and γ values for (a) a first order regular blazed grating and (b) an example of a corresponding γ-optimized zone-size modulated blazed grating.

α	$\eta_{0,a}$	$\eta_{0,b}$	$\eta_{1,a}$	$\eta_{1,b}$	$\eta_{2,a}$	$\eta_{2,b}$	γ_a	γ_b
0.7	0.135	0.064	0.737	0.648	0.039	0.001	0.184	0.099
0.8	0.055	0.020	0.875	0.827	0.024	0.002	0.063	0.024
0.9	0.012	0.003	0.968	0.954	0.008	0.001	0.012	0.003
1.0	0.000	0.000	1.000	1.000	0.000	0.000	0.000	0.000
1.1	0.008	0.001	0.968	0.954	0.012	0.003	0.012	0.003
1.2	0.024	0.002	0.875	0.827	0.055	0.020	0.063	0.024
1.3	0.039	0.001	0.737	0.648	0.135	0.064	0.184	0.099

$$\gamma = \frac{\max(\eta_{k\neq M})}{\eta_{k=M}}. \tag{9}$$

It is well perceptible in figure 2, that the higher diffraction orders could be reduced to the order of the 'average ground noise level' and the quality factor γ could be improved by approximately 50% (cf. table 1).

Figures 3 (a) and (b) show the function $\eta_k(\alpha)$ for $k = 1, 2, 3$ of the above mentioned two gratings. In the case of the regular blazed grating, $\eta_k(\alpha)$ is described by a sinc^2-function (equation 6). This behaviour is no longer valid for a blazed grating with modulated zone boundary positions. Depending on the magnitude of the zone size variations, the efficiency figure deviates from the sinc^2-shape. The primary lobes of the diffraction orders $k = 1, 2, 3$ are getting narrower while the secondary lobes are significantly diminished. Consequently, the occurrence of unwanted orders ($k \neq 1$) for values of $\alpha \neq 1$ is reduced. However, although additional losses of the main diffraction efficiency have to be tolerated, significant improvements of the factor γ can be achieved, as shown in table 1. It is also notable, that the efficiency figure of the first order remains symmetric with respect to $\alpha = 1$.

4. Application to focusing and collimating diffractive lenses

The theoretical analysis of circular symmetric diffractive lenses is similar to the analysis of blazed gratings, as demonstrated in the previous paragraph. The field incident on the element is described in a more general way by an axial symmetric spherical wave with a radius of curvature R_c and a Gaussian amplitude distribution:

$$u_0^+(\rho, \varphi, 0) = \exp\left[-2\left(\frac{\rho}{b}\right)^2\right] \exp\left(\mathrm{i}\frac{\pi}{\lambda R_c}\rho^2\right). \tag{10}$$

Here, b denotes the width of the Gaussian field amplitude distribution in the plane of incidence. The field behind the lens is given by

$$u_0^+(\rho, \varphi, 0) = u_0^-(\rho, \varphi, 0)t(\rho), \tag{11}$$

where ρ denotes the radial and φ the angular coordinate.

The zone boundary locations ρ_p of a conventional Mth order diffractive lens with N zones and a focal length f are determined by [6, 13]

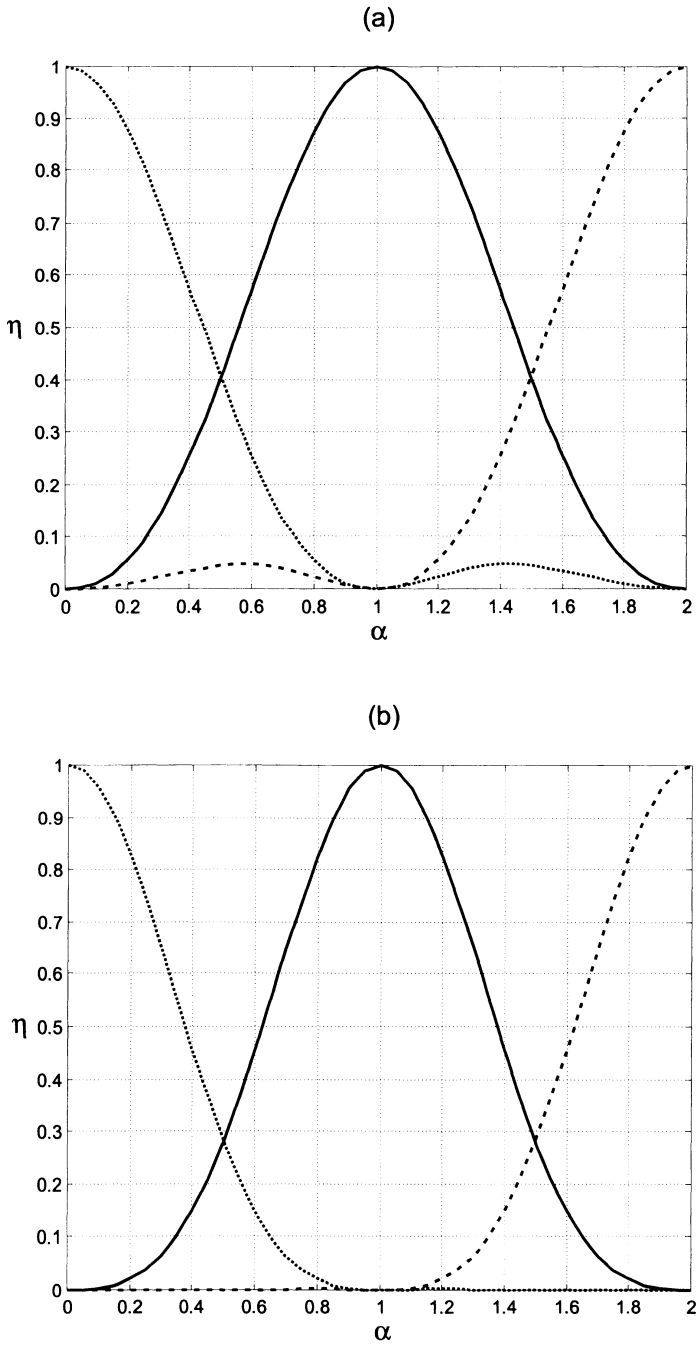

Figure 3. Calculated diffraction efficiencies of (*a*) a regular blazed grating and (*b*) an example of an optimized zone-size modulated blazed grating as a function of α for $k = 0$ (dotted), $k = 1$ (solid) and $k = 2$ (dashed).

$$\rho_p = [2fM\lambda p + (M\lambda p)^2]^{1/2}. \tag{12}$$

Within the pth zone, the phase delay $\Phi_p(\rho)$ introduced to the incident field is

$$\Phi_p(\rho) = \frac{2\pi}{\lambda_0}[f - p - (\rho^2 + f^2)^{1/2}] \text{ for } \rho_p \leqslant \rho < \rho_{p+1}, \quad p = 1, \ldots, N. \tag{13}$$

Hence, the complex amplitude transmittance function $t(\rho)$ of the entire lens within the radius of aperture r_A can be written as

$$t(\rho) = \sum_{p=1}^{N} C_p(\rho) \exp\left[\mathrm{i}\alpha\Phi_p(\rho)\right]; \quad C_p(\rho) = \begin{cases} 1, & \text{for } \rho_p \leqslant \rho < \rho_{p+1}, \\ 0, & \text{elsewhere,} \end{cases} \quad 0 \leqslant \rho < r_A, \tag{14}$$

where α is the phase correction factor given by equation (5). Equations (13) and (14) are also valid if the zone boundaries ρ_p are displaced with respect to the values yielded by equation (12). If we redefine the boundary positions to

$$\rho_p^* = \rho_p + \Delta_\rho \epsilon_\rho (\rho_{p+1} - \rho_p) \quad \text{with} \quad \epsilon_p \in [-1, 1], \tag{15}$$

the new phase delay function for the pth zone can be calculated using equation (13) and the requirement of $M2\pi$ phase steps between neighbouring zones is kept. The factor Δ_p limiting the displacement of the boundary between zones p and $p+1$ to a certain percentage of the size of zone $p+1$ should be chosen such that the conditions for the validity of scalar diffraction theory are fulfilled.

For the propagation of the emanating field, we employ an algorithm for the (zone-wise) direct integration of u_0^+ over the aperture area A using the first Rayleigh–Sommerfeld diffraction formula [10, 14, 15]:

$$u(r, z_2) = \int\int_A u_0^+(\rho, \varphi, 0) \left(\frac{\lambda}{2\pi\delta} - \mathrm{i}\right) \left(\frac{z_2}{\lambda\delta^2}\right) \exp(\mathrm{i}k\delta)\, \mathrm{d}\varphi\, \mathrm{d}\rho,$$
$$\delta = \left[z_2^2 + r^2 + \rho^2 - 2r\rho\cos(\varphi)\right]^{1/2}. \tag{16}$$

r and ρ are the radial coordinates in the observation plane ($z = z_2$) and the aperture plane ($z = 0$), respectively. For faster numerical evaluation, we utilize Gauss–Legendre quadratures [16] for both the integrations along the angular as well as the radial coordinates. Depending on the location of the points of interests, symmetries can be exploited for the reduction of the computational effort.

The diffraction properties of a diffractive lens can be theoretically interpreted in terms of the paraxial approximation as a discrete series of lenses with focal lengths f_k given by

$$f_k = \frac{Mf}{k} \frac{\lambda_0}{\lambda}. \tag{17}$$

Thereby, the energy in a focal point f_k corresponds to the energy diffracted into the kth diffraction order [13, 17]. It is also known that the efficiency of the kth diffraction order η_k is given by the same relation that holds for a regular blazed grating (see equation (6)).

In all cases, the basic design parameters have been chosen as: $\lambda_0 = 0.633\,\mu\mathrm{m}$, $f = 4\,\mathrm{mm}$, $r_\mathrm{A} = 400\,\mu\mathrm{m}$, $M = 1$, $N = 32$. These exemplary data have been chosen as a compromise between a small $F/\#$ number, a sufficient number of zones in order to have enough flexibility for optimization and a minimum feature size to fulfill the requirements for a scalar diffraction approximation.

First, we investigate the on-axis diffractive behaviour of zone-size modulated diffractive lenses under plane wave illumination. Figure 4 compares the on-axis irradiance distribution of (*a*) a conventional and (*b*) a zone-size modulated first order lens, respectively. The former case clearly shows the energy distribution among the focal points (diffraction orders) f_k (cf. equation (17)) which is correlated with the sinc^2-law (equation (6)). The latter gives an example of the suppression of

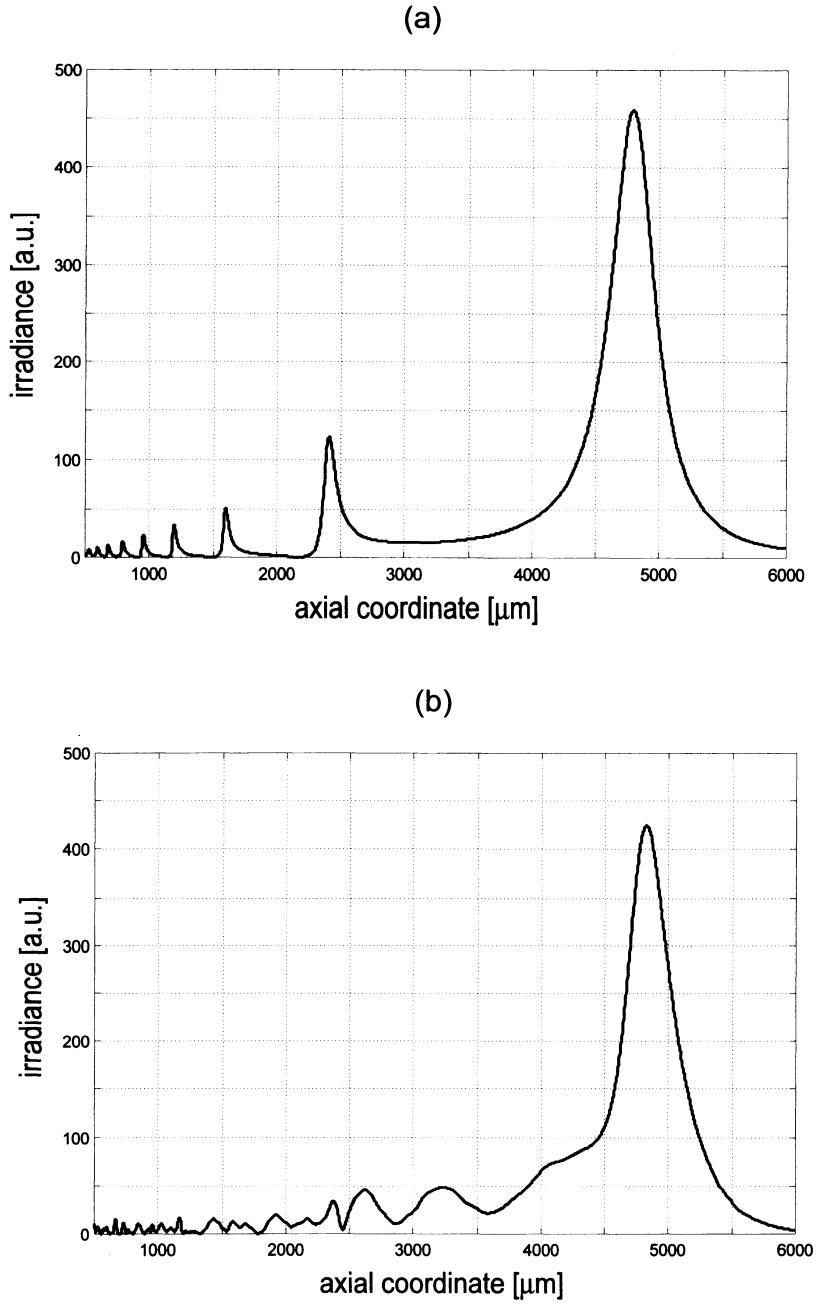

Figure 4. On-axis irradiance distribution of (*a*) a conventional diffractive lens and (*b*) a zone-size optimized diffractive lens illuminated with a plane wave at normal incidence and $\alpha = 0.7$. $\lambda_0 = 633\,\text{nm}$, $f = 4\,\text{mm}$, $r_A = 400\,\mu\text{m}$, $F/\# = 5$.

higher orders in an equivalent fashion as already demonstrated with the zone-size modulated blazed gratings.

This lens has been optimized for a maximum peak intensity at $z = f_1$ while suppressing the higher diffraction orders as much as possible. The optimization has been performed using a simulated annealing algorithm with a merit function σ defined as

$$\sigma = \kappa_0 \eta_M - \sum_{i=1}^{n} \kappa_i \eta_{M+i}. \tag{18}$$

Consequently, maximizing σ leads to a maximization of the amount of light in the design order (represented by η_M) while minimizing the energy in the next n focal points. Introducing an individual weighting factor κ_i for each order allows for putting emphasis on the optimization of one (or more) specific order(s). In the example presented here, the following set of parameters has been used: $n = 4$, $\kappa_0 = 0.5$, $\kappa_1 = 0.7$, $\kappa_2 = 0.5$, $\kappa_3 = 0.4$, $\kappa_4 = 0.3$, $\Delta_p = 0.3$, $\alpha = 0.7$.

Following the definition of equation (9), the quality factor γ of this lens could be improved by a maximum factor of approximately 2. Equivalent to the case of blazed gratings, an improvement of γ for this optimized lens can be observed for values of α within the interval [0.7, 1].

Diffractive lenses with modulated zone sizes can be used to improve the performance of systems for collimating diverging Gaussian beams. It is well known that diffractive collimators are particularly sensitive to wave front aberrations [18]. Light diffracted into higher and lower orders propagates within the 'signal window' (the area of the collimated beam) over much larger distances than is the case for focusing lenses. The interference of the light in higher orders with the light in the design order leads to undesired effects over a large range of propagation [18, 19]. This has to be taken into account for the design of many applications.

As an example, we will investigate the irradiance distribution of a Gaussian beam with $b = 180\,\mu\text{m}$ and $R_c = 4\,\text{mm}$, collimated with a conventional diffractive lens with identical design parameters as described above for the focusing of plane waves. Figure 5 (*a*) illustrates the irradiance distribution for $\alpha = 0.9$ ($\lambda = 700\,\text{nm}$) at a distance $z = 2f$.

It is easily perceptible, that in both cases the actual irradiance pattern (solid line) differs significantly from a (fitted) Gaussian distribution (dashed line). Particularly in the central region, the intensity tends to large oscillations [18] leading to a considerable sensitivity to wavelength deviations.

As a consequence, the usage of diffractive lenses for broadband applications with high beam quality requirements is limited to a very small spectral range. As reported recently by Rossi and Hessler [18], 1% of light distributed among higher orders already results in a normalized uniformity error of approximately 10% (definition given in [18]).

In the following, we will demonstrate the applicability of the zone-size modulation principle on the improvement of the wavelength sensitivity of diffractive collimator lenses. Again, a simulated annealing algorithm has been adapted for the optimization of the irradiance distribution of the collimated beam. As a quality criterion, the mean square error (MSE) of the irradiance distribution with respect to a form function has been chosen. Since a wavelength deviation introduces a field curvature at the exit pupil of the lens, the output beam is either a slightly converging or diverging Gaussian beam. Therefore, we have employed a Gaussian fit to the actual irradiance distribution at the wavelength of interest as a form function for this optimization.

The MSE has been evaluated for two different wavelengths λ_A and λ_B defining a spectral range $[\lambda_A, \lambda_B]$ with $\lambda_A > \lambda_0 > \lambda_B$. For the simulated annealing algorithm, a weighted sum of these two mean square errors, $\text{MSE}(\lambda_A)$ and $\text{MSE}(\lambda_B)$ served as the merit function to be minimized.

During the optimization, the merit function has been evaluated while iteratively changing the positions of the zone boundaries within the predefined

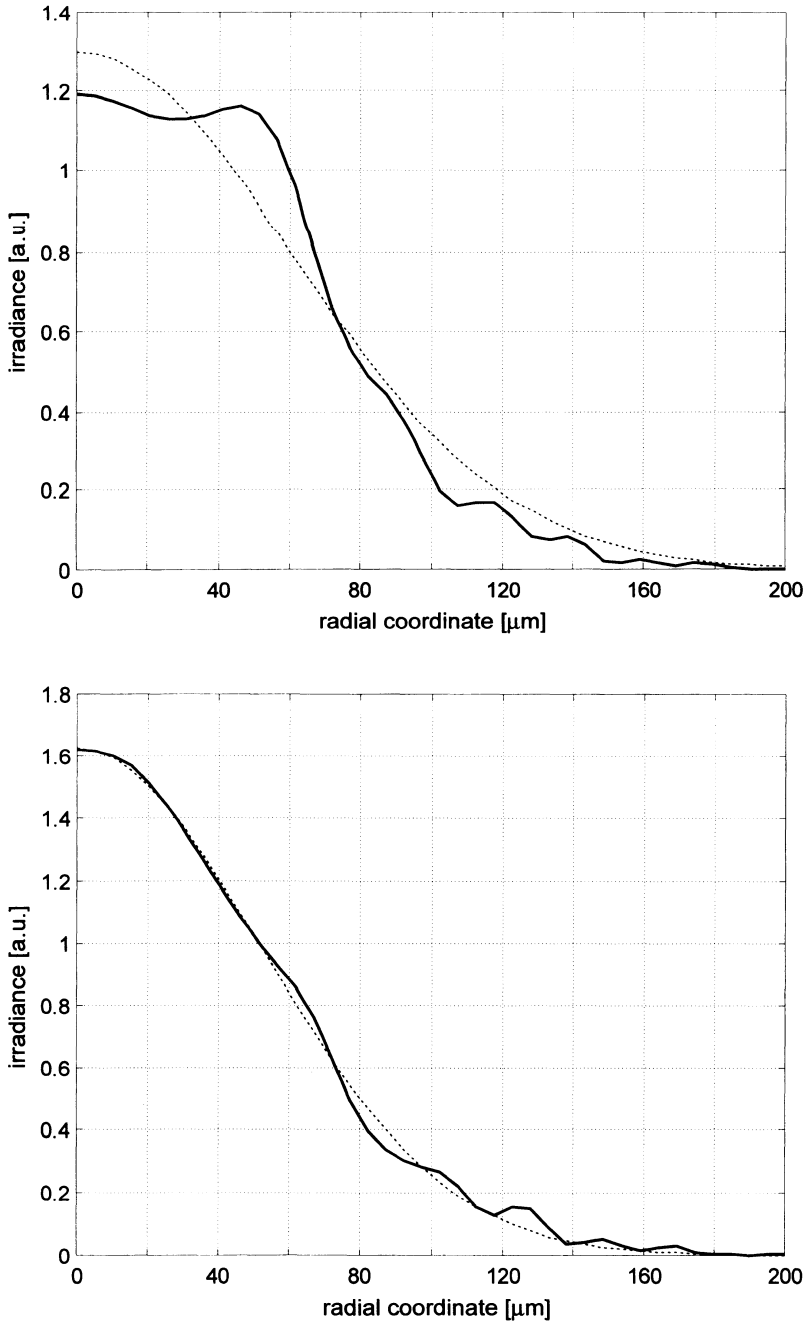

Figure 5. Calculated irradiance distribution at $z = 2f$ of a Gaussian beam with $b = 180\,\mu\text{m}$ collimated with (*a*) a conventional diffractive lens and (*b*) a zone-size optimized diffractive lens. $\lambda = 700\,\text{nm}$, $\lambda_0 = 633\,\text{nm}$, $f = 4\,\text{mm}$, $r_A = 400\,\mu\text{m}$, $F/\# = 5$.

limitations determined by equation (15). In this case we have set this limit to $\Delta_\rho = 0.3$. The spectral range for this optimization has been chosen as $\lambda_A = 575\,\text{nm}$ and $\lambda_B = 700\,\text{nm}$.

Figure 5 shows an example for the irradiance distribution of (*a*) a conventional diffractive lens and (*b*) the result of the optimization at $\lambda = 700\,\text{nm}$. Table 2 compares the numerical results for both types of lenses as a function of the wavelength deviation.

The achieved improvement not only holds for the specific wavelengths λ_A and λ_B. The mean square error is lower for the zone-size modulated diffractive lens

Table 2. Numerical results for the mean square errors (arbitrary units) of (*a*) a conventional and (*b*) a zone-size modulated diffractive lens, optimized for $\lambda_A = 575\,\text{nm}$, $\lambda_B = 700\,\text{nm}$ and $\lambda_0 = 633\,\text{nm}$. $f = 4\,\text{mm}$, $r_A = 400\,\mu\text{m}$, $b = 180\,\mu\text{m}$ and $z_2 = 2f$.

α	$\lambda(nm)$	$MSE(a)$	$MSE(b)$
0.90	700	0.089	0.030
0.95	666	0.048	0.026
0.99	639	0.009	0.005
1.00	633	0.000	0.000
1.01	627	0.010	0.006
1.05	603	0.056	0.031
1.10	575	0.125	0.074

than for a conventional diffractive lens throughout the entire range $[\lambda_A, \lambda_B]$. Table 2 lists a series of examples for different wavelengths (or phase correction factors, respectively). It is evident that this dispersion relaxation is much more significant for wavelengths $\lambda > \lambda_0$, which is due to the steeper gradient of the diffraction efficiency as a function of λ for $\alpha < 1$ than for $\alpha > 1$ (cf. equation (6)).

Hence, when optimizing the zone sizes for a predefined spectral range, it is recommended to choose a design wavelength which is not exactly in the centre of $[\lambda_A, \lambda_B]$. Depending on the design requirements, it is advantageous to choose $\lambda_0 \neq (\lambda_A + \lambda_B)/2$. Note that this statement also holds for the collimation of Gaussian beams with conventional diffractive lenses, although the effect is less significant. In most practical cases, only small wavelength deviations occur. Changes in the order of 1% are realistic for most applications. However, as table 2 shows, such deviations lead already to significant interference effects which can be lowered by approximately 40% by the optimization presented here.

It has been proven that the irradiance distribution of the collimated Gaussian beam is not significantly affected by the zone-boundary position anymore if the field amplitude drops below approximately 10% of the peak amplitude. This is the case for radial positions larger than approximately $1.2b$. Thus, a modulation of the zone sizes in the outer region of the collimating lens is not required. On the other hand, the irradiance distribution is highly sensitive to truncation of the input amplitude on choosing an insufficiently large aperture diameter. If the aperture radius r_A is smaller than approximately $2.2b$, significant aberrations occur especially at the centre of the collimated beam. This aperture effect is a well-known problem in collimating Gaussian beams [20].

These effects impose certain limitations on the choice of parameters for the scalar optimization. In order to obtain a sufficient number of zones within the centre of the lens, a low design order M is preferable.

5. Conclusions

The modulation of individual zone sizes provides an additional degree of freedom for the scalar design of diffractive optical elements. We successfully demonstrated the applicability of this principle to both the design of blazed gratings and diffractive lenses. For blazed gratings and focusing diffractive lenses, the ratio between the 'peak-noise level' and the efficiency of the design order could

be significantly increased. Furthermore, the zone-size modulation proved to be a powerful method for the improvement of the optical performance of diffractive collimator lenses in applications over a certain spectral range. Even wavelength deviations in the order of 1–2% already have a detrimental effect on the quality of a Gaussian beam collimated with a conventional diffractive lens, particularly for short propagation distances. Optimized zone-size modulated diffractive lenses can yield a significant relaxation of the deviation of the irradiance distribution from an ideal Gaussian shape. Consequently, zone-size modulated diffractive lenses provide an alternative for applications where wavelength deviations or propagation distances are critical for the beam quality requirements.

Acknowledgments

We gratefully thank R. Dändliker and H. P. Herzig, both with University of Neuchâtel, Switzerland as well as Th. Hessler, Leister Technologies, Kägiswil, Switzerland for their helpful comments and discussions. This work has been partially funded by the Swiss Priority Program Optique II, whom we thank for their support.

References

[1] Sweatt, W. C., 1979, *J. Opt. Soc. Am.*, **69,** 486.
[2] Herzig, H. P., 1997, *Micro-Optics: Elements, Systems and Applications* (Bristol: Taylor and Francis).
[3] Hessler, Th., 1997, PhD thesis, University of Neuchâtel, Switzerland.
[4] Kunz, R. E., and Rossi, M., 1993, *Optics Commun.*, **97,** 6.
[5] Ammer, Th., and Rossi, M., 1999, *EOS Topical Meet. Digest Ser.*, **22,** 28.
[6] Turunen, J., and Wyrowski, F., 1997, *Diffractive Optics* (Berlin: Akademie Verlag).
[7] Pommet, D. A. Moharam, M. G., and Grann, E. B., 1994, *J. opt. Soc. Am.* A, **11,** 1827.
[8] Rossi, M., Kunz, R. E., and Herzig, H. P., 1995, *Appl. Optics*, **34,** 5996.
[9] Goodman, J. W., 1968, *Introduction to Fourier Optics* (New York: McGraw-Hill).
[10] Gaskill, J. D., 1978, *Linear Systems, Fourier Transforms and Optics* (New York: John Wiley & Sons).
[11] Hessler, Th., and Kunz, R. E., 1997, *J. opt. Soc. Am.* A, **14,** 1599.
[12] Hutley, M. C., 1982, *Diffraction Gratings* (London: Academic Press).
[13] Buralli, D. A., Morris, G. M., and Rogers, J. R., 1989, *Appl. Optics*, **5,** 977.
[14] Stammes, J. J., 1986, *Waves in Focal Regions* (Bristol: Adam Hilger).
[15] Sergienko, N., Stamnes, J. J., Kettunen, V., Kuittinen, M., Turunen, J., Vahimaa, P., and Friberg, A. T., 1999, *J. mod. Optics*, **46,** 65.
[16] Korn, G. A., and Korn, T. M., 1968, *Mathematical Handbook for Scientists and Engineers* (New York: McGraw-Hill).
[17] Dammann, H., 1970, *Optik*, **1,** 95.
[18] Rossi, M., and Hessler, Th., 1999, *Appl. Optics*, **38,** 3068.
[19] Waddie, J. A., and Taghizadeh, M. R., 1999, *Appl. Optics*, **38,** 5915.
[20] Siegman, A. E., 1986, *Lasers* (Mill Valley: University Science Books).

Publication III

Diffractive Optical Elements for Passive Infrared Detectors

M. Rossi, Th. Ammer, M.T. Gale, A. Maciossek and J. Söchtig
CSEM Centre Suisse d'Electronique et de Microtechnique
Badenerstrasse 569, CH-8048 Zurich, Switzerland
Tel. +41 1 4971 640, Fax. +41 1 4971 400, e-mail markus.rossi@csem.ch

C. Ferrari
Polymer Optics, 5 Holland Gardens, GB-Egham, England
Tel. +44 118 9893 341, Fax. +44 1932 566 180, e-mail chris.ferrari@polyopt2.freeserve.co.uk

Abstract: Complex diffractive lens arrays for passive infrared detection systems have been designed and fabricated by laser beam writing and injection moulding. Continuous relief profiles with depths up to 20 μm were originated, characterised and replicated.

OCIS codes: (050.1970, 120.1880)

1. Introduction

Passive infrared detectors for motion detection and intrusion alarms use a complex, multi-element lens array to focus the target field onto an infrared detector and generate an alarm when an object moves across the field. The moving object produces a characteristic time-dependent signal as the images formed by the various lenslets in the array move across the detector.

The lens arrays are mass-produced by injection moulding in infrared (IR) transmissive polyethylene from a complex mould tool. Such moulds have been thus far been typically produced by micro-machining techniques. In this paper we describe the use of Diffractive Optical Elements (DOEs) for this application. Each DOE is an array of diffractive lenslets designed and optimised for a given detector type – Fig. 1 shows a typical array. The fabrication of the original DOE microstructure is done by direct laser writing in photoresist. This allows the fabrication of complex lenslet arrays in a single writing step and opens the door to increased functionality and new detector features. In the example shown here, the lenslet array is optimised for a home detector which can distinguish between persons and pets and generate an alarm only for the former.

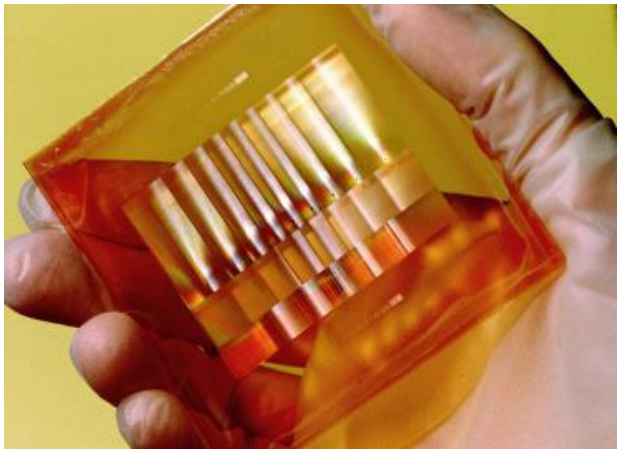

Fig. 1. Lenslet array recorded in photoresist for custom IR detector application.

2. Fabrication: Direct Laser Writing

The polymer lenslet arrays are fabricated using the following steps:
1) Design of lenslets and array
2) Origination by direct laser writing in photoresist
3) Electroforming of an injection moulding tool insert
4) Injection moulding in PE (Polyethylene) for mass-production

The lenslet array shown in Fig. 1 was fabricated using the CSEM LaserWriter system [1] shown schematically in Fig. 2. The individual lenslets were designed as anamorphic diffractive lenses, i.e. having different focal lengths f_x and f_y along the x and y axes.

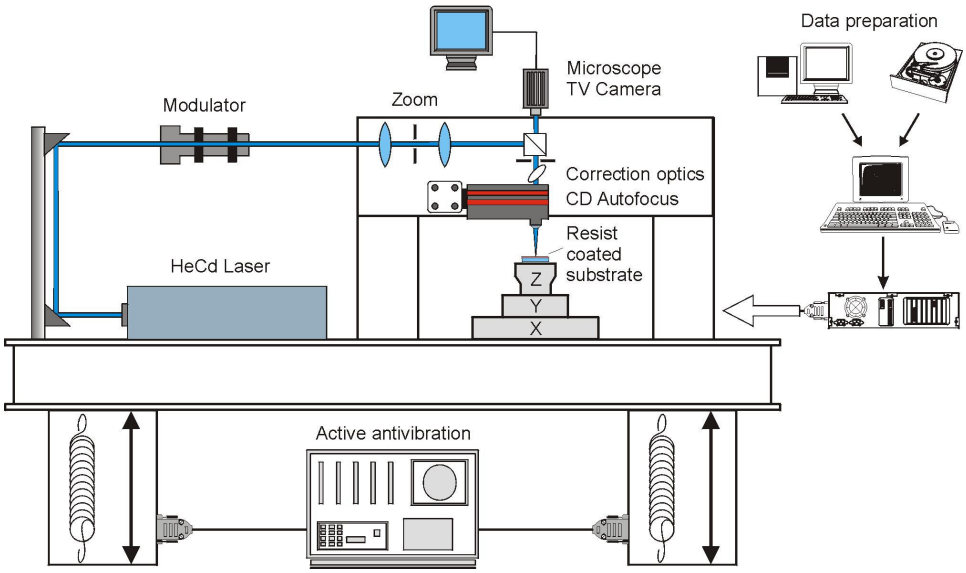

Fig. 2. CSEM`s LaserWriter system for fabricating DOEs by direct laser beam writing

The focal lengths f_x and f_y of each lenses in the array are optimized in order to achieve the required spatial distribution and the signature typical for a human intruder. The horizontal focal length f_x sets the observation range; the values of f_x vary from 10 - 25 mm over the whole array, which typically consists of 20 - 25 individual lenses. By setting f_y to a higher value (typically up to 80 mm) the optical signal of an IR source with a predominantly vertical shape can be increased (= human) compared to a source with a horizontal form (= pet).

Conventional lenses for IR sensor applications are fabricated by diamond machining and are combined to an array by replication techniques. The fabrication with microstructuring technologies such as direct laser beam writing offers several advantages over conventional Fresnel-type lenses:

- For sophisticated spatial detection patterns, different focal lengths can be combined in an array with no additional cost.
- Non-rotationally symmetric elements (including anamorphic lenses) can be fabricated.
- The DOE can be tuned for optimum performance at the wavelength range of interest, 7-14 µm, reducing the false alarm rate by about 15% in practice.
- Due to the reduction in sag when replacing a classical Fresnel element by a diffractive structure, the overall thickness of the element can be reduced, leading to lower absorption and higher signal levels. The mechanical strength of the 500 µm thick injection moulded piece is also significantly improved by the replacement of a classical Fresnel element with about 250 µm maximum depth with the DOE of only a few µm depth.
- Customer specific labelling of the array can be done in the same fabrication step.

The design wavelength was set to $\lambda_0 = 10.0$ µm, considering the typical IR emission spectrum of an object at a temperature of 25 - 30°C and the sensitivity of the pyroelectric detectors. Polyethylene (PE) is a material with good transmission characteristics in the mid IR and excellent suitability for injection molding. The index of refraction at λ_0 is $n \approx 1.51$, leading to a profile depth for a first order diffractive lens of $d \approx 20$ µm. The ability to fabricate deep microstructures by photolithography is thus the key for applying plastic diffractive optics in the infrared wavelength region. Since such continuous-relief profile depths are beyond the limits of standard lithography techniques, special emphasis has to be put on the optimization of film preparation and exposure parameters. The fabrication methods that are currently used at CSEM for diffractive and refractive micro-optical elements in the visible wavelength range were adapted and optimized [2].

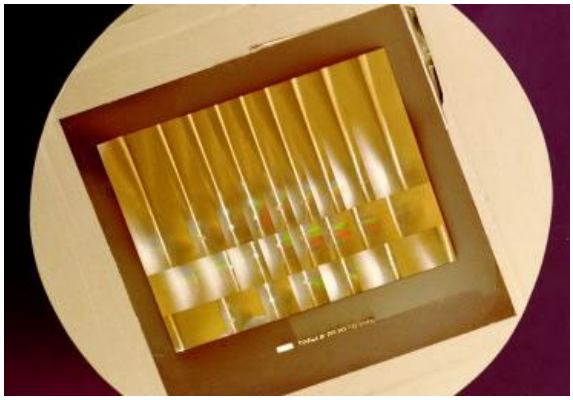

Fig. 3. Ni mould insert electroformed from photoresist original.

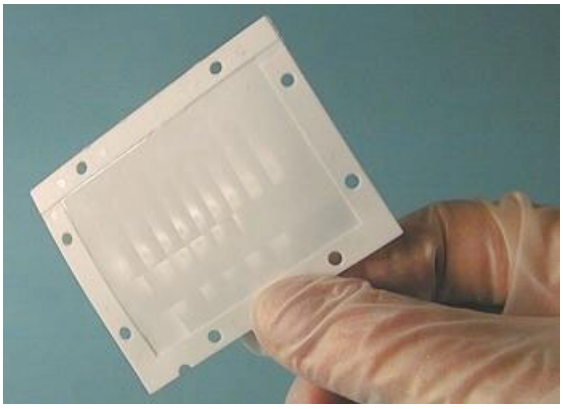

Fig. 4. Injection moulded lenslet arrays in polyethylene.

Films of Shipley S1828 photoresist were spun in a single step to a thickness of 20 μm on glass substrates and exposed in a slightly modified direct laser writing process. Various effects such as the bulk absorption of the photoresist and an increased isotropic component in the development process required additional characterisation runs on test structures. Blazed gratings with different periods and diffractive test lenses were originated by laser beam writing and measured in an IR characterisation set-up.

Following fabrication of the original in photoresist, it is electroformed to a Ni insert tool for the injection moulding [3]. The tool is electroformed to a thickness of 1 mm and polished on the rear side to produce a high quality insert for the moulding. Consistency of the insert tool flatness and thickness are of paramount importance, since the finished component is only 0.5 mm thick and any distortion in the tool will result in a deviation in section thickness of the final moulded component, causing an erratic performance.

The lenslet arrays are moulded in a special polyethylene material for use in the mid IR for these applications. As with all thin section injection moulding care has to be taken to ensure an even fill process to minimise any stress as that would have a detrimental effect on both optical performance and the geometric/mechanical stability of the component. Figs. 3 and 4 show the moulding tool insert and an injection moulded PE lenslet array. Fabricated elements have been tested extensively and show an excellent performance.

3. Conclusions

The use of DOE designs for the lenslet array in Passive Infrared Detectors adds flexibility and new functionality to the system performance. Such elements have been recorded in photoresist using the CSEM LaserWriter and electroformed to a Ni tool insert for injection moulding. Replicas were produced by injection moulding in polyethylene. The resulting DOE lenslet arrays have been successfully tested in Passive IR Detector units and shown to result in improved performance and new features.

The authors gratefully acknowledge the contributions of J.S. Pedersen and other colleagues of CSEM Zurich. This work was supported in part by the Swiss Priority Program OPTIQUE.

References

[1] M.T. Gale and M. Rossi, “Continuous-relief diffractive lenses and microlens arrays”, Ch. 4 in *Diffractive Optics for Industrial and Commercial Applications*, J. Turunen and F. Wyrowski (Eds.), Akademie Verlag, Berlin (1997).

[2] Th. Ammer and M. Rossi, "Replicated diffractive optical elements for IR applications", European Optical Society Topical Digest Meetings Series: Volume **22**, 44-45 (1999).

[3] M.T. Gale, Replication, Ch. 6 in *Micro-Optics : Elements, systems and applications*, H.P. Herzig, Ed., Taylor and Francis, London (1997).

Publication IV

On-chip replication of micro-optical structures for VCSEL to fiber coupling

Thomas Ammer[a], Michael T. Gale[a] and Markus Rossi[b]

[a]CSEM - Centre Suisse d'Electronique et de Microtechnique SA,
Badenerstrasse 569, 8048 Zürich, Switzerland
[b]Heptagon, Badenerstrasse 569, 8048 Zürich, Switzerland

ABSTRACT

We present the design and fabrication of optical microsystems based on UV-replication techniques using Ormocer®* materials. An integration of the optical and mechanical structures on chip level is demonstrated for Vertical Surface Emitting Lasers (VCSEL). VCSEL's are of increasing interest for various fields such as telecommunication, optical sensing and optical interconnects. UV-replication techniques using Ormocer® materials offer a cost-effective way of integrating micro-optical elements directly on the chip with reduced assembly effort. Structures up to several hundred microns thickness and alignment tolerances in the order of few microns can be produced. The method is suitable for the fabrication of single elements, arrays and is extendable to wafer-scale processing. The presented example is a system for the coupling of VCSEL arrays into multimode optical fibers. Two different approaches are followed: Focussing of the VCSEL output into the fiber using replicated microlenses and fiber butt-coupling of the VCSEL lasers with help of replicated fiber alignment/guiding structures. Origination of the structure elements is accomplished by direct laser writing in photoresist and resist reflow techniques, respectively. Specific limitations of the corresponding fabrication method are already taken into account during element design and modelling. Results for the replicated lenses show a total fiber launch efficiency better than 70% over the laser operational range. This performance can be met by passive fiber alignment with tolerances of approximately $\pm 10\mu$m. In case of the replicated fiber alignment / guiding structures, fiber launch efficiencies better than 50% over the operation range and maximum values better than 80% are reported.

Keywords: Micro-Optics, Replication, VCSEL, Fiber-Coupling

1. INTRODUCTION

In recent years, Vertical Cavity Surface Emitting Lasers (VCSEL) have become established devices with increasing importance for various fields of applications. These include datacom, telecom, optical interconnects or optical sensing. Due to their low-cost producibility, efficiency, high-speed tunability and capability to form one- and two-dimensional arrays, they are a preferable light source for many applications. However, the integration into systems (assembly and packaging) still causes time and cost consuming difficulties, which have not been fully addressed yet.

In this paper, we will describe a replication technique based on Ormocer® materials (Organically modified Ceramics), which provides a cost-effective way to integrate micro-optical elements directly on a VCSEL chip. It offers the possibility to integrate micro-optical elements on the surface of single device chips (discrete devices), to produce one- and two-dimensional arrays of micro-optical elements and to integrate elements at wafer-scale level. The latter opens the capability to extend the technique towards low-cost fabrication in large quantities.

For datacom and telecom applications, the high efficient coupling of the output beam into optical fibers is of particular interest. Conventional methods comprise, for example, the manual or automated active alignment of the fiber with subsequent encapsulation (pig-tailing), the use of microprisms in combination with horizontally mounted fiber arrays or ribbons, flexible waveguide structures as interconnecting part between lasers and fiber sockets or the use of sapphire ball lenses. However, all these techniques require time- and cost-consuming alignment and assembly efforts. In this publication, we will demonstrate two different approaches for the coupling of multimode VCSELs into multimode fibers taking advantage of the replication technique mentioned above. The first approach uses diffractive microlenses for the focussing of the beam into a fiber and the second approach describes the replication of special kind of supporting structures with smoothed edges for the alignment and mechanical assembly of the fiber on the chip (pig tailing).

Further author information: Send correspondence to (E-mail) thomas.ammer@csem.ch
Ormocer is a registered Trademark of Fraunhofer Gesellschaft

2. SOURCE CHARACTERISTICS OF THE VCSEL

For all designs and experiments, oxide apertured Vertical Surface Emitting Lasers produced by Avalon Photonics have been used.[1] These were $850nm$ multimode VCSEL's operating in a range between approximately $1mA$ (threshold current) and $12mA$ at an optical power of up to $2mW$. Due to complex effects within the laser cavity, the mode characteristics of the device strongly depends on the driving current.[2] At low currents above threshold, the device operates at the fundamental (TEM_{00}) mode, only. With increasing current, additional linearly polarized modes (LP-modes) appear. The shape and scaling of these higher modes not only influence the near-field intensity distribution at the aperture exit, but have also a strong influence on the far-field angular intensity distribution and the divergence of the laser beam. These properties are decisive for the design aspects and efficiency of fiber coupling lenses, while the tolerancing for the butt-coupling of fibers is mainly determined by the near-field distribution.

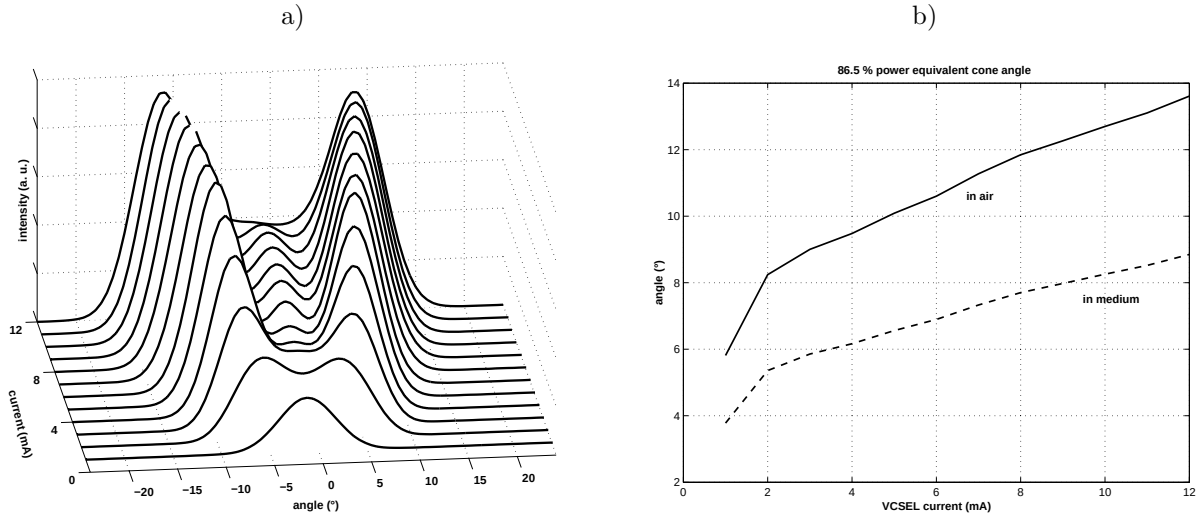

Figure 1. a) Measured angular far-field intensity distribution in free space of a $850nm$ multimode VCSEL as a function of driving current starting from threshold at $1mA$ in steps of $1mA$ to $12mA$ (a). From this data, the divergence half angle θ of the beam within which 86.5% of the emitted power is contained has been derived by radiometric calculations (b) The solid line displays the value of θ for free space propagation and the dashed line corresponds to values of θ in a medium with an refractive index of 1.54 (Ormocer material) .

Measurements of the angular far-field intensity distribution versus the driving current are displayed in Figure 1(a). It is well perceptible that higher modes begin to dominate over the fundamental mode already at currents above approximately $2mA$ and how the divergence of the output beam increases with current. From this measurements, the beam divergence has been calculated by radiometric integration (Figure 1(b)). The divergence half angle θ hereby corresponds to a radiation cone which contains 86.5% of the emitted power. In an operation range between $2mA$ and $12mA$, the dependence of θ on the VCSEL current is almost linear and ranges from approximately 5° to 9° within the Ormocer material ($n = 1.54$).

3. DIFFRACTIVE COUPLING LENSES

We are considering the case of the output beam of the VCSEL to be coupled into a standard multimode optical datacom fiber ($50/125\mu m$) core/cladding diameter with an numerical aperture $NA = 0.20$. The beam is focussed into the fiber core by a diffractive microlens which is directly replicated in Ormocer material on top of the VCSEL chip. Figure 2 shows a schematic cross-sectional drawing of the system setup.

For optimal coupling efficiency, a focussed beam with a numerical aperture smaller than the fiber NA and a spot smaller than the fiber core is required. The design of a diffractive lens for the focussing of the VCSEL beam comprises the translation of the desired optical function into a manufacturable profile (by direct laser writing) under consideration of the restrictions due to the geometrical requirements and the resolution of the manufacturing process. Both aspects will be analyzed in the following two subsections in order to obtain an efficient and fabrication-tolerant design for the coupling system.

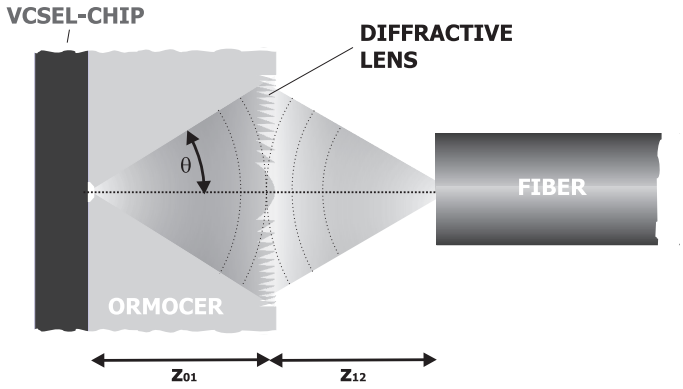

Figure 2. Schematic drawing (cross section) of a VCSEL chip with a diffractive coupling lens replicated in Ormocer material

3.1. Geometrical system design aspects

For the maximum efficiency and the geometrical tolerances of the fiber coupling system, the main parameters are the transversal diameter of the spot at the focal position and the variation of the spot diameter along the propagation axis. Since the exact shape and optical power of each mode is very difficult to determine, a simple model is used for the beam propagation simulations. Taking the divergence data from Figure 1(b), the source beam can be modelled as a Gaussian beam with the same divergence half angle θ (e^{-2} convention). This simplification is justified by the fact that the mode shapes at the exit mirror (aperture) of the laser can be well approximated by a step-index fiber model.[2] Thus, assuming that each mode has the same spacial extent and wavelength, they all have approximately the same divergence and it is sufficient to consider only the propagation of the fundamental (Gaussian) mode in order to model the far-field beam characteristics..[3]

In this fashion, the focal spot diameter (waist) and the Rayleigh range are calculated for a Gaussian mode in Fresnel approximation corresponding to the experimentally derived divergence data presented in Section 2:

Table 1. Gaussian beam propagation parameters for a divergence half angle θ (within the material), vacuum wavelength $\lambda_0 = 850nm$ and a refractive index of the lens material of $n = 1.54$. z_{01} and z_{12} denote the distance VCSEL to lens and lens to fiber-facet, respectively. All values are given in μm

$\theta = 5°$

	waist diameter			**Rayleigh range**		
z_{01}	$z_{12} = 200$	$z_{12} = 300$	$z_{12} = 400$	$z_{12} = 200$	$z_{12} = 300$	$z_{12} = 400$
50	13.4	15.1	15.9	165.2	209.5	233.2
100	11.4	15.9	19.5	119.2	232.5	350.7
200	6.1	9.2	12.1	34.9	77.5	135.6
400	3.1	4.6	6.2	8.9	19.9	35.4

$\theta = 9°$

	waist diameter			**Rayleigh range**		
z_{01}	$z_{12} = 200$	$z_{12} = 300$	$z_{12} = 400$	$z_{12} = 200$	$z_{12} = 300$	$z_{12} = 400$
50	12.4	16.9	20.2	141.8	263.6	378.6
100	6.8	10.2	13.4	43.1	95.3	165.6
200	3.4	5.2	6.9	10.9	24.6	43.7
400	1.7	2.6	3.4	2.7	6.2	11.0

Table 1 list these values for $\theta = 5°$ to $\theta = 9°$ within the Ormocer material ($n = 1.54$), which marks the extremes of the operation range. Values for the waist diameter and Rayleigh range are given for different geometrical lens configurations represented by the distances z_{01} between the VCSEL and the lens and the distance z_{12} between the lens and the focus, respectively. As one can see from Table 1, small distances between the VCSEL and the lens lead

to large waist diameters and large Rayleigh ranges. In this case, the beam is almost collimated. However, for high coupling efficiency and relaxed lateral fiber alignment tolerances, a small spot diameter is required. The longitudinal fiber alignment tolerances can be qualified by the Rayleigh range Z_R. A displacement of the fiber by Z_R with respect to the waist leads to an increase of the Gaussian spot by a factor of $\sqrt{2}$. A longitudinal displacement comparable to Z_R can also lead to an excess of numerical aperture (NA) of the fiber.

Since waist diameter and Z_R are inversely related, a compromise has to be found. There is also a focal shift of the waist with respect to z_{12} associated with small values of z_{01}, but since the Rayleigh range in this cases is in the order of z_{12}, these shifts have only a minor influence on the spot size at the distance z_{12}.

The total focal length of the lens is chosen for optimal focussing of the Gaussian beam at z_{12} when the laser is driven at the center of the operation range. The geometrical dimensions of the coupling system not only determine the caustic of the focussed beam, but also the efficiency of the lens. In the next section, the influence of the geometrical arrangement of the fabrication tolerances of the lens will be discussed.

3.2. Modelling of fabrication specific efficiency effects

The original structures of the diffractive microlenses are fabricated in photoresist by direct laser writing[4] and then replicated directly on top of the VCSEL chip surface. For an estimation of the diffraction efficiency of the lens, we employ a convolution model[5,6] in order to simulate the characteristic effects of the fabrication technique on the shape of the lens profile. Direct laser writing typically produces structures with smoothed profile steps due to the finite size of the writing spot. This smoothing can be accurately simulated by convolution of the design profile with a Gaussian smoothing function. For the following results, a form function with an Gaussian diameter of $1\mu m$ (full width at half maximum) has been chosen.

Thus, the diffraction efficiency of each zone of the diffractive lens can be estimated. In this example, we have used scalar diffraction theory and employed a phase-only thin element approximation to evaluate the local diffraction efficiency of the smoothed lens profile for different geometrical configurations. Taking the intensity distribution of the laser beam in the plane of the lens into account, which is calculated from the measurements shown in section 2, the total diffraction efficiency of the lens can be calculated by integration over the whole aperture area.

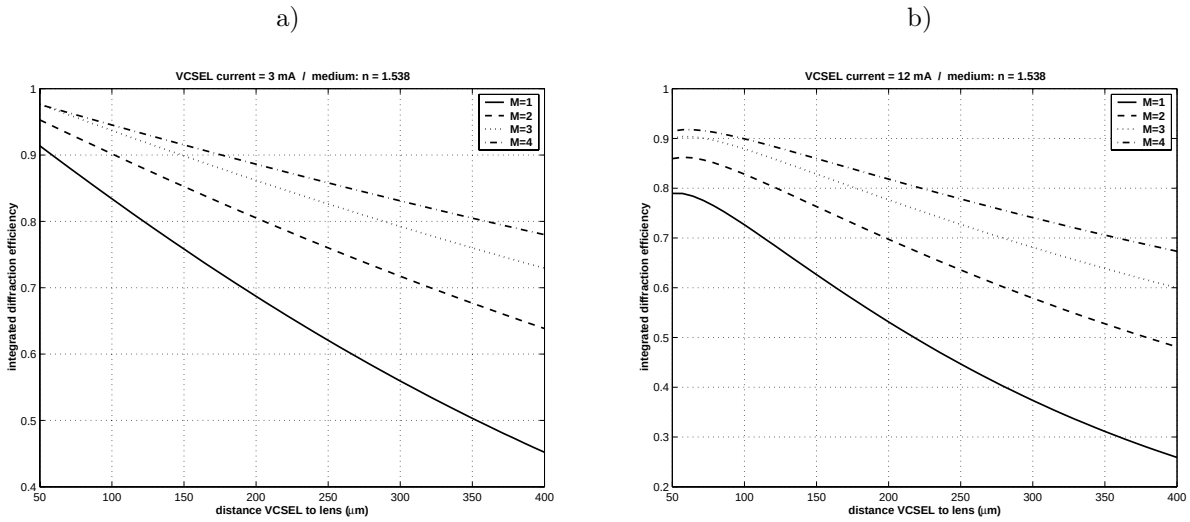

Figure 3. Integrated total diffraction efficency of diffractive lenses with a smoothed profile as a function of the distance between the VCSEL and the lens, designed for $z_{12} = 250\mu m$ and diffraction order $M = 1, 2, 3, 4$ at an operation current of $3mA$ (a) and $12mA$ (b). The diameter of the Gaussian smoothing function is $1\mu m$ (fwhm).

The calculated total diffraction efficiencies as function of z_{01} are shown in Figure 3 for two different operation currents at the lower and the upper end of the operation range, respectively. For the plots, $z_{12} = 250\mu m$ is held constant and z_{01} varied from $50\mu m$ to $400\mu m$. The focal length of the lens is given approximately by $f = (z_{01}^{-1}+z_{12}^{-1})^{-1}$ and the lens aperture diameter is $250\mu m$ in all cases. The different lines correspond to phase matching numbers

(design diffraction orders) of $M = 1, 2, 3, 4$. The figure shows a significant drop of the diffraction efficiency for increasing distance between VCSEL and lens. This can be understood by an increasing diameter of the beam in the lens plane with increasing distance. For this type of high-NA diffractive lenses, the zone sizes or local periods are getting very small at the outer regions of the lens (in the order of $10\mu m$ for a first diffraction order lens profile $M = 1$). This results in a rapidly dropping local diffraction efficiency towards the edge of the lens due to increased smoothing of the zones. The same effect has an increased angle of divergence due to a higher operation current. This explains the difference in the diffraction efficiencies of approximately 10% between Figure 3 (a) and Figure 3 (b).

The figure also illustrates the influence of the chosen design diffraction order M. The diffraction efficiency is significantly better for higher values of M. The reason therefore is that the number of zones is less by a factor of $1/M$ compared to a first diffraction order lens profile for $M > 1$. Thus, there are less zone steps in the profile and the smoothing effect is less dominant. However, values of $M \neq 1$ result in a profile thickness larger by a factor of M, compared to a first diffraction order lens profile. This causes an increase of the effective size of the smoothing function, which again leads to lower diffraction efficiencies. The optimum value for the design diffraction order is in the range of $M = 2..4$.

For optimum fiber launch efficiency and fiber alignment tolerances, a compromise has to be found for the geometrical arrangement. In general, the simulations state that small distances between VCSEL and lens and larger distances between lens and fiber improve the lens performance. Yet, this confronts with the conditions for a small focal spot. An optimized combination depends on the specific application.

Another issue are the requirements imposed by fabrication specific and geometrical limitations. In addition, possible negative effects of light which is diffracted into stray light diffraction orders have to be taken into account.

4. FIBER GUIDING STRUCTURES

We have investigated a different approach for the coupling of a VCSEL source into an optical fiber where the fiber is to be directly attached to the chip (butt-coupled). Therefore, the fabrication of special alignment or guiding structures has been developed. This structures allow the integration directly on the VCSEL chip or wafer by UV-replication. They can be described as circular symmetric grooves with rounded edges at the top surface. Figure 4 illustrates the shape of the guiding structure replicated on top of a VCSEL chip with inserted and encapsulated fibers.

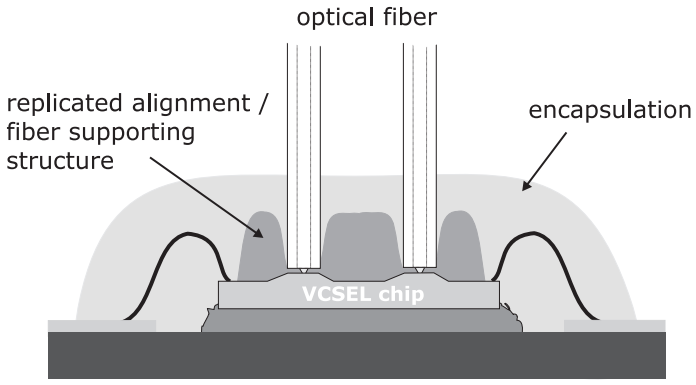

Figure 4. Schematic drawing (cross section) of a VCSEL chip with replicated guiding structures, inserted and encapsulated optical fibers

An original profile of the structure is lithographically produced by thick-film positive photoresist processing with a subsequent thermal reflow of the resist in order to achieve the desired edge profile. The integration on the chip or wafer is carried out by robot-assisted UV-casting replication. The lateral dimension of the near-field intensity distribution just behind the VCSEL aperture is in the order of $10\mu m$. For the robot-assisted replication used for the experiments, lateral alignment tolerances better than $\pm 5\mu m$ and a distance between the laser aperture and the bottom of the alignment grooves smaller than $10\mu m$ can be achieved.

The fiber is attached manually or again robot-assisted by visual pre-alignment using a microscope or imaging system, respectively. After pre-alignment, the fiber is inserted by pushing it into the structure. The rounded conical shape assist the guiding of the fiber and thus a passive alignment. For encapsulation of the system, an optical adhesive, epoxy-material, Ormocer, or other appropriate material can be used.

5. ON-CHIP REPLICATION TECHNIQUE

The replication of the diffractive lens profile as well as the fiber aligment/supporting grooves is done by a UV-casting process using on heteropolysiloxane based materials, in our case Ormocer®[7] . Therefore, a negative silicone cast is first formed from the photoresist original structure as a stamp for later replication. Before casting, the highly viscose Ormocer compound is initially mixed with an appropriate photo-initiator and the deposited on top of the VCSEL chip or wafer.

A precise positioning of the replication stamp with respect to the the wafer is accomplished by a micron-precision cartesian robot. The robot is equipped with an imaging system and distance sensors for sufficient aligment within tolerances smaller than approximately $\pm 10\mu m$ in all three coordinates. After positioning, the material is cured by UV-exposure and the stamp is lift-off. A subsequent thermal annealing of the device at $150 - 200°C$ assures the chemical stabilization and durability of the compound.

In order to adapt this technology to full wafer-scale compatibility, the silicone stamp can be combined with a shadow mask for the selective curing of the UV-material. In this fashion, the problem of sparring out areas for bonding pads and dicing channels can be addressed. Furthermore, additional rods or ridges for the mechanical alignment of other system parts may be implemented next to the actual element.

6. EXPERIMENTAL RESULTS

We present first experimental results for fiber coupling lenses and fiber guiding structures replicated of single device VCSEL chips. For the measurements, a tuneable precision laser current source, an fiber-optical powermeter and xyz-scanning stages have been used in an automated setup.

6.1. Coupling Lenses

Two fourth order ($M = 4$) diffractive lenses designed for distances $z_{01} = 200\mu m$ (lens A) and $z_{01} = 400\mu m$ (lens B), respectively have been characterized. In both cases the designed distance between the lens and the fiber is $z_{12} = 400\mu m$. Figures 5(a) shows the plot of the fiber launch power as a function of the transversal displacement of the fiber from the optimum position for lens A. In Figure 5(b) the absolute fiber coupling efficiency is displayed as a function of the operation current for the same configuration. The different lines in the plots account for different longitudinal displacements of the fiber with respect to designed focal position of $-100\mu m$, $0\mu m$ and $+100\mu m$. Figure 6 is the analogue plot to Figure 5 for lens B.

It can be seen from the figures, that for both lenses coupling losses less than 10% compared to the maximum fiber launch power can be achieved with lateral alignment tolerances of $\pm 10\mu m$. As expected, the coupling efficiency decreases with the VCSEL current, due to the increasing beam divergence (section 3.2). For both lenses the maximum launch efficiencies are almost identical and agree well with the expected values. It is also perceptible that there is a difference in the coupling efficiencies of approximately 15% if the fiber is longitudinally displaced by $100\mu m$ for lens A and approximately 8% for lens B.

However, there are some effects which can not be explained by the simple model of a Gaussian beam. Lens A exhibits a less significant dependence of the coupling efficiency on the VCSEL current than lens B, but shows a stronger dependence on the longitudinal displacement of the fiber. In addition, in both cases the coupling efficiency is better if the fiber is placed closer to the lens than at the designed focal position ($\Delta z < 0$). The main reason therefore is that there is a significant amount of stray-light which is diffracted into diffraction orders other that the designed order. In particular, light that goes into diffraction orders higher than M, will be focussed at intermediate locations between the lens than z_{12}. For a smaller value of z_{01}, These additional focal spots might have a larger longitudinal extent due to the smaller spatial intensity distribution at the lens plane.

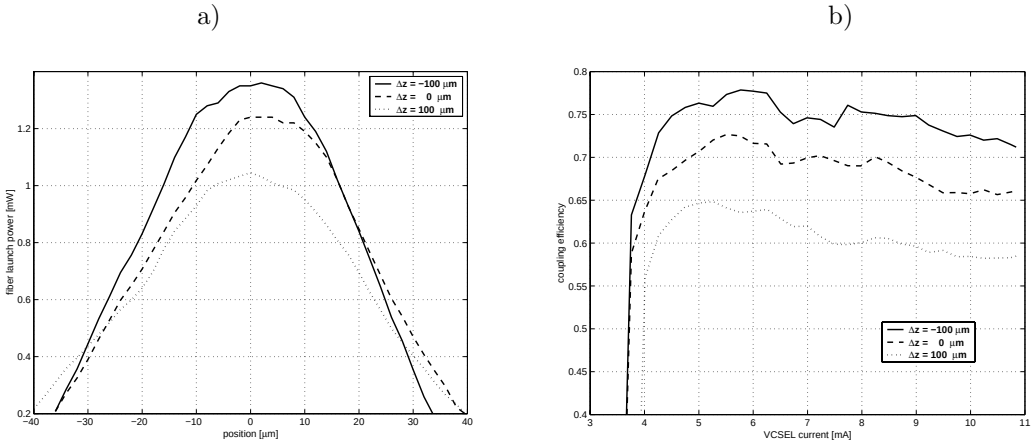

Figure 5. Lens A: Fiber launch power at $I = 10mA$ as a function of the lateral fiber displacement (a) and absolute coupling efficiency as a function of I. $z_{01} = 200\mu m$, $z_{12} = 400\mu m$ and $M = 4$. The different lines refer to a longitudinal displacement Δz of $-100\mu m$ (solid), $0\mu m$ (dashed) and $+100\mu m$ (dotted) of the fiber with respect to the designed focal position.

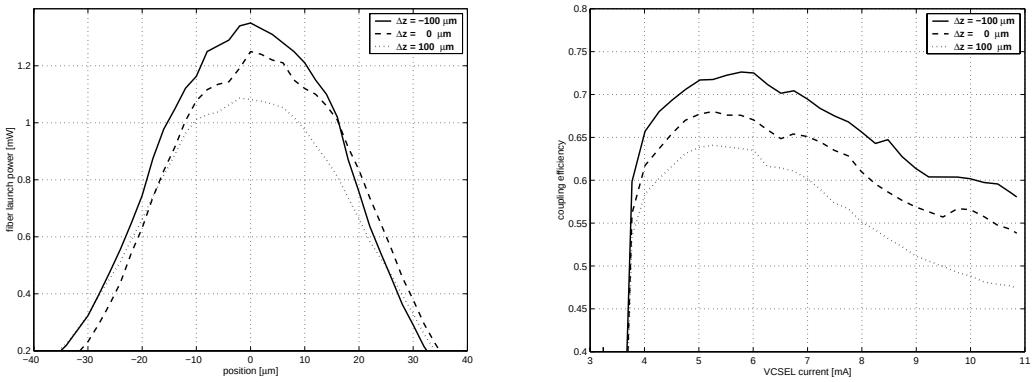

Figure 6. Lens B: Same as Figure 5, but with $z_{01} = 400\mu m$, $z_{12} = 400\mu m$ and $M = 4$.

6.2. Fiber Guiding Structures

We can report the first results for the butt-coupling of multimode VCSEL chips with attached multimode fibers. The fibers have been manually inserted into the Ormocer replicated guiding structure and been encapsulated with an optical UV-adhesive with a refractive index comparable to the refractive indices of the Ormocer and the fiber core. Two VCSELs with a slightly different threshold current have been pigtailed in this fashion and been characterized. In Figure 7, the total fiber coupling efficiency is shown for both VCSELs at different operation currents.

The maximum coupling efficiency ranges between 80% and 90%, which is slightly higher (approximately 5%) compared to the measured maximum coupling efficiency of a fiber butt-coupled to the laser in free-space (without any encapsulation) at a proximity of $5 - 10\mu m$ and the optimum lateral position. Also the almost linear decrease of coupling efficiency with the VCSEL current has the same slope than in the case of free-space butt-coupling.

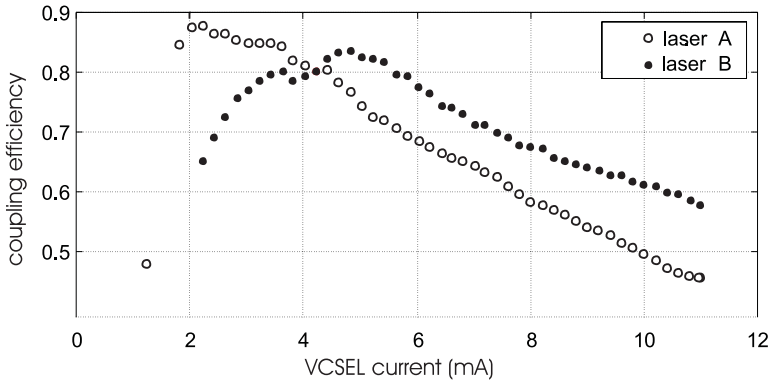

Figure 7. Fiber coupling efficiency of pigtailed VCSELs.

7. CONCLUSIONS

The integration of optical microlenses and fiber guiding structures on single-device VCSEL chips by Ormocer replication has been successfully demonstrated. Coupling efficiencies better than 70% over the whole operation range have been shown for lens coupling. This example also exhibits relaxed alignment tolerances, which can be met by passive alignment. In case of the fiber guiding structures, fiber launch efficiencies could be demonstrated, which are slightly better than for a optimally aligned fee-space butt-coupled device.

Future work on the subject will comprise the further analysis of the beam propagation characteristics under consideration of stray-light effects, further experimental verifications of the design parameters and the extension of the replication technology to VCSEL arrays and wafer-scale processing.

ACKNOWLEDGMENTS

The Authors are particularicly grateful to Dr. Marcel Brunner, Dr. Hans Peter Gauggel and Dr. Stephan Hunziker of Avalon Photonics for their help and support and the supply of VCSELS and measurement data. We also have to thank Prof. Rene Dändliker and Dr. Hans Peter Herzig for helpful discussions.

REFERENCES

1. H. Zappe et. al., "Polarization and noise behaviour of narrow-linewidth 850 nm VCSELs", *Proc. Europ. Conf. on Opt. Comm. (ECOC), Nice*, **Vol. 2**, pp. 308, 1999.
2. M. Brunner, "Design and characterization of single and dual cavity oxide-apertured VCSELs", *PhD-Thesis, École Polytechnique Fédérale de Lausanne*, 2000
3. Siegman, A. E., 1986, "Physical properties of Gaussian beams". in "Lasers" (Mill Valley: University Science Books).
4. Turunen, J. and Wyrowski, F., 1997, "Diffractive Optics" (Berlin: Akademie Verlag).
5. T. Hessler et. al., "Analysis and optimization of fabrication of continous-relief diffractive optical elements", *Appl. Opt.* **33**, pp. 4069, 1998.
6. I. Kallioniemi, T. Ammer , "Optimization of continous-profile blazed gratings using rigorous diffraction theory", *Opt. Comm.* **177**, pp. 24, 2000.
7. G. Blau et. al., "Aspherical microlenses for beam shaping of VCSEL arrays", *Proc. Europ. Conf. on Opt. Comm. (ECOC), Nice*, **Vol. 1**, pp. 350, 1999.

Publication V

Chip-level integrated diffractive optical microlenses for multimode vertical-cavity surface-emitting laser to fiber coupling

Thomas Ammer
Michael T. Gale, MEMBER SPIE
Centre Suisse d'Electronique et de Microtechnique SA
Badenerstrasse 569
8048 Zürich, Switzerland
E-mail: thomas.ammer@csem.ch

Markus Rossi
Heptagon
Badenerstrasse 569
8048 Zürich, Switzerland

Abstract. The standard assembly technologies for vertical-cavity surface-emitting laser (VCSEL) to fiber coupling systems involve the integration of discrete elements with demanding requirements for alignment effort and time. We present a method for the monolithic integration of diffractive microlenses on the chip level. This process is based on a UV-casting replication technique using ORMOCER® (a registered trademark of Fraunhofer-Gesellschaft) materials [hybrid organic-inorganic polymers (Streppel et al. 2001)] and offers the capability to be extended to a wafer-scale process. A mathematical description for the propagation of the laser modes through the system and the resulting fiber coupling efficiency is presented. We use a model for the source characteristics of the VCSEL based on a step-index fiber model for the simulation of the mode-field propagation. A model for the estimation of the diffraction efficiency of the lens is developed. Finally the simulations are compared with first experimental results of single replicated elements. Experimental coupling efficiencies for a multimode fiber [50/125, numerical aperture (NA) = 0.20] better than 0.7 over the entire operation range of the VCSEL are achieved. Losses below 0.5 dB (10%) are observed within lateral fiber displacement tolerances of ± 10 μm. [DOI: 10.1117/1.1518994]

Subject terms: micro-optics; replication; vertical-cavity surface-emitting lasers; fiber coupling.

Paper 010472 received Dec. 21, 2001; revised manuscript received May 14, 2002; accepted for publication May 14, 2002.

1 Introduction

Recent technological developments have shown that vertical-cavity surface-emitting lasers (VCSELs) are gaining increasing importance and have become a preferable choice in many fields of optical communication. They can be produced at low cost, provide efficient operation at high data rates, and offer the capability to form 1-D and 2-D arrays. Multimode VCSELs are widely implemented in transceivers for high-speed, short-range fiber links for fiber channel and gigabit Ethernet in the 850-nm wavelength range. Other applications with increasing interest include optical interconnects for free-space transmission, optical backplanes, and chip-to-chip communication.

For the system integration in datacom and telecom applications, the coupling of the output beams into optical fibers is an issue of particular interest. The majority of the established approaches involve the assembly and alignment (manual or automated) of the VCSELs, the fibers, and micro-optical elements with respect to each other. Some of the most common approaches are sketched in Fig. 1 and include elements such as lenses (refractive or diffractive microlenses,[1,2] ball lenses,[3] graded-index lenses)[4] or interconnecting parts based on flexible waveguides.[5,6]

In this fashion, only single elements or small arrays can be processed at a time and an accurate alignment of all components with respect to each other is required.

In this paper, we describe a technology for the direct integration of diffractive microlenses using a replication technique based on organically modified ceramics (ORMOCER®, a registered trademark of Fraunhofer-Gesellschaft), a hybrid inorganic-organic polymer material.[7] This approach provides a cost-effective way to integrate micro-optical elements directly on a VCSEL chip,[8] as indicated in Fig. 2. It offers the possibility to produce 1-D and 2-D arrays of micro-optical elements.

The main advantage of this method is the possibility to extend the processing to fabrication on a wafer-scale level. This enables the capability for a low-cost fabrication in large quantities. In this paper, we focus only on diffractive microlenses. The process itself is also suitable for the integration of other elements, such as refractive lenslets, gratings, alignment or assembly structures with mechanical functionality, and more complex optical or mechanical subassemblies or microsystems.

The aim of this paper is to describe the steps required for the realization of such a system and to show results for the first practical implementations. To achieve a high coupling performance with relaxed alignment tolerances, it is mandatory to optimize design parameters such as the geometrical configuration and the lens profile. Therefore, we develop a suitable model for the simulation of the optical system, which takes the source characteristics of the laser

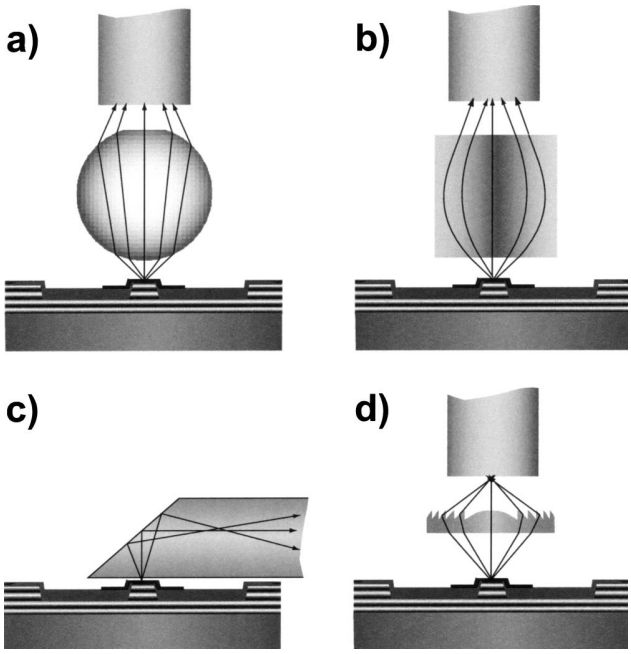

Fig. 1 Schematic drawing of common multimode fiber coupling methods: (a) ball lens, (b) graded-index lens, (c) flexible waveguide with coupling prism, and (d) diffractive lenslet.

as well as fabrication specific aspects of the chosen technologies into account.

The paper is organized as follows. Section 2 describes the beam characteristics of the multimode VCSELs in the near and far fields and the mathematical model used for the source simulation. Section 3 focuses on the modeling and optimization of the diffractive lens and the geometrical arrangement of the system. Finally, in Secs. 4 and 5, the basics of the chosen technological approach and first experimental results are discussed.

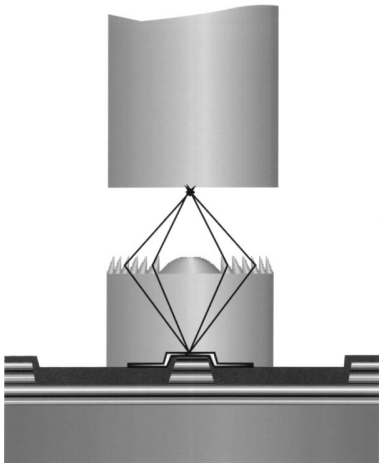

Fig. 2 Schematic illustration of the monolithic chip-level integration of a diffractive microlens.

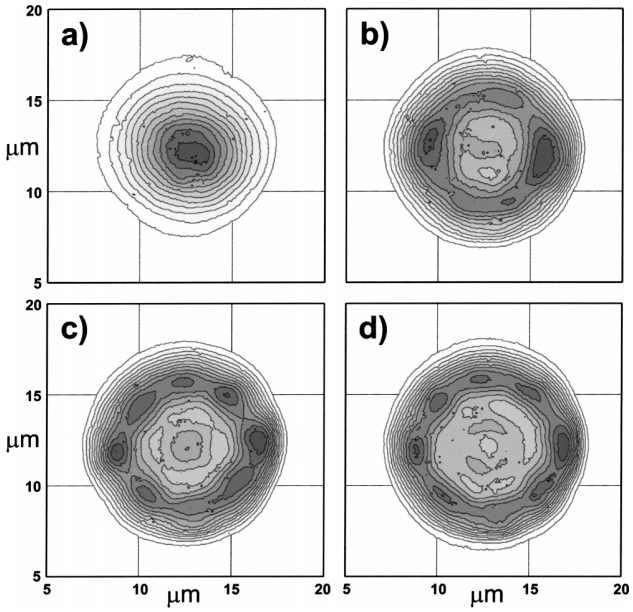

Fig. 3 Contour plots of measured near-field intensity distributions at the exit of the VCSEL aperture for (a) 2-, (b) 4-, (c) 6-, and (d) 8-mA driving currents.

2 Modeling the VCSEL Source

For the work presented in this paper, oxide-confined 850-nm multimode VCSELs produced by Avalon Photonics have been used.[9,10] The lasers have a threshold current of approximately 2 mA and are typically operated between 0.5 and 1.5 mW optical output power, which corresponds to a driving current between 3 and 9 mA. The maximum output power is approximately 2 mW at 15 mA.

2.1 *Mode Characterization in the Near Field*

The transverse mode characteristics of the VCSEL are mainly determined by the structure of the cavity and by the shape and diameter of the oxide aperture, which is located between the active layer and the upper Bragg mirror. The described VCSELs have a circular oxide aperture with a specified diameter of 11 to 12 μm. The near-field intensity distribution was measured by imaging the emission at the VCSEL output onto a CCD camera chip by using a high-quality microscope objective. Figure 3 shows the measured near-field intensity distribution for 2-, 4-, 6-, and 8-mA operation currents.

At low currents above threshold, only the fundamental mode of the cavity is emitting. With increasing current, additional higher order modes appear. It is well perceptible, that the near-field intensity distribution in general is nearly radially symmetric. Qualitative observations while placing a linear polarization filter within the characterization setup show that the shape of the particular modes closely resemble the linear polarized modes (LP modes) of a multimode step-index fiber. It also shows that typically, two orthogonal orientations of individual LP modes with nonzero radial mode index exist with different polarization and carry approximately the same fraction of power. This explains the radial symmetry of the intensity distribution. However, as the driving current of the VCSEL is increased,

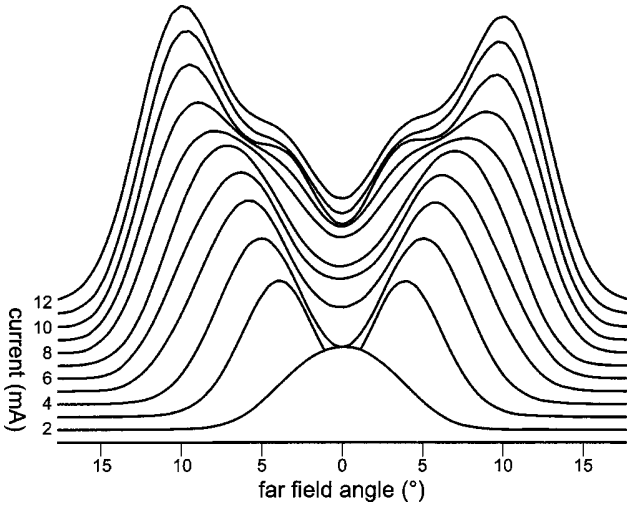

Fig. 4 Measured angular far-field intensity distribution (1-D scan in arbitrary units) in free space for driving currents from 2 mA (front) to 12 mA (back).

the different polarization orientations do not appear exactly at the same point. Thus, the overall polarization state is not constant throughout the operation range and exhibits a complex behavior.[10]

It has been shown that the measured near-field intensity distributions can be very well approximated by LP modes, which correspond to a step-index fiber with a core diameter of 11 μm and an index difference between core and cladding[9] of 0.01. These fitted values are in good agreement with the specification for the oxide aperture diameter and the expected values for the refractive indices. The LP-mode model is discussed in more detail in Sec. 2.3.

2.2 *Angular Far-Field Intensity Distribution*

The circular symmetry of the near field is also present in the far field. Figure 4 shows values of the angular far-field intensity distribution measured in free space. Here, it is also well recognizable that around 2 mA the device operates at its fundamental mode (LP_{01}) only. With increasing current, higher order modes begin to dominate.

Note that the beam divergence depends on the mode distribution, and thus on the driving current. It strongly increases with the current. To obtain a quantitative measure for the beam divergence, the emission angles (in air), which correspond to a circular radiation cone containing a fraction of 86.5% of the total power have been calculated (by radiometric integration). These values are listed in Table 1.

Table 1 also lists the approximated divergence values for propagation within the chosen replication material (ORMOCER®) with a refractive index $n=1.54$ at $\lambda = 850$ nm.

Table 1 Far-field divergence angles θ in degree and the corresponding numerical aperture (NA) for propagation in air ($n=1.00$) and ORMOCER ($n=1.54$). The values correspond to the angle of a radiation cone that contains 86.5% of the total emitted power.

	$n=1.00$		$n=1.54$	
I (mA)	θ (deg)	NA	θ (deg)	NA
2	6.64	0.12	4.31	0.08
3	7.88	0.14	5.12	0.09
4	6.16	0.16	5.95	0.10
6	11.1	0.19	7.21	0.13
8	12.2	0.21	7.92	0.14
10	12.7	0.22	8.25	0.14
12	13.3	0.23	8.60	0.15

2.3 *Modeling the VCSEL Modes*

For a sufficient estimation of the coupling performance of the lens system, an adequate model for the VCSEL source characteristics is required. A rigorous numerical treatment of the complex mode characteristics within the VCSEL cavity is beyond the scope of this work. However, it has been demonstrated, that the transverse mode characteristics of the oxide-confined VCSEL can be well approximated by a step-index fiber model.[9] The refractive index of the insulating Al-oxide layer within the cavity is significantly lower than in the central semiconductor material. Therefore, a mode is laterally confined as it passes through the aperture layer and diffracts after passage. Since the waves propagate periodically back and forth between the two mirrors, this confinement acts like a focusing element. Due to the short propagation length of a few micrometer within the aperture, these periodically guided modes can be approximated by the modes of a uniform step-index waveguide with circular symmetry. The refractive indices for this model can be derived by calculating the mean refractive indices for a vertical round-trip propagation through the region inside the oxide aperture area and outside, respectively.[9] Thus, for this model to represent the VCSEL cavity, these values are taken as the refractive indices of the waveguide core and cladding region and the radius of the oxide aperture is taken for the radius of the waveguide core.

The radial solution of the wave equation for the core and cladding regions of a step-index fiber in cylindrical coordinates are given by[11,12]:

$$u_{lm}(\rho) \propto \begin{cases} J_l(k_t \rho) & \rho \leqslant a \\ J_l(k_t a)/K_l(\gamma a) K_l(\gamma \rho) & \rho > a, \end{cases} \tag{1}$$

where J_l is the l'th order Bessel function of the first kind, K_l is the modified Bessel function of the second kind and order l, and a is the radius of the model fiber core. The parameters k_t and γ are given by

$$k_t^2 = n_1^2 k_0^2 - \beta^2, \quad \gamma^2 = \beta^2 - n_2^2 k_0^2, \quad k_0 = 2\pi/\lambda_0, \tag{2}$$

where λ_0 is the vacuum wavelength; n_1 and n_2 are the refractive indices of the core and the cladding; respectively; and β is the propagation constant of the mode. For guided modes, k_t and γ must satisfy the characteristic equation

$$k_t \frac{J_{l\pm1}(k_t a)}{J_l(k_t a)} = \pm \gamma \frac{K_{l\pm1}(\gamma a)}{K_l(\gamma a)}. \tag{3}$$

In case of a weakly guiding fiber, the guided waves can be approximated as transverse electromagnetic waves (TEM).

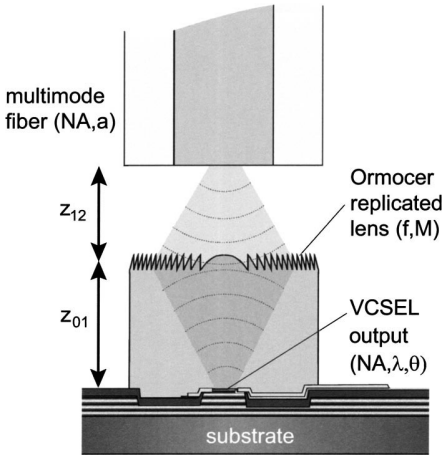

Fig. 5 Schematic drawing (cross section) of the coupling system with a diffractive lens integrated on top of a VCSEL chip, replicated in ORMOCER material.

Thus, the solution for weakly guided waves can be described by a set of linearly polarized (LP_{lm}) modes:

$$u_{lm}^{s}(\rho,\phi)=Au_{lm}(\rho)\cos(l\phi),$$
$$u_{lm}^{p}(\rho,\phi)=Au_{lm}(\rho)\sin(l\phi), \tag{4}$$

where the superscripts *s* and *p* account for two orthogonal orientations of a mode (*l,m*) with amplitude *A* and an azimuthal cosine and sine modulation with the angular coordinate ϕ, respectively.[11]

3 Design and Optimization of the Coupling System

According to the results presented in the previous section, this model of the VCSEL beam characteristics is used as a basis for the simulation of the entire system. Figure 5 schematically illustrates the geometrical setup. The figure shows the diffractive lens, integrated within a block of replicated material on the chip placed at a distance z_{01} from the VCSEL surface. The purpose of the lens is to focus the source beam onto the facet of the fiber located at an axial distance z_{12} from the lens. In case of a VCSEL/fiber array, the maximum diameter of the lens is limited by the pitch of the array (typically 250 μm). However, in terms of compatibility to a wafer-scale process, the lens diameter may also be limited by constraints of the wafer layout (bonding pads, dicing channels). In addition, the divergence or numerical aperture (NA) of the beam, the NA of the fiber and the thickness limitations of the replication process have to be taken into account. Furthermore, application-specific geometrical limitations might be imposed.

Within these constraints, an optimized solution for the geometrical setup is requested. Therefore, the propagation of the source modes through the replication material, the transmission through the lens and the coupling into the multimode fiber must be simulated.

For a phenomenological study of the optimization problem, the simulation was split into two design aspects. Section 3.2 deals with the influence of the geometrical distances and the fiber positioning errors assuming the diffractive lens to be ideal. Section 3.3 then describes the simulation of the lens efficiency for a given geometrical configuration.

3.1 *Field Propagation and Coupling Efficiency Modeling*

The propagation of the scalar mode fields within a homogeneous medium with a refractive index *n* and a wavenumber $k=k_0 n$ from a transverse plane $z=z_a$ to a plane $z=z_b$ is accomplished by the evaluation of the first Rayleigh-Sommerfeld diffraction integral in convolution form[13–15]:

$$u(x,y,z_b)=\mathcal{F}^{-1}\{\mathcal{F}[u(x,y,z_a)]H(\xi_x,\xi_y)\}, \tag{5}$$

$$H(\xi_x,\xi_y)=\begin{cases}\exp[ikz_{ab}(1-\Omega)^{1/2}] & \Omega<1\\ 0 & \text{otherwise,}\end{cases} \tag{6}$$

$$\Omega=\lambda^2(\xi_x^2+\xi_y^2). \tag{7}$$

Here, $\mathcal{F}$ and $\mathcal{F}^{-1}$ denote the forward and inverse Fourier transforms, respectively; $\mathcal{F}[u(x,y,z_a)]$ then represents the plane-wave spectrum of the field $u(x,y,z_a)$ in the transverse plane at $z=z_a$ with spatial frequencies ξ_x and ξ_y; and $H(\xi_x,\xi_y)$ is the transfer function for propagation over the distance $z_{ab}=z_b-z_a$, neglecting evanescent waves.[13] In this manner, the fields are propagated from the source to lens plane and from the lens to the fiber plane, respectively. For simplicity, the phase distribution in the VCSEL plane is assumed to be constant.

Assuming an ideal and infinitely thin diffractive lens element with a focal length *f*, its radial complex amplitude transfer function $\Phi_p(r)$ within the *p*'th zone ($r_{p-1}\leqslant r<r_p$) can be written as[16,17]

$$\Phi_p(r)=\exp\{ik[(r^2+f^2)^{1/2}-f-M\lambda(p-1)]\}. \tag{8}$$

Here, *M* denotes the design diffraction order of the lens. Note that we are regarding a pure phase element with an amplitude transmittance of 1. The position r_p of the outer boundary of the *p*'th zone derives to

$$r_p=[2fM\lambda p+(M\lambda p)^2]^{1/2}. \tag{9}$$

The lens transfer function is applied in real space in the lens plane at a distance z_{01} from the source, according to Fig. 5.

For a rigorous calculation of the coupling efficiency into a multimode fiber with a core radius r_c and a numerical aperture NA_f, the coupling coefficients for each allowed mode in the fiber must be considered. However, since the exact characteristics of the fiber modes are not known, we seek for an approximate solution making the following assumptions.

First, a coupling into the fiber takes place only if the light is incident within the core area. Thus, the fraction of power encircled within the fiber core area compared to the totally emitted power yields a factor η_{core} for the ''spatial'' coupling efficiency.

Second, the incident beam must not exceed the numerical aperture of the fiber. From a ray-optical point of view, this means that rays whose angle with the fiber axis exceeds $\phi_f = \arcsin(\mathrm{NA}_f)$, do not fulfill the condition for total internal reflection. This limitation can be expressed as a cut-off condition in Fourier space. It is equivalent to a spatial filtering of the plane-wave spectrum and derives to:

$$\Omega < \mathrm{NA}_f^2. \tag{10}$$

This condition is accounted for with a second coupling efficiency factor η_{NA}. Thus, the total estimated coupling efficiency derives to $\eta = \eta_{\mathrm{core}}\eta_{\mathrm{NA}}$.

For an efficient numerical evaluation of the above procedures, the algorithm expressed in Eqs. (5)–(7) is implemented taking advantage of fast Fourier transform (FFT) and inverse fast Fourier transform (IFFT) methods.[14]

According to the notation used in Fig. 5, the propagation simulation for the complete system can be outlined as follows:

1. Propagate the source field over distance z_{01} within medium 1.
2. Apply the lens transfer function.
3. Propagate the field emerging from the lens over distance z_{12} within medium 2.
4. Calculate the coupling efficiency.

Due to the orthogonality of the LP modes, this procedure is employed for each individual mode (and mode orientation) separately. To obtain the total field intensity, the propagated modes are incoherently superimposed in the image plane.

3.2 *Design of the System Geometry*

A robust design for the system must consider misalignments due to fabrication tolerances. Therefore, the dependence of the coupling efficiency on misalignments of the fiber needs to be simulated. We do not discuss the effects of the misalignment of the diffractive lens in this publication for the following reasons. First, since the aim is to carry out the replication process on a wafer-scale level (i.e., with a conventional mask aligner), the alignment of the lenses with respect to the wafer can be performed with accuracies of the order of a few micrometers (see Sec. 4). Second, a lateral displacement of the lens does typically not affect the shape of the focal spot (unless aperture effects take place), but causes a proportional lateral shift of the image spot and therefore has a similar effect than a displacement of the fiber.

An issue of particular interest is the behavior of the individual modes of the laser. Based on the LP mode model described in Sec. 2.3, the field propagation through the system is calculated according to the algorithm outlined in Sec. 3.1. For this model, a step-index fiber with a core diameter of 11 μm and an index difference of 0.01 has been chosen. These values yield a very good agreement with the measured near-field intensity distributions. However, since the exact phase in the near field is not known, the resulting far-field divergence is slightly smaller than the measured values (5 to 10%).

To investigate the effect of misalignment on the coupling efficiency separately, we first consider an infinitely thin diffractive lens with an ideal complex amplitude transmittance [Eq. (8)]. The diffraction efficiency of the lens itself will be addressed in the next section.

The observations of the near- and far-field intensity patterns confirm that the distribution of the optical power among individual modes strongly depends on the operation current. Qualitative measurements show that the modes with the highest significance are LP_{01}, LP_{11}, LP_{21}, LP_{31}, LP_{41}, and LP_{12}. With increasing current, more and more energy moves into higher order modes. At 1-mW output power (6 to 8 mA), approximately 50% of the optical power is carried by the modes LP_{31} and LP_{41} and less than 10% by the fundamental mode.

The functionality of the coupling system can be regarded in terms of an imaging system, in which the lens images the output of the VCSEL aperture onto the facet of the fiber. The magnification of the image should be optimized to achieve high coupling efficiencies. We consider a cleaved standard step-index multimode fiber with a core diameter of 50 μm and an NA of 0.20. The paraxial approximation of the magnification factor m for the fundamental mode is given by

$$m \approx \frac{n_1 z_{12}}{n_2 z_{01}}, \tag{11}$$

where n_1 and n_2 are the refractive indices of the medium in front of the lens (replication material) and behind the lens (air), respectively. Since the NA of the VCSEL at high operation currents (10 to 12 nA) is already in the order of 0.14 to 0.15 (NA of the 86.5% power equivalent cone angle within the replication material, cf. Table 1), it is not advisable to chose $m < 1$.

Figure 6 illustrates examples for fiber coupling efficiencies calculated according to the method described in Sec. 3.1. The coupling efficiencies are plotted separately as a function of the lateral displacement of the fiber for the modes LP_{01}, LP_{11}, LP_{31}, and LP_{41} for three different geometrical configurations, given by the distances z_{01} and z_{12}. The focal length of the lens has been chosen as

$$f = \left(\frac{n_1}{z_{01}} + \frac{1}{z_{12}}\right)^{-1}, \tag{12}$$

according to paraxial ray-optical considerations.

Figure 6(a) displays the calculated tolerance curves for $z_{12} = 400$ μm or a magnification $m \approx 3$. We readily see that the coupling efficiency reaches 1.0 within lateral displacement tolerances of the order of 10 μm. The tolerances depend to a low degree on the mode number. The lateral tolerance for the maximum coupling efficiency is significantly smaller than the fiber core radius, due to the large magnification. In this case, the diameter of the image spot is of the order of 50 to 60% of the fiber core diameter, depending on the mode order.

In Fig. 6(b) a case with $m \approx 0.75$ is shown. It is clearly discernible that the lateral tolerances are approaching the dimensions of the fiber core (50 μm diameter), due to the small image spot size. However, since the NA of the beam

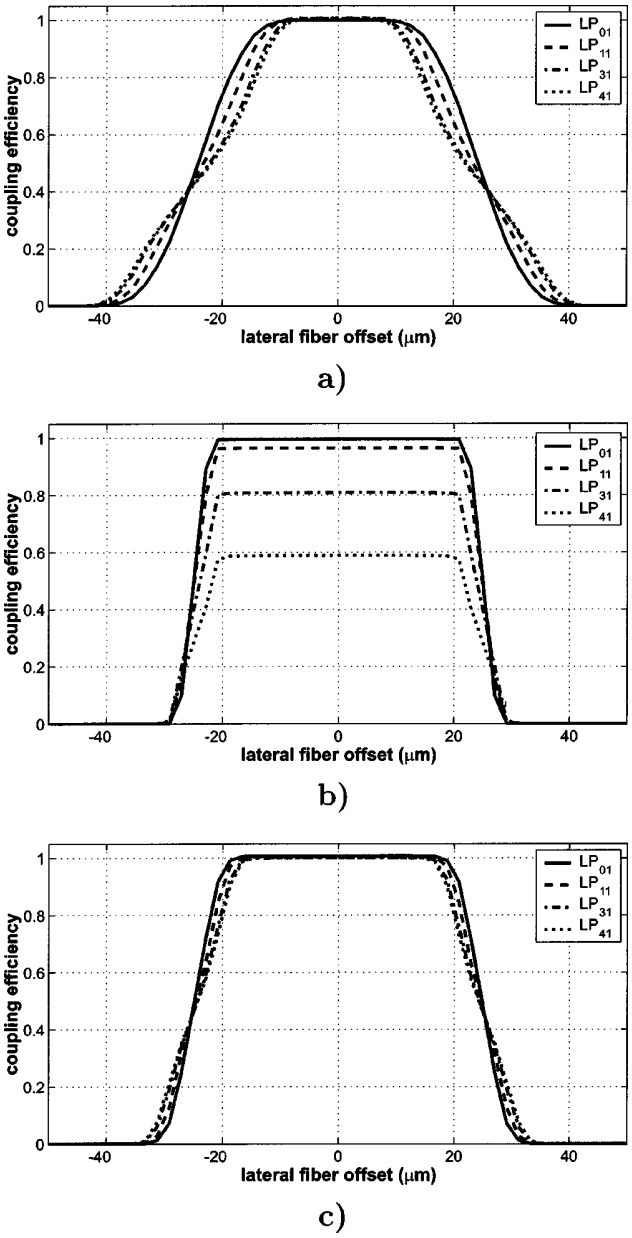

Fig. 6 Calculated coupling efficiencies for different LP modes as a function of the lateral displacement of the fiber. The three plots correspond to different geometrical setups: (a) $z_{12}=400\ \mu$m, (b) $z_{12}=100\ \mu$m, and (c) $z_{12}=200\ \mu$m. For all three cases, $z_{01}=200\ \mu$m.

incident on the fiber increases, the higher order modes partially exceed already the NA of the fiber, which leads to a lower maximal coupling efficiency. The higher order modes have typically an almost ring-shaped far-field intensity distribution. Therefore, a considerable fraction of optical intensity within the lens plane lies outside the acceptance area of the fiber.

Finally, in Fig. 6(c) we consider the distances $z_{01}=z_{12}=200\ \mu$m. This corresponds to a magnification of $m\approx 1.5$, which ensures a smaller NA of the beam emerging from the lens. The imaged spot still fits well into the area of the fiber core and thus the coupling efficiency curves are nearly identical for the indicated modes and reach 1.0 within a lateral displacement range of approximately $\pm 15\ \mu$m.

Table 2 Calculated coupling efficiencies of the modes LP_{01}, LP_{11}, LP_{31}, and LP_{41} for different diffraction orders m of a fourth-order lens for geometrical distances $z_{01}=200\ \mu$m and $z_{12}=400\ \mu$m with values are given for axial fiber displacements $\Delta z=-100$, 0, and $+100\ \mu$m.

m	Δz (μm)	LP_{01}	LP_{11}	LP_{31}	LP_{41}
	−100	0.99	0.87	0.21	0.06
2	0	0.97	0.73	0.10	0.02
	+100	0.92	0.58	0.05	0.01
	−100	1.00	0.99	0.92	0.74
3	0	0.99	0.98	0.87	0.67
	+100	0.99	0.95	0.77	0.57
	−100	1.00	1.00	1.00	1.00
4	0	1.00	1.00	1.00	1.00
	+100	1.00	1.00	0.99	0.98
	−100	1.00	1.00	1.00	1.00
5	0	0.96	0.90	0.71	0.60
	+100	0.86	0.67	0.28	0.14
	−100	0.96	0.88	0.60	0.43
6	0	0.82	0.56	0.08	0.02
	+100	0.66	0.28	0.01	0.01

The latter example represents almost an ideal case for the coupling conditions. All modes are coupled into the fiber with efficiencies reaching 1.0 within fiber displacement tolerances primarily determined by the radius of the fiber core. In terms of imaging properties, this is a very good starting point for an optimized design. The aim for the following part is to implement an element with similar properties and highest possible efficiency.

In the stated examples, the coupling behavior of the individual modes is analyzed under the assumption of an ideal diffractive lens with a diffraction efficiency of 1.0. However, the efficiency of a real fabricated diffractive lens for the focusing of a beam with such a high NA is significantly lower than 1.0 (see Sec. 3.3). The remaining light is distributed among other diffraction orders. A mathematically equivalent description of a diffractive lens is to represent it as infinite series of lenses with different focal lengths.[17] Each diffraction order m of a lens with design order M is associated with a focal length f_m, given by

$$f_m=\frac{Mf}{m}. \tag{13}$$

Using this analogy, the coupling efficiencies associated with an individual diffraction order can be determined by regarding it as a separate ''lens.'' This gives insight to the ''remainder'' of such ''stray-light'' diffraction orders. Tables 2 and 3 list the calculated coupling efficiencies of several modes diffracted into different orders m are for two lenses. The first one with $M=4$, $z_{01}=200\ \mu$m, and $z_{12}=400\ \mu$m and the second with $M=4$, $z_{01}=400\ \mu$m, and $z_{12}=400\ \mu$m. Both designs have been experimentally realized (see Sec. 5).

Table 3 Calculated coupling efficiencies of the modes LP_{01}, LP_{11}, LP_{31}, and LP_{41} for several diffraction orders m of a fourth-order lens with $z_{01}=400\ \mu$m and $z_{12}=400\ \mu$m.

m	LP_{01}	LP_{11}	LP_{31}	LP_{41}
2	0.89	0.48	0.03	0.01
3	0.99	0.98	0.64	0.33
4	1.00	1.00	1.00	1.00
5	0.99	0.96	0.85	0.76
6	0.86	0.48	0.02	0.00

We readily see that for both lenses the coupling behavior strongly depends on the mode number. Almost all power of the fundamental mode is coupled into the fiber for $m=2$ to 6, whereas for higher modes, only the neighboring orders $m=3$ and 5 contribute to a significant coupling. This is due to the fact that the spot size in the fiber plane is larger for $m \neq M$ and the NA can be exceeded (especially for $m<M$). The density of focal points on the optical axis increases with M and decreases with the chosen distance between the lens and the fiber. Thus the lens with $z_{12}=400\ \mu$m (Table 3), exhibits less tolerant efficiency values, compared to the lens with $z_{12}=200\ \mu$m (Table 2).

Additionally, Table 2 shows the effect of an axial displacement of the fiber of $\Delta z=\pm 100\ \mu$m (with respect to its design position) on the coupling efficiencies—with an interesting result: A displacement within this range has only minor consequences for the design diffraction order while the coupling efficiencies for light in other orders can be significantly improved if the fiber is placed closer to the lens ($\Delta z<0$). Particularly the light in the orders $M\pm 1$, which typically are the most significant ''stray-light orders'' of a nonperfect element, can be collected more efficiently. In general, the optimal value for Δz depends on the chosen design order, the geometrical setup and the diffraction characteristics of the lens. If the fiber is placed too close to the lens, the efficiencies can decrease. The same holds generally for $\Delta z>0$.

The coupling behavior of individual modes is not only relevant for the maximum coupling efficiency and misalignment tolerances. It can also affect the properties of the coupling system at high data rate transmission (at gigahertz-rates). In particular, a differential coupling of the modes can cause mode partitioning in the VCSEL. This in turn can give rise to modal noise, which lowers the transmission bandwidth.[18]

3.3 *Diffractive Lens Performance Simulation*

Apart from effects caused by the fiber coupling itself, the system efficiency is determined by the performance of the diffractive lens. The original diffractive surface for subsequent fabrication of a replication mold is generated by a direct laser-writing process in photoresist.[19] Due to the limited resolution of this fabrication method, the shape of the fabricated surface relief differs from the ideal design function. The noninfinitesimal dimensions of the writing spot cause a smoothing of the typical sharp-edged profile steps between the diffractive zones.[20,21] This effect becomes particularly significant at the outer regions of the lens, where the zone sizes decrease with increasing distance from the center. A simple mathematical model can be employed to estimate the resulting overall diffraction efficiency of the lens: The smoothing effect can be mathematically emulated by convolving the ideal profile with an appropriate shape function. This shape function is characteristic to the fabrication method. For the direct laser-writing process used to originate the lenses described in Sec. 5, we have chosen a Gaussian convolution function[22] with a full width at half maximum of 1.5 μm. Note that the convolution method is also applicable to other fabrication processes.[23]

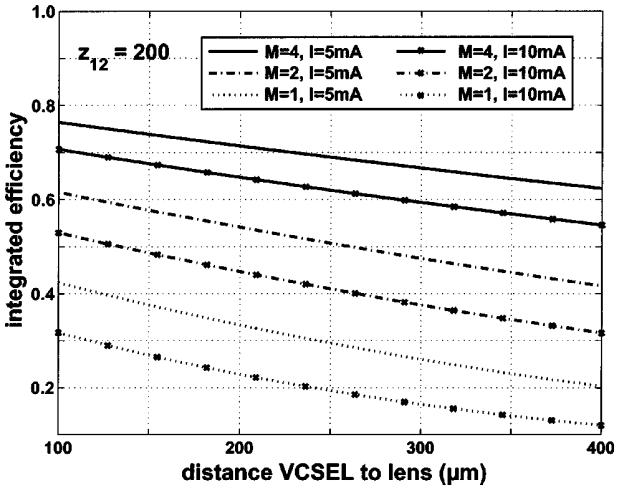

Fig. 7 Diffractive lens integrated total diffraction efficiencies as a function of the distance between the VCSEL and the lens for $z_{12}=200\ \mu$m. The lines correspond to design diffraction orders $M=1$, $M=2$, and $M=4$ for laser operation at 5 mA (unmarked lines) and at 10 mA (marked lines).

In this manner, the diffraction efficiency of the lens as a function of the radial position can be estimated. The lens is treated as a thin phase element and the local diffraction efficiency is calculated using scalar diffraction theory. For the determination of the resulting total diffraction efficiency, the far-field beam characteristics of the VCSEL as shown in Sec. 2 are used. Taking the irradiance distribution in the lens plane (according to the chosen geometry), the fraction of optical power that is diffracted into the design order M can be calculated by integrating over the lens aperture.

Figure 7 summarizes the calculated results for the integrated diffraction efficiency as function of the distance between the VCSEL and the lens for the example of $z_{12}=200\ \mu$m.

Therefore, three different design diffraction orders $M=1$, $M=2$, and $M=4$ were considered. The overall diffraction efficiencies for these orders are plotted for an irradiance distribution in the lens plane, which corresponds to operation currents of the VCSEL of 5 and 10 mA, respectively.

It is clearly discernible, that the efficiency decreases with increasing distance z_{01}, although the focal length of the lens also increases and the NA relaxes. The reason therefore is the fact that for increasing z_{01}, the optical power is more and more concentrated at the outer lens zones with less local diffraction efficiency. The same effect

holds for an increasing operation current, since the divergence of the beam increases. The efficiency drops by approximately 5 to 10% by changing the current from 5 to 10 mA.

Of most significance is the influence of the chosen design order M. As indicated in Fig. 7, the integrated diffraction efficiency for $M=2$, 3, and 4 is drastically higher than for $M=1$. With higher design orders, the number of diffractive zones reduce by a factor of M, compared to $M=1$ and thus, the sizes of the zones increase. Therefore, the smoothing of the zone steps becomes less significant and the efficiency increases. However, not only the zone get larger, but also the relief depth increases. For lenses designed for diffraction order higher than the third order, the smoothing effect becomes more significant (this effect has been neglected in the calculations shown in Fig. 7), because the diameter of the convolution function increases. Thus, the optimum value for M is in the range of 3 to 4.

4 On-Chip Replication Technique

The experiments with the replication of diffractive lens profiles on VCSEL chips were realized by a UV-casting process using[7] inorganic-organic hybrid polymers of type ORMOCER® (organically modified ceramics). After UV curing and a thermal annealing cycle at 150 to 180 °C, the material is typically transparent throughout the visible range and the near IR and becomes a glasslike amorphous composite. The main advantages are its good optical properties, the excellent thermal stability, and durability against moisture along with the fact that it can be well structured and used like a negative photoresist.[7,24] The UV-casting process itself can be outlined as follows.

Starting from the original surface structure produced in positive photoresist (in our case, by direct laser writing),[14,25] a negative silicone mould is formed. This mould is transparent for the UV light and acts as a stamp for the replication. Before casting, the highly viscose ORMOCER® solution is initially mixed with an appropriate photoinitiator and then dispensed on top of the VCSEL chip or wafer.

A precise positioning of the replication stamp with respect to the wafer is required and in our case accomplished by a micrometer-precision Cartesian robot. This robot is equipped with an imaging system and distance sensors for sufficient alignment within tolerances better than $\pm 10\ \mu$m in all three coordinates for ORMOCER® layer thicknesses of 200 to 400 μm. Once the mould is positioned with respect to the substrate or wafer, the material is cross-linked by UV exposure and the mould can then be removed. A subsequent thermal annealing of the device at 150 to 180°C ensures the chemical stabilization and durability of the composit.

To extend this technology to full wafer-scale compatibility, the silicone relief mold can be combined with a lithographic mask for a locally selective cross-linking of the UV material. In the shadowed regions, the remains of noncured material can be removed with appropriate solvents. In doing so, the problem of sparring out areas for bonding pads and channels for chip dicing can be addressed (as indicated in Fig. 5). Furthermore, additional rods or ridges for the mechanical alignment of other system parts may be implemented in the vicinity of the actual element. If the replication process can be done with a mask aligner adapted for this purpose, the positioning tolerances can be further improved. A wafer-scale processing is the key for a production at low cost.

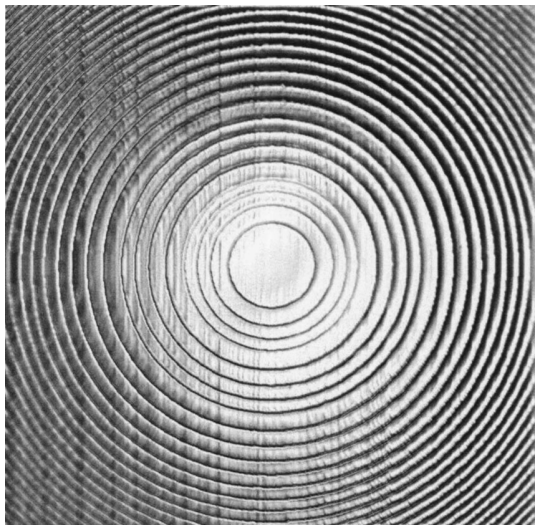

Fig. 8 Example microscope image of a forth-order diffractive lens originated by direct laser writing and replicated by ORMOCER UV casting. The lens area measures $250\times250\ \mu$m and the maximum profile depth is approximately 6 μm.

5 Experimental Results

In this section, we present first experimental results for coupling lenses replicated of single device VCSEL chips. For the measurements of the coupling efficiencies, a tuneable precision laser current source and a fiber optical powermeter were used. The fiber misalignment tolerance curves were determined with three-axis precision scanning stages operated in an automated setup.

Two diffractive lenses designed for the fourth order ($M=4$) were fabricated (an example is shown in Fig. 8). The designed distance between the lens and the fiber for this specific example was required to be $z_{12}=400\ \mu$m. For a comparison with the theoretical results shown in Sec. 3.2, two different distances between the VCSEL and the lens have been chosen: $z_{01}=200\ \mu$m (lens A) and $z_{01}=400\ \mu$m (lens B), respectively. Lens A is equivalent to the underlying design of Fig. 6(a). The imaging properties of lens B correspond to the calculations shown in Fig. 6(c), where $z_{01}=z_{12}=200\ \mu$m (this case is equivalent in terms of the imaging properties). The expected lens diffraction efficiencies for lens A are of the order of 0.6 (see Fig. 7) and for lens B of the order of 0.7.

The characterization results for lens A and B are shown in Figs. 9 and 10, respectively.

In Figs. 9(a) and 10(a), the absolute fiber coupling efficiencies are displayed as a function of the operation current, respectively. Figures 9(b) and 10(b) represent plots of the fiber launch power as a function of the transversal displacement of the fiber from the optimum position for the two samples. In addition, the lateral scans and the current curves are repeated for different axial fiber positions. The solid, dashed, and dotted lines in the plots account for a

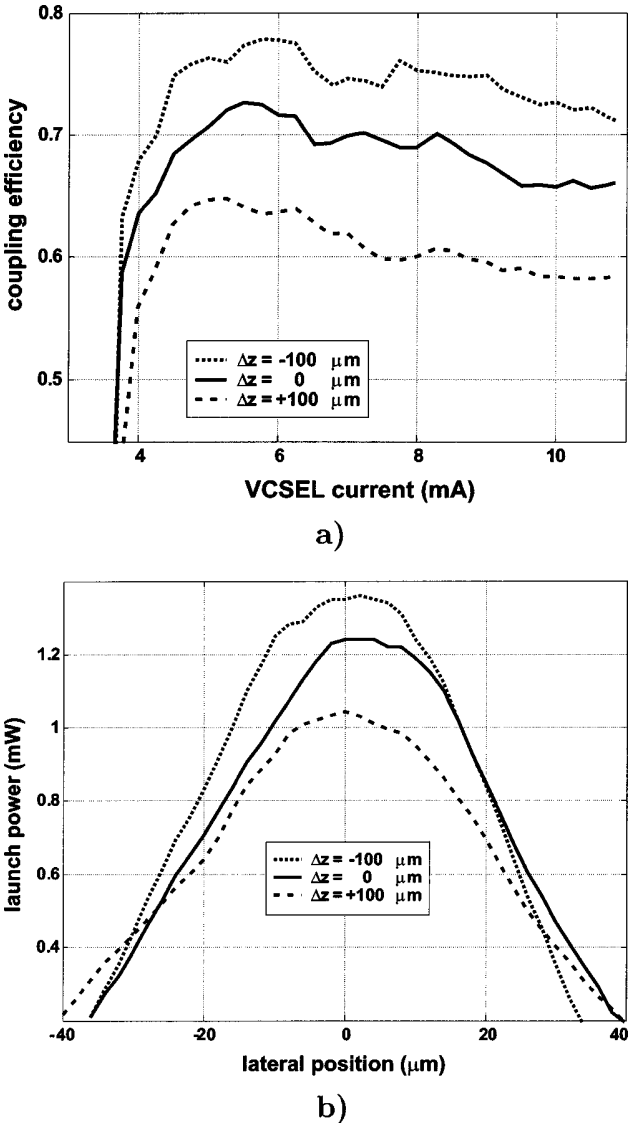

Fig. 9 Lens A: (a) absolute coupling efficiency as a function of the VCSEL current and (b) fiber launch power at $I=10$ mA as a function of the lateral fiber displacement for $z_{01}=200$ μm, $z_{12}=400$ μm, and $M=4$. The different lines refer to a longitudinal displacement $\Delta z = -100$ μm (solid), 0 μm (dashed), and $+100$ μm (dotted) of the fiber with respect to the designed focal position.

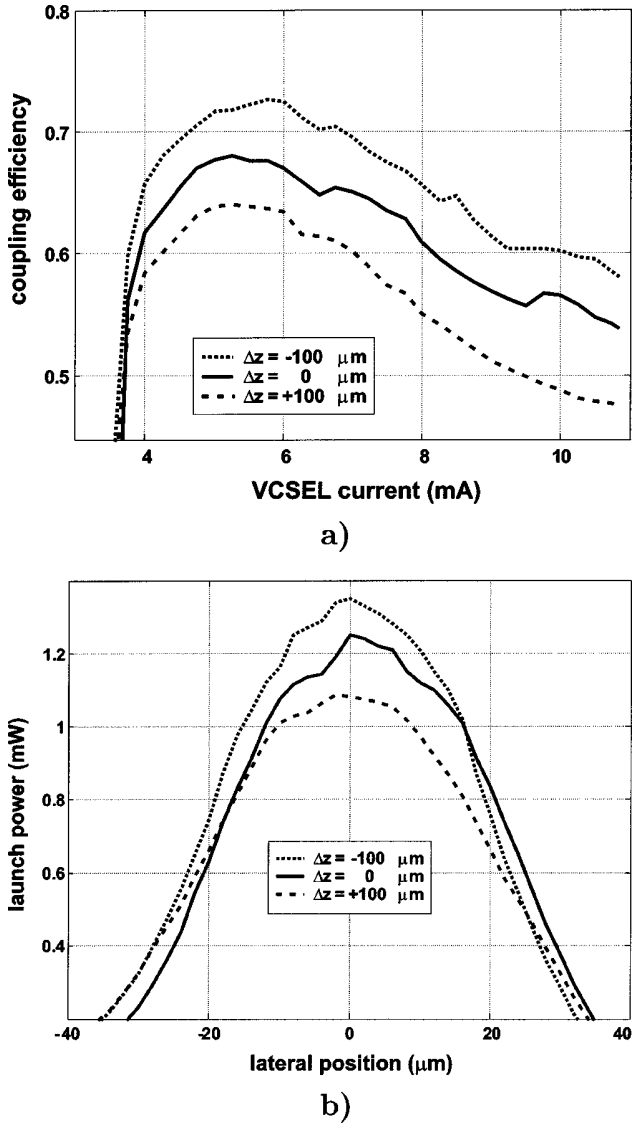

Fig. 10 Lens B: (a) absolute coupling efficiency as a function of the VCSEL current and (b) fiber launch power as a function of the lateral fiber displacement for $I=10$ mA, $z_{01}=400$ μm, $z_{12}=400$ μm, and $M=4$.

longitudinal displacements of $\Delta z = -100$, 0 and $+100$ μm of the fiber with respect to the designed focal position.

The figures confirm that coupling losses less than 0.5 dB (0.1), compared to the maximum fiber launch power can be achieved with lateral alignment tolerances of ± 10 μm. As expected by the calculations presented in Sec. 3.3, the coupling efficiency decreases with the VCSEL current, due to the increasing beam divergence. Both lenses yield similar maximum fiber launch efficiencies. Approximately 30 to 40% of the optical power is distributed among ''stray-light'' diffraction orders, which are also partially coupled into the fiber.

For both lenses, the coupling efficiencies will increase between a factor of 0.05 and 0.1 if the fiber is placed 100 μm closer to the lens from the design focal position. This is another justification for the partial coupling of light from ''stray-light'' diffraction orders and agrees well with the theoretical results summarized in Tables 2 and 3. These results are also a possible explanation for the more significant decrease of the fiber launch efficiency for lens B, since here most of the ''stray-light'' orders are coupled in with lower efficiency. In particular higher order LP modes (which are dominant for high currencies) are coupled less efficient with diffraction orders $m<M$, compared to lens A.

6 Conclusions

The direct replication and integration of diffractive microlenses on VCSEL chips by UV casting with ORMOCER® material is a feasible and promising process. We successfully demonstrated the fabrication of first test samples,

which exhibit a coupling efficiency better than 0.7 over the full operation range of the VCSEL. Losses below 0.5 dB (0.1) of the maximum fiber launch power were achieved with lateral fiber offset tolerances of ± 10 μm. Such tolerances are sufficient for passive fiber alignment in most applications.

On the theoretical side, a mathematical description for the source characteristics of the VCSEL based on a step-index fiber model was adopted. Furthermore, the scalar field propagation of the modes through the system, a model for the diffraction efficiency of the lens, and the estimation of the coupling efficiency of individual modes were presented. In addition, the presented numerical method also enables the investigation of the coupling behavior of ''stray-light'' diffraction orders.

The results of these simulations show a good agreement with the experimental results.

Acknowledgments

The authors are particularicly grateful to Dr. Marcel Brunner, Dr. Stephan Hunziker, Dr. Michael Moser, and Dr. Hans-Peter Gauggel of Avalon Photonics for their constant help and support and the supply of VCSELS, as well as measurement data. We also have to thank Prof. Rene Dändliker and Dr. Hans Peter Herzig of the University of Neuchâtel for their support and helpful discussions.

References

1. G. Nakagawa, K. Miura, M. Makiuchi, and M. Yano, ''Highly efficient coupling between LD array and optical fiber array using Si microlens array,'' *IEEE Photonics Technol. Lett.* **5**, 1056 (1993).
2. M. Rossi, G. L. Bona, and R. E. Kunz, ''Arrays of anamorphic phase-matched Fresnel elements for laser diode-to-fiber coupling,'' *Appl. Opt.* **34**, 2483 (1995).
3. M. Ramos, I. Verrier, J. P. Goure, and P. Mottier, ''Efficient ball lens coupling between a single mode optical fiber and a silica microguide at 1.3 μm,'' *J. Opt. Commun.* **16**, 179–185 (1995).
4. P. Chanclou, M. Thual, J. Lostec, D. Pavy, and M. Gadonna, ''Focusing and coupling properties of collective micro-optics on fiber ribbons,'' *Opt. Eng.* **39**, 387–392 (2000).
5. K. H. Hahn and D. W. Dolfi, ''POLO: A gigabyte/s parallel optical link,'' *SPIE Optoelectronic Interconnects and Packaging*, Vol. CR62, pp. 393–404 (1996).
6. H. Karstensen, F. Auracher, N. Ebel, J. Fiedler, V. Plickert, L. Melchior, L. Leininger, M. Bittner, M. Festag, M. Wicke, S. Meyer, R. Miller, G. Kuhn, H.-L. Althaus, and A. Ebberg, ''Module packaging for high-speed serial and parallel transmission,'' in *Proc. 50th Electronic Components & Technology Conf.*, pp. 479–486, Las Vegas (2000).
7. U. Streppel, C. Dannberg, P. Waechter, A. H. Braeuer, P. Nicole, L. Froehlich, R. Houbertz, and M. Popall, ''Multilayer optical fan-out device composed of stacked monomode waveguides,'' *Proc. SPIE* **4453**, 61–68 (2001).
8. T. Ammer, M. Rossi, and M. T. Gale, ''On-chip replication of micro-optical structures for VCSEL to fiber coupling,'' *Proc. SPIE* **4440**, 238–245 (2001).
9. M. Brunner, ''Design and characterization of single and dual cavity oxide-apertured VCSELs,'' PhD Thesis, Ecole Polytechnique Fédérale de Lausanne, Switzerland (2000).
10. H. P. Zappe, F. Monti di Sopra, H. P. Gauggel, M. Moser, R. Hövel, and K. Gulden, ''Polarization and noise behaviour of narrow-linewidth 850 nm VCSELs,'' in *Proc. Europ. Conf. on Optical Communication (ECOC)*, Vol. 2, p. 308, Nice (1999).
11. D. Marcuse, *Theory of Dielectric Optical Waveguides*, Academic Press, New York (1974).
12. A. Yariv, *Quantum Electronics*, John Wiley & Sons, New York (1988).
13. J. W. Goodman, *Introduction to Fourier Optics*, McGraw-Hill, New York, (1968).
14. N. Delen and B. Hooker, ''Free-space beam propagation between arbitrarily oriented planes based on full diffraction theory: a fast Fourier transform approach,'' *J. Opt. Soc. Am. A* **15**(4), 857–867 (1998).
15. J. D. Gaskill, *Linear Systems, Fourier Transforms and Optics*, John Wiley & Sons, New York (1978).
16. J. Turunen and F. Wyrowski, *Diffractive Optics for Industrial and Commercial Applications*, Akademie Verlag, Berlin (1997).
17. D. A. Buralli and G. M. Morris, ''Optical performance of holographic kinoforms,'' *Appl. Opt.* **28**, 976–983 (1989).
18. D. G. Cunningham, M. C. Novell, P. Dowd, L. Raddatz, and I. H. White, ''Modal noise penalties for data communication links employing large area VCSELs,'' *Electron. Lett.* **31**, 2147–2148 (1995).
19. M. T. Gale, M. Rossi, J. S. Pedersen, and H. Schütz, ''Fabrication of continuous-relief micro-optical elements by direct laser writing in photoresist,'' *Opt. Eng.* **33**, 3556–3566 (1994).
20. M. Ekberg, F. Nikolajeff, M. Larsson, and S. Hård, ''Proximity-compensated blazed transmission grating manufacture with direct-writing electron lithography,'' *Appl. Opt.* **33**, 103–107 (1994).
21. F. Nikolajeff, J. Bengtsson, M. Larsson, M. Ekberg, and S. Hård, ''Measuring and modelling the proximity effect in direct write electron-beam lithography kinoforms,'' *Appl. Opt.* **34**, 897–903 (1995).
22. T. Hessler, M. Rossi, R. E. Kunz, and M. T. Gale, ''Analysis and optimization of fabrication of continuous-relief diffractive optical elements,'' *Appl. Opt.* **37**(19), 4069–4079 (1998).
23. I. Kallioniemi, T. Ammer, and M. Rossi, ''Optimization of continuous-profile blazed gratings using rigorous diffraction theory,'' *Opt. Commun.* **177**, 15–24 (2000).
24. G. Blau, M. Rossi, T. Ammer, M. T. Gale, H. P. Gauggel, and K. Gulden, ''Aspherical microlenses for beam shaping of VCSEL arrays,'' in *Proc. Eur. Conf. on Optical Communication* (ECOC), Vol. 1, p. 350, Nice (1999).
25. H. P. Herzig, *Micro-Optics: Elements, Systems and Applications*, Bristol, Taylor and Francis (1997).

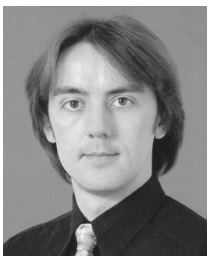

Thomas Ammer received his engineering degree in microsystems technologies from the University of Applied Sciences, Regensburg, Germany. He is currently carrying out his PhD studies at the Centre Suisse d'Electronique et de Microtechnique—CSEM, Zurich, Switzerland, in cooperation with the University of Neuchâtel, Switzerland. His research interests include the modeling, fabrication, and replication of micro-optical elements for datacom, telecom, and sensing applications.

Michael T. Gale heads the Optical Microsystems Section at the Zurich laboratory of the Centre Suisse d'Electronique et de Microtechnique (CSEM). He received his BA degree in physics from Cambridge University, England, in 1968 and his MSc degree in optoelectronics from Essex University, England, in 1969. On subsequently joining Laboratories RCA Ltd., Zurich, he worked on a number of holographic and applied optics projects, including surface-relief microimages, laser-writing lithography, the fabrication and applications of diffractive surface relief structures, the development of a single-chip CCD color camera, and applications of CCD imagers in surveillance and metrology. Over 70 technical publications and 18 issued patents have accompanied this work. Since his transfer of the laboratories to PSI in 1987 and to CSEM in 1997, his research interests also include the fabrication and applications of planar micro-optical structures by direct laser writing, replicated integrated optics and optical microsystems for telecommunications, and subwavelength optics.

Markus Rossi received his MS degree in physics in 1989 from ETH Zurich and his PhD in micro-optics in 1995 from University of Neuchâtel, Switzerland. He is a production director with Heptagon, Zurich, Switzerland.